Capillary thinning of viscoelastic fluid filaments

zur Erlangung des akademischen Grades eines
DOKTORS DER INGENIEURWISSENSCHAFTEN (Dr.-Ing.)

von der Fakultät für Chemieingenieurwesen und Verfahrenstechnik des
Karlsruher Institut für Technologie (KIT)
genehmigte

DISSERTATION

von

Dipl.-Ing. Dirk Sachsenheimer
aus Karlsruhe

Referent: Prof. Dr. N. Willenbacher
Koreferent: Prof. Dr. M. Wilhelm
Tag der mündlichen Prüfung: 17.12.2014

Preface

This publication based dissertation collects the main results of my experimental results obtained during April 2011 and June 2014 at the Karlsruhe Institute of Technology, Institute for Mechanical Process Engineering and Mechanics in the group of Applied Mechanics. The main part of this thesis consists of my three publications

1. Determination of axial forces during the capillary breakup of liquid filaments - the tilted CaBER method [Sachsenheimer et al. 2012],

2. Experimental study on the capillary thinning of entangled polymer solutions [Sachsenheimer et al. 2014a], and

3. Elongational deformation of wormlike micellar solutions [Sachsenheimer et al. 2014b].

The publications are framed by a short introduction which gives a brief overview about the CaBER (Capillary Breakup Extensional Rheometry) technique as well as an overall conclusion, outlook, and bibliography. Some diagrams and images are modified in size and color taking into account the one column and full color printing of this dissertation.

I would like to take this opportunity to express my grateful thanks to all persons who contributed directly or indirectly to this work.

I wish to express special thanks to Norbert Willenbacher for supervising my dissertation project and to Manfred Wilhelm for being the second referee.

Furthermore, I wish to say thank you to Christian Dienemann practicing all my presentations unlimited numbers of times. I would suggest that there is no other person who attend that often to a CaBER presentation than Christian.

My students, Sebastian Bindgen, Frank Bossler, Sonja Müller, Thomas Schybilla, Severin Onderka, and Jan Küstner are also gratefully acknowledged for performing experiments and stimulating discussions.

I am grateful to Bernhard Hochstein and Claude Oelschlager for discussing possibilities of technical realizations and the theory of wormlike micelles solutions.

Finally, I would like to say thanks to all my colleagues, especially to the "Mittagessensrunde"

Clara Weis, Monica Schneider, and Susanne Wollgarten as well as to the one and only office colleague Leon Jampolski.

Notations

Latin symbols

c	concentration
c_1	rate constant of micellar breaking
c_2	rate constant of micellar recombination
c^*	critical concentration
c_e	entanglement concentration
c_s	surfactant concentration
$c_{s,max}$	surfactant concentration at maximum viscosity
C	constant
C_1	integration constant
D	diameter
D_0	initial diameter
D_1	diameter at time $t = t_1$
$D_{1,crit}$	critical value of D_1
D_{mid}	midpoint diameter
E_{sciss}	scission energy
F	axial force
$F_{\sigma_{zz}=0}$	apparent axial force
F_{app}	apparent axial force
F_G	gravity force
F_x	force in x-direction
F_y	force in y-direction
G	elastic modulus
G^*	complex modulus
G'	storage modulus
G''	loss modulus
G''_{min}	minimum value of loss modulus
G_0	plateau modulus
g	gravity

g_i	i[th] relaxation strength
h_f	final displacement
h_i	initial displacement
k_B	Boltzmann constant
L_i	left i[th] data point for base line correction
L	temporal position of the upper plate in FiSER experiments
L	length
$\overline{L}$	mean length
L_0	initial displacement in FiSER experiments
M_w	weight average molecular weight
$N(L)$	distribution of micelles length
q	scattering vector
R	molar salt/surfactant ratio
R_c	radius of curvature
R_G	radius of gyration
R_i	right i[th] data point for base line correction
s	length
t	time
t_0	initial time
t_1	time at which the upper plate reaches the end position
t_{fil}	filament life time
t_{fil}^{max}	maximum filament life time
$t_{fil,N}$	filament life time assuming Newtonian thinning behavior
t_s	strike time
t_v	viscous time scale
T	temperature
V	volume
w	approximated bending line
w''	second derivative of the approximated bending line
W	measured bending line
W_L	left mean value of the bending line for base line correction
W_R	right mean value of the bending line for base line correction
W_{corr}	base line corrected bending line
X	force ratio
$\tilde{X}$	intermediate force ratio
X_∞	final force ratio

IV

X_{New}	force ratio in case of Newtonian thinning
x	coordinate direction
y	coordinate direction
y	bending line
y''	second derivative of the bending line
z	coordinate direction

Greek symbols

α	exponent
β	approximation error
$\dot{\gamma}$	shear rate
$\dot{\gamma}_c$	critical shear rate
Γ	surface tension
Δp	pressure drop
ε	Hencky strain
ε_c	critical Hencky strain
ε_L	Hencky strain calculated from the change of the length
$\dot{\varepsilon}$	elongational rate
$\dot{\varepsilon}_L$	elongational rate calculated from the change of the length
η_0	zero shear viscosity
η_e	elongational viscosity
$\eta_{e,app}$	apparent elongational viscosity
η_{sol}	zero shear viscosity of the solvent
$[\eta]$	intrinsic viscosity
Θ	numerical factor for linear diameter decay
λ_1	longest relaxation time in the multi mode Maxwell model
λ_{br}	breakage time
λ_c	crossover shear relaxation time
λ_e	elongational relaxation time
λ_i	i$^{\text{th}}$ relaxation time in the multi mode Maxwell model
λ_{rep}	reptation time
λ_s	terminal shear relaxation time
$\lambda_{s,Max}$	terminal shear relaxation time defined by the multi mode Maxwell model
$\overline{\lambda}_s$	average shear relaxation time
λ_Z	relaxation time of the Zimm model
ν	scaling exponent

ρ	density
σ_{rr}	radial normal stress
σ_{zz}	axial normal stress
φ	volume concentration
ω	angular frequency

Dimensionless numbers

Ec	elasto-capillary number
Re	Reynolds number
Tr	Trouton ratio
Wi	Weissenberg number

Abbreviations

BL	base line
CaBER	capillary breakup extensional rheometer
EIS	Elongational Induced Structure
FENE	finitely extensible nonlinear elastic
FIB	flow-induced birefringence
FiSER	filament stretching extensional rheometer
LDV	laser-Doppler velocimetry
PDI	polydispersity index
PIB	polyisobutylene
SALS	small angle light scattering
SANS	small angle neutron scattering
SAOS	small amplitude oscillatory shear
SIS	shear induced structure
SOR	stress optical rule
WLM	wormlike micelles

Chemicals, surfactants, and polymers

CPyCl	cetylpyridinium chlorid
CTAB	hexadecyltrimethylammonium bromide
C_8TAB	octyl trimethyl ammonium bromide
KBr	potassium bromide
NaCl	sodium chloride
$NaClO_3$	sodium chlorate

NaNO$_3$	sodium nitrate
NaOA	sodium oleate
NaSal	sodium salicylate
PEG	polyethylene glycol
PEO	polyethylene oxide
PS	polystyrene

Contents

Contents

Contents

XII

1 Introduction

Many industrial applications and processes such as coating [Fernando et al. 1989, 2000], spraying [Dexter 1996; Prudhomme et al. 2005] (including mist formation [James et al. 2003] and its prevention [Chao et al. 1984]), inkjet printing [Agarwal and Gupta 2002; Han et al. 2004; Vadillo et al. 2010] or fiber spinning [McKay et al. 1978] include flow kinematics with large elements of elongational flow. Due to this high technical relevance, the correlation between rheological properties against elongational deformation and fluid behavior in processes is a major subject of research.

Technically relevant liquids are often complex multicomponent systems with special flow properties adjusted by adding small amounts of rheological modifier or thickener. A great number of these additional materials are commercially available [Braun and Rosen 2000]. Therefore, understanding the elongational flow properties of such low-viscosity fluids showing e.g. viscoelastic flow behavior is of fundamental importance in process optimization and product development. Measuring the elongational viscosity of such low-viscosity liquids is still a very challenging task because surface tension and gravitational effects can be of the same order of magnitude as viscous oder viscoelastic effects. Nevertheless, different techniques [Tropea 2007] such as fiber spinning [Wagner et al. 1996a,b; Talbott and Goddard 1979; Chan et al. 1988], four-roll mill [Dunlap and Leal 1987; Fuller and Leal 1980], entrance flows [Binding 1991; Boger 1987], opposed jet [Fuller et al. 1987] or tubless siphon [Moan and Magueur 1988] have been developed in the past. All these techniques have a lot of disadvantages like e.g. an unknown pre-shear history, variable strain rates or a flow which is not purely extensional as summarized in figure 1.1. Therefore, these techniques might be used to get an index of the elongational properties of an non-Newtonian fluid but cannot determine the elongational viscosity η_e unambiguously since η_e depends on both, the deformation rate and the total deformation of the material, and cannot be characterized by a single value [Tropea 2007].

Fiber spinning

Flow:	uniaxial extension
Limitations:	Low strain, non-uniform strain rates
	pre-shear history
Range:	$\eta_0 > 1$ Pas
	10 s$^{-1} < \dot{\varepsilon} < 10^3$ s^{-1}; $\varepsilon_{max} \leq 2-3$

Four-roll mill

Flow:	uniaxial extension
Limitations:	variable strain rates and strain history,
	unknown total strain, non-uniform
	deformation
Range:	$\eta_0 = 1 - 1000$ Pas
	10^{-2} s$^{-1} < \dot{\varepsilon} < 10^2$ s^{-1}

Entrance flows

Flow:	uniaxial extension
Limitations:	variable strain rates, mixed with shear
	many approximations, limited use
Range:	$\eta_0 > 1$ Pas
	10^{-2} s$^{-1} < \dot{\varepsilon} < 10^2$ s^{-1} typical

Opposed jet

Flow:	stagnation flow, uniaxial extension
Limitations:	variable strain rates and strain history,
	some shear
Range:	$\eta_0 = 0.01 - 1$ Pas
	1 s$^{-1} < \dot{\varepsilon} < 10^4$ s^{-1}; $\varepsilon_{max} \approx 1$ approximated

Tubeless siphon

Flow:	uniaxial extension
Limitations:	pre-shear history, variable strain rates,
	low achievable strain rates
Range:	$\eta_0 = 1 - 1000$ Pas
	$\dot{\varepsilon} < 10$ s^{-1}; $\varepsilon_{max} \approx 4$

Figure 1.1: Summary of common extensional rheometer for low-viscosity fluids. [Tropea 2007; Macosko 1994; Dontula et al. 1997; Pope and Keller 1977; Kato et al. 2002]

However, two additional techniques are discussed in the literature for determining elongational material parameters of low-viscosity fluids. Filament stretching [Matta and Tytus 1990; Spiegelberg et al. 1996; Tirtaatmadja and Sridhar 1993; Muller and Froelich 1985] or capillary breakup [McKinley and Tripathi 2000; Bazilevsky et al. 1990; Entov and Hinch 1997; Bazilevsky et al. 2001; Anna and McKinley 2001; Tirtaatmadja and Sridhar 1993; Spiegelberg et al. 1996; Anna et al. 1999; Orr and Sridhar 1999; McKinley et al. 2001; McKinley and Sridhar 2002; Anna et al. 2001; Rothstein and McKinley 2002a,b; Rothstein 2003; Tropea 2007] experiments analyze the thinning behavior of slender filaments (see figure 1.2). In both types of experiments, the flow field is predominantly extensional and the pre-stretch history is known.

Filament stretching

	Flow:	uniaxial extension
	Limitations:	sample gripping, elastic instability,
		influence of gravity and surface tension
	Range:	$\eta_0 = 1 - 1000$ Pas
		10^{-1} s^{-1} < $\dot{\varepsilon}$ < 10 s^{-1}
		$\varepsilon_{max} \leq 5 - 7$

Capillary breakup

	Flow:	uniaxial extension
	Limitations:	no predefined strain rates
	Range:	$\eta_0 = 0.01 - 100$ Pas
		10^{-2} s^{-1} < $\dot{\varepsilon}$ < 10^2 s^{-1}
		$\varepsilon_{max} \leq 14$
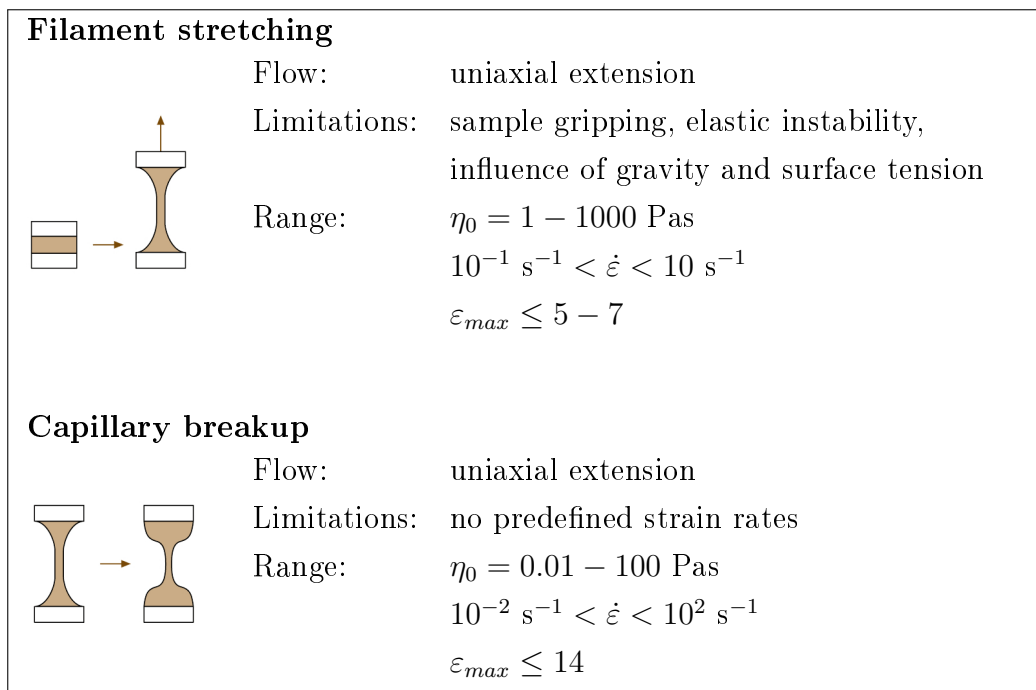
Figure 1.2: Filament stretching (top) and capillary breakup (bottom) devices. [Tropea 2007; Anna et al. 2001; McKinley et al. 2001; Arnolds et al. 2010; Yesilata et al. 2006]

In a filament stretching extensional rheometer (FiSER) the liquid under test is placed between to parallel plates. The upper plate is separated continuously until the filament breaks [Tropea 2007]. The deformation rate is monitored using a laser micrometer or a video camera, and the axial force is captured with a load cell attached to the lower (stationary) plate [Morrison 2001]. Generally, two types of velocity profiles are possible [Kolte et al. 1997]: The upper plate is separated with an exponentially increasing velocity or the plate velocity is controlled, such that the filament diameter decreases exponentially corresponding to

constant elongational rate during the whole experiment [Kolte et al. 1997; Tropea 2007]. The transient elongational viscosity is then computed from the tensile force and the filament diameter at the axial midpoint [McKinley et al. 2001]. The main advantage of FiSER measurements is that the experiment starts from a well defined rest state. But inhomogeneities caused by secondary flows near the end plates complicate the interpretation of the measured axial stress and gravity as well as surface tension can affect the elongational viscosity value, too [Morrison 2001]. Furthermore, a shear viscosity of at least $\eta_0 = 1$ Pas is required due to the limited sensitivity of the fore transducer. This hinders the analysis oft fluids with very low viscosity like dilute polymer solutions.

However, the called capillary breakup extensional rheometer (CaBER) is a simple and versatile method for the characterization of low-viscosity fluids. It has been suggested more than 20 years ago [Bazilevsky et al. 1990; Entov and Hinch 1997; Bazilevsky et al. 2001] and is even commercially available now. Performing a CaBER experiment is fast and simple and total deformations of up to $\varepsilon_{max} = 14$ can be achieved. Such high strains are of grate significance to industrial practice. The strain rate is determined my the fluid and varies typically between 10^{-2} s$^{-1} < \dot{\varepsilon} < 10^2$ s^{-1} but values up to $\dot{\varepsilon}_{max} = 8000$s^{-1} are reported [Vadillo et al. 2010]. A detailed overview of this technique is given in the following.

1.1 Capillary Breakup Extensional Rheometer (CaBER)

The CaBER experiment is based on the creation of an instable liquid bridge. Therefore, the liquid under test is placed between two parallel plates (diameter of D_0) which have an initial displacement h_i. After sample loading, an initial step strain is applied within a short strike time in a range of typically $t_s = 20 \ldots 100$ ms causing an final displacement h_f between the two plates. It should be mentioned that h_f must be sufficient large in order to destabilize the filament. The initial striking process is illustrated in figure 1.3 where the time dependent displacement of the upper plate is shown. The experiment starts at time t_0 with linear displacement of the upper plate (constant velocity). Monitoring of the filament diameter as a function of time allows for the determination of characteristic elongational flow properties such as the apparent elongational viscosity [Anna and McKinley 2001], the elongational relaxation time [Entov and Hinch 1997; Clasen 2010] or the elongational yield stress [Niedzwiedz et al. 2009, 2010; Martinie et al. 2013]. The thinning behavior of a liquid thread is controlled by the capillary force and viscous or visco-elastic forces. The interplay of these forces results in characteristic diameter vs. time curves observed experimentally and predicted theoretically for different types of fluids, e.g. Bingham plastic, power law, Newtonian or visco-elastic fluids [McKinley 2005].
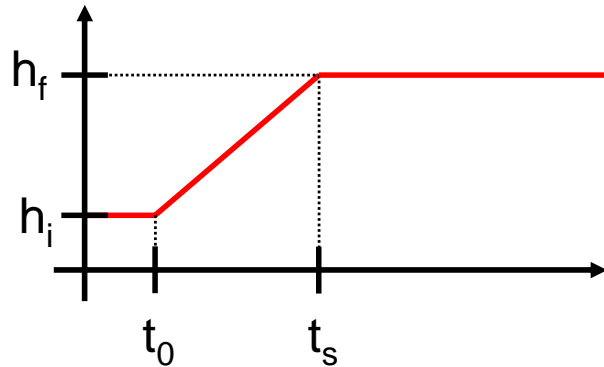
Figure 1.3: Position of the upper plate in a CaBER experiment as a function of time.

The commercial available version of the Capillary Breakup Extensional Rheometer distributed by Thermo Haake (Karlsruhe, Germany) is equipped with a laser micrometer for diameter detection. However, this way of monitoring the diameter decay is not unambiguous since the diameter is only determined at a single position somewhere in the filament. Such diameter measurements might obtain reliable values as long as the fluid filament is purely cylindrical but, unfortunately, the shape of the thinning thread can depend on the type of fluid as illustrated in figure 1.4. Here, typical pictures of a Newtonian liquid, a viscoelastic liquid and a Bingham fluid during the thinning process are shown. Cylindrical filaments are only observed for viscoelastic materials [Bazilevsky et al. 1990; Anna and McKinley 2001; Arnolds et al. 2010; McKinley 2005] whereas filaments of Newtonian or Bingham liquids form non-cylindrical shapes.
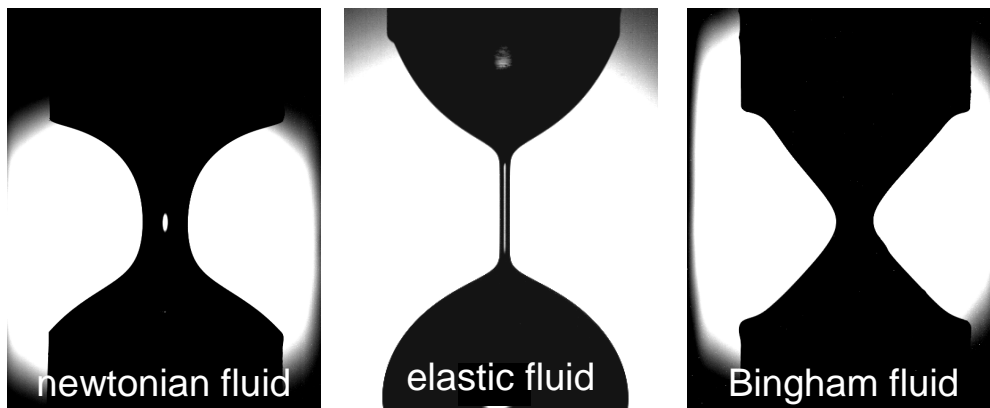

Figure 1.4: Pictures of three different fluid types undergoing capillary thinning. Left: Newtonian liquid, middle: viscoelastic fluid, and right: Bingham fluid.

In order to get a larger field of application, an optical setup has been developed at the Institute for Mechanical Process Engineering and Mechanics allowing for determination of the

whole filament with a high spatial and temporal resolution [Niedzwiedz et al. 2009; Arnolds et al. 2010; Arnolds 2011]. Therefore, a high speed camera, telecentric backlight illumination, and telecentric objectives has been used as shown in figure 1.5. Analyzing the shape of the thread allows for a correct monitoring of the diameter decay during the thinning process as well as filament breakup mechanisms.
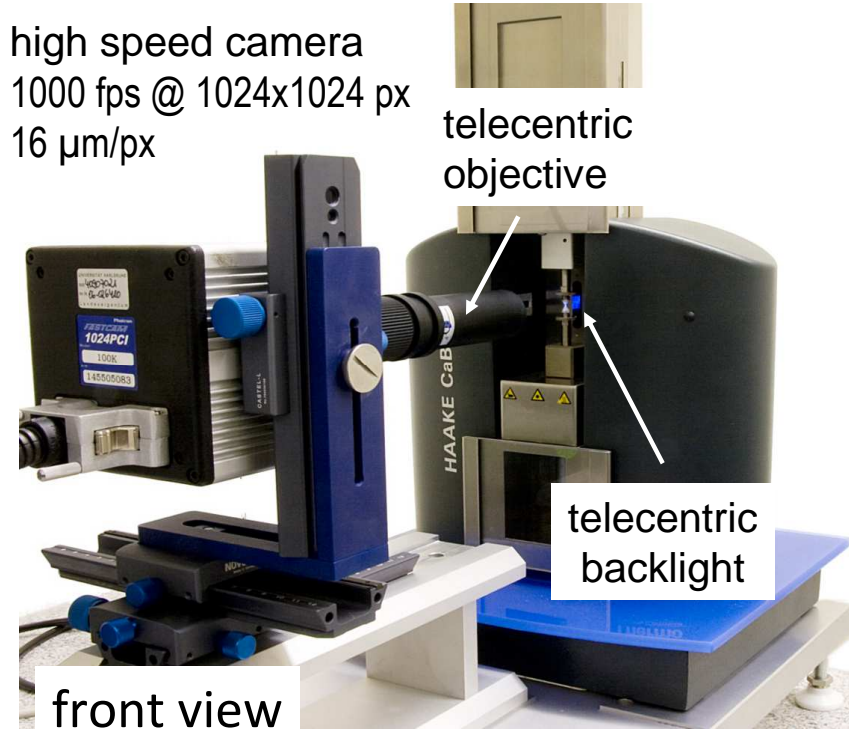
Figure 1.5: Advanced CaBER setup. The diameter decay of a liquid filament undergoing capillary thinning is monitored using a high speed camera equipped with telecentric objectives. The filament is illuminated with a telecentric backlight.

1.1.1 Basic data evaluation

As mention above, CaBER experiments are used for determination of elongational material properties. The elongational rate

$$\dot{\varepsilon} = -\frac{2}{D_{min}} \frac{\mathrm{d}D_{min}}{\mathrm{d}t} \tag{1.1}$$

is commonly calculated from the decrease of the minimum diameter D_{min} of the thinning liquid thread and the accumulated Hencky strain than reads

$$\varepsilon = \int\limits_0^t \dot{\varepsilon}\,\mathrm{d}t = 2\ln\left(\frac{D_0}{D_{min}}\right) \ , \tag{1.2}$$

where D_0 is the initial diameter.

Unfortunately, the axial force F is not measured during CaBER experiments. Instead, the elongational viscosity is calculated based on an apparent axial force $F_{app} = \pi \Gamma D$ assuming that no axial normal stresses σ_{zz} ($\sigma_{zz} = 0$ assumption) are present in the filament. As a consequence, the universal definition of the elongational viscosity [Schümmer and Tebel 1983]

$$\eta_e = \frac{\sigma_{zz} - \sigma_{rr}}{\dot{\varepsilon}} \, , \tag{1.3}$$

where σ_{zz} and $\sigma_{rr} = -2\Gamma/D$ are the axial and radial normal stresses, reduces to the apparent elongational viscosity

$$\eta_{e,app} = \frac{-\sigma_{rr}}{\dot{\varepsilon}} = -\frac{\Gamma}{\mathrm{d}D/\mathrm{d}t} \tag{1.4}$$

for CaBER data analysis [Anna and McKinley 2001]. Discussing the apparent elongational viscosity is widely used in literature [Rothstein 2003; Yesilata et al. 2006; Oliveira et al. 2006; Bhardwaj et al. 2007a,c; Sattler et al. 2007; Chellamuthu and Rothstein 2008; Kheirandish et al. 2008; Tuladhar and Mackley 2008; Chen et al. 2008; Yang and Xu 2008; Kheirandish et al. 2009; Arratia et al. 2009; Miller et al. 2009; David et al. 2009; Regev et al. 2010; Bischoff White et al. 2010; Clasen 2010; Becerra and Carvalho 2011; Erni et al. 2011; Rathfon et al. 2011; Nelson et al. 2011; Haward et al. 2012b; Haward and McKinley 2012; Gier and Wagner 2012; Tembely et al. 2012; Vadillo et al. 2012; Sankaran and Rothstein 2012], but the $\sigma_{zz} = 0$ assumption has not been validated experimentally. Deviations obviously occur for the Newtonian case [Liang and Mackley 1994; Kolte and Szabo 1999; McKinley and Tripathi 2000] and also shown in numerical simulations of the CaBER experiment using different viscoelastic or viscoplastic constitutive equations [Clasen et al. 2006a; Webster et al. 2008; Alexandrou et al. 2009].

1.1.2 Previous force measurement attempts

Fluid characterization based on equation 1.4 might be helpful in comparative studies employed, e.g., for product development purposes. But especially for the determination of the true elongational viscosity from CaBER experiments, it is mandatory to measure the time-dependent axial force F during filament thinning accurately. Klein et al. [Klein et al. 2009] mounted a commercial quartz load cell to the fixed bottom plate of a CaBER device. Due to oversampling of the force signal, a nominal sensitivity of 50 μN was reached, but calibration was only done in the force range larger than 2,000 μN. Thus, reliable force detection during

capillary thinning of fluid filaments was not possible and calculated elongational viscosities, especially for the polystyrene solution investigated in there study, show non-physical values. Furthermore, diameter and force measurements were not synchronized causing a shift between these two data. The force transducer extension of Klein et al. [Klein et al. 2009] might be helpful for determining axial forces for high viscosity fluids ($\eta_0 \gtrsim 100$ Pas) during the step strain but obviously not during the capillary thinning.

A second way for determination axial forces during a CaBER experiment might be the analysis of horizontally stretched filaments which show a pronounced deflection due to gravity [Arnolds 2011]. The force calculation is based on the beam bending theory where a constant curvature as well as a constant diameter over the filament length was assumed. Presented experimental data [Arnolds 2011] for Newtonian silicon oils show Trouton ratios Tr > 3 which indicates an inaccurate force detection since Tr = 3 is expected (and also found for these solutions) for Newtonian liquids undergoing uniaxial elongation. The origin of this deviation is not comprehensible and might be related to a incorrect force calculation. Finding Tr > 3 for Newtonian liquids in a CaBER experiment corresponds to an additional contribution to the true axial force F ($F/F_{app} > 1$) but $F/F_{app} \approx 0.6$ was also reported. Furthermore, viscoelastic polyethylene oxide solutions do not show an elongational hardening behavior as expected [Sridhar et al. 1991; Solomon and Muller 1996].

Up to now, axial forces during the whole capillary thinning process have not been measured unambiguously.

1.2 Time evolution of the filament diameter during capillary thinning

The time evolution of the diameter during capillary thinning is controlled by a balance of capillary and viscous or viscoelastic forces. Different characteristic in diameter vs. time curves are observed for different types of fluids, e.g., Bingham plastic, power law, and Newtonian or viscoelastic fluids. The cases of Newtonian and visco-elastic tinning will be discussed shortly in the following. More details of the thinning behavior of yield stress fluids are given in the literature [Goldin et al. 1972; Mahajan et al. 1999; McKinley 2005; Niedzwiedz et al. 2009, 2010; Martinie et al. 2013]

1.2.1 Ideal Newtonian fluid

A Newtonian liquid creates slightly non-cylindrical filaments in CaBER experiments as illustrated in figure 1.6 where the thinning process of a silicon oil with a zero shear viscosity of approximately $\eta_0 \approx 1\,\mathrm{Pas}$ is shown exemplarily. The midpoint diameter D_{mid} of a Newto-
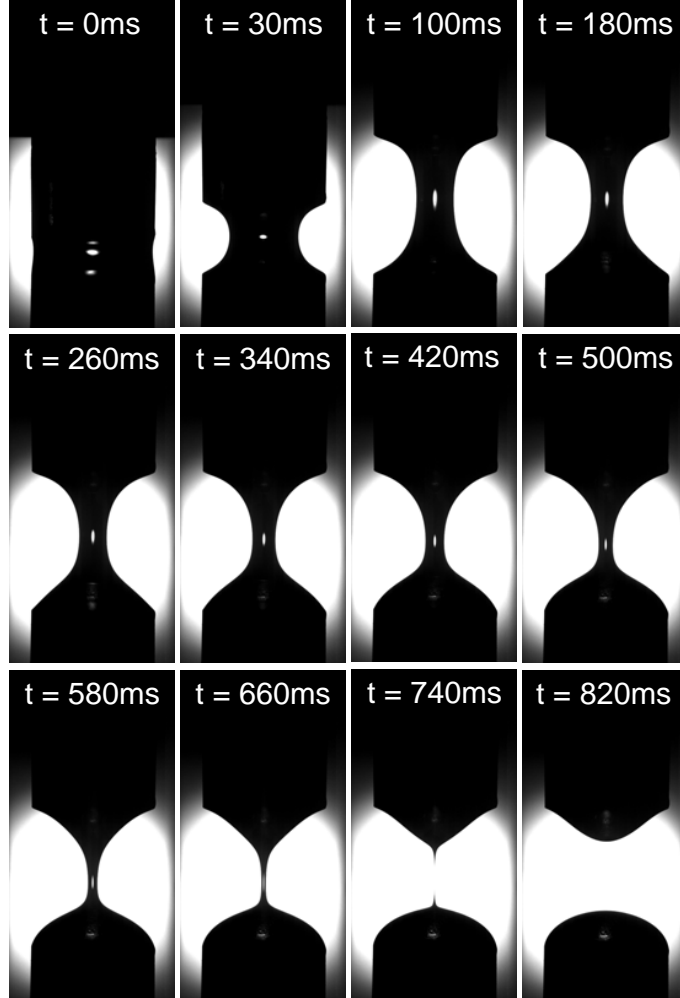
Figure 1.6: Capillary thinning of silicon oil AK 1000 with Newtonian flow behavior in CaBER experiments

nian fluid in a CaBER experiment decreases linearly with time t according to [Papageorgiou 1995; McKinley and Tripathi 2000]:

$$D_{mid} = D_0 - \Theta\,\frac{\Gamma}{\eta_0}\,t \;, \tag{1.5}$$

where D_0 is the initial diameter of the liquid bridge, Θ is a numerical pre-factor, Γ is the surface tension, and η_0 is the shear viscosity. Early analysis of the capillary thinning of Newtonian liquids was based on a local force balance [Bazilevsky et al. 1990; Liang and

Mackley 1994; Kolte and Szabo 1999] only considering viscous stresses in radial direction and surface tension but neglecting axial normal stresses and inertia (Reynolds number: Re = 0).

$$3\eta_0\dot{\varepsilon} = -\frac{2\Gamma}{D_{mid}} \qquad \Rightarrow \qquad D_{mid} = D_0 - \frac{\Gamma}{3\eta_0}t \tag{1.6}$$

This simple force balance obviously results in a numerical pre-factor of $\Theta = 1/3$. However, numerical studies have focused on the unsteady Stokes equation. In case of negligible inertia (Re = 0) Papageorgiou [Papageorgiou 1995] calculated a value of $\Theta = 0.1418$. Considering inertia (Re > 0), Eggers [Eggers 1993, 1997] and Brenner [Brenner et al. 1996] estimated the numerical factor to $\Theta = 0.0608$ and showed that this solution is valid near the filament break up. Finally, McKinley and Tripathi [McKinley and Tripathi 2000] confirmed the numerical results of Papageorgiou experimentally for the capillary thinning of glycerol samples in a CaBER device.

1.2.2 Ideal viscoelastic fluid

In contrast to Newtonian liquids, cylindrical filaments and an exponential diameter decay according to

$$D(t) = D_0 \left(\frac{G\,D_0}{\Gamma}\right)^{1/3} \exp\left(-\frac{t}{3\lambda_e}\right) \,, \tag{1.7}$$

has been predict for Maxwell fluids [Liang and Mackley 1994; Entov and Hinch 1997]. Here G is the elastic modulus and λ_e is the elongational relaxation time which is related to the elongational rate $\dot{\varepsilon}$ (defined in equation 1.1)

$$\dot{\varepsilon} = \frac{2}{3\lambda_e} \,. \tag{1.8}$$

Experimental results for a broad variety of weakly viscoelastic polymer solutions are well described by equation 1.7 even if their rheological behavior is not fully captured by the ideal Maxwell model. [Bazilevsky et al. 1990; Entov and Hinch 1997; Anna and McKinley 2001; Arnolds et al. 2010]. The elongational relaxation time λ_e has been compared to different molecular and shear relaxation times, e.g. a mean shear relaxation time $\overline{\lambda}_s$ [Liang and Mackley 1994], the Zimm relaxation time λ_Z [Christanti and Walker 2001a, 2002a; Rodd et al. 2005; Tirtaatmadja et al. 2006; Clasen et al. 2006a,b; Clasen 2010; Campo-Deaño and Clasen 2010; Vadillo et al. 2012; Haward et al. 2012b], or the terminal relaxation time λ_s [Oliveira et al. 2006; Arnolds et al. 2010; Clasen 2010], but no simple and universal correlation between these values could be found. A detailed state of the art will be given in section 4.3.1.

However, e.g. for polymer solutions with concentrations above the overlap concentration $(c > c^*)$ relaxation time ratios $\lambda_e/\lambda_s < 1$ have been reported [Oliveira et al. 2006; Arnolds et al. 2010; Clasen 2010]. Arnolds et al. [Arnolds et al. 2010] have quantified the effect of non-linear deformation in CaBER experiments using a single factorizable integral model including a damping function which has been determined from steady shear data. The decrease of the relaxation time ratio λ_e/λ_s with increasing polymer concentration could be predicted quantitatively.

More complex systems like surfactant solutions forming entangled wormlike micelles, polyelectrolyte complexes in solution or aggregated acrylic thickener solutions also exhibit relaxation time ratios $\lambda_e/\lambda_s < 1$, but these systems are supposed to undergo structural changes in strong elongational flow [Bhardwaj et al. 2007b; Kheirandish et al. 2008; Willenbacher et al. 2008].

1.3 Wormlike micelles solutions

The mechanical behavior of wormlike micelles (WLM) solutions is very complex due to the equilibrium nature of such structures. The dynamic self-assembly process enables micelles to break and recombine all the time and causes a distribution of micelle lengths [Cates 1988, 1987; Israelachvili et al. 1976]

$$N(L) = \frac{2\,c_1}{c_2} \exp\left(-\frac{L}{\overline{L}}\right)\ , \tag{1.9}$$

where c_1 and c_2 are the rate constants for breakage and recombination, respectively and $\overline{L}$ is the average length of the micelles given by

$$\overline{L} \approx \phi^{1/2} \exp\left(\frac{E_{sciss}}{2k_B\,T}\right)\ . \tag{1.10}$$

Here, ϕ is the total surfactant volume fraction, k_B is the Boltzmann constant, T is the temperature, and E_{sciss} is the scission energy defined as the difference between the energy required to create two hemispherical end-caps and the energy of the rodlike structure containing an equal number of surfactant molecules.

However, the ratio of the breaking time $\lambda_{br} = \left(c_1\,\overline{L}\right)^{-1}$ [Cates 1987; Rehage and Hoffmann 1991; Khatory et al. 1993] and the reptation time λ_{rep} is decisive for the rheological behavior of entangled WLM systems. In the slow breakage limit $(\lambda_{br} >> \lambda_{rep})$ the distribution of micellar length (equation 1.9) causes a broad distribution of relaxation times and stress relaxation is characterized by a stretched exponential law for the relaxation function $G(t)$ [Larson 1999; Cates 1987, 1988; Rehage and Hoffmann 1988, 1991]. Representative storage

G' and loss moduli G'' as a function of angular frequency ω are shown in figure 1.7 (left). In case of the fast breaking limit ($\lambda_{br} << \lambda_{rep}$), the stress relaxation is characterized by one single (shear) relaxation time $\lambda_s = \sqrt{\lambda_{br}\lambda_{rep}}$ [Rehage and Hoffmann 1988; Cates 1987, 1988; Cates and Candau 1990; Granek and Cates 1992]. Therefore, the complex moduli G' and G'' are well described over a wide range of frequency ω using a single Maxwell model , as illustrated in figure 1.7 (right), exemplary. The deviation between experimental results and the single Maxwell prediction for high frequencies are related to a Rouse-like motion of micelles between two entanglement points [Fischer et al. 1997; Granek and Cates 1992; Kern et al. 1994; Yesilata et al. 2006].
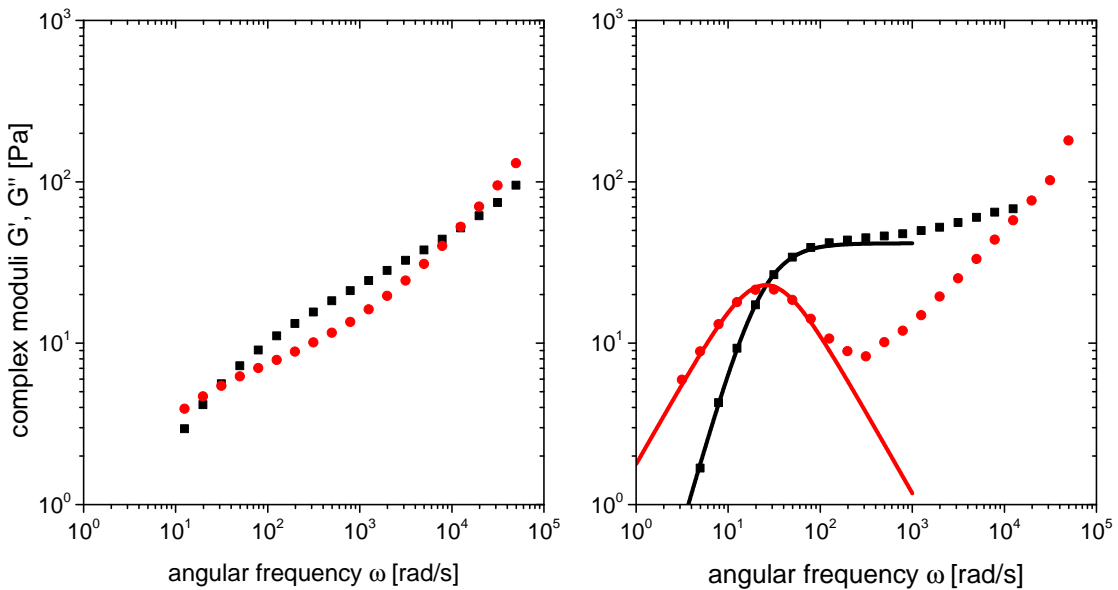
Figure 1.7: Storage and loss moduli G' and G'' as a function the angular frequency ω (left) for a CPyCl/NaSal solution in the slow breaking limit ([CPyCl] = 100mM and salt/surfactant ratio $R = 0.5$) and (right) for a CPyCl/NaSal solution in the fast breaking limit ([CPyCl] = 100mM and salt/surfactant ratio $R = 2.8$). The solid lines represent a single mode Maxwell fit to the experimental data.

Moreover, the transient micelles character enables more mechanisms for stress relief like e.g ghostlike crossing or sliding of branching points [Appell et al. 1992]. This very efficient stress relaxation mechanisms cause a decreasing viscosity value with increasing number of branching points [Candau et al. 1993; Raghavan and Kaler 2001; Schubert et al. 2003; Ziserman et al. 2004; Oelschlaeger et al. 2010] which are indicated by a increase of the plateau modulus G_0 [Candau et al. 1993; Raghavan and Kaler 2001; Schubert et al. 2003; Chellamuthu and Rothstein 2008; Oelschlaeger et al. 2009, 2010]. Therefore, the viscosity of WLM solutions (with constant surfactant concentration) can vary orders of magnitude if the salt/surfactant

ratio R is increased and distinct maxima in the viscosity over R function can occur as illustrated in figure 1.8 exemplary for three different surfactant solutions. The first viscosity
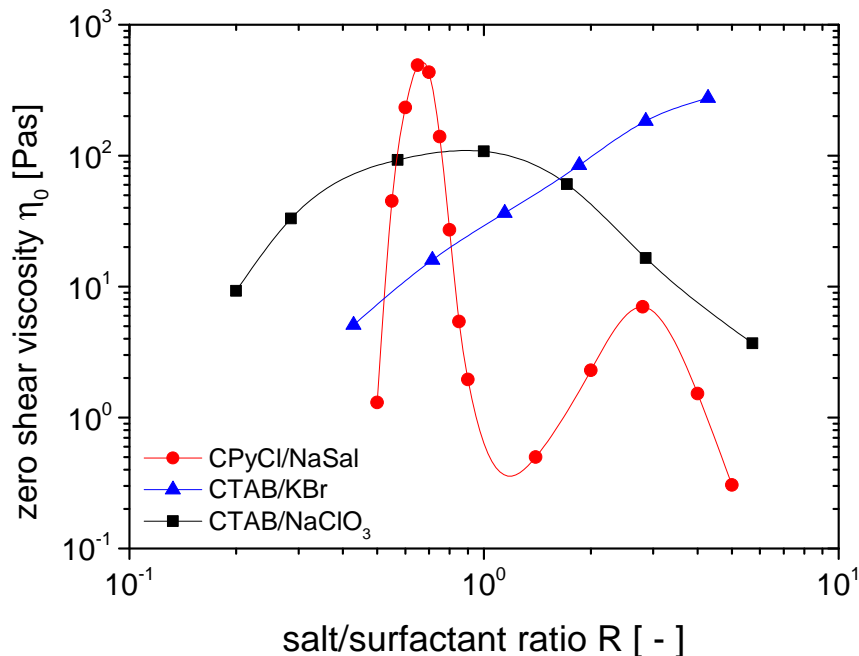
Figure 1.8: Zero shear viscosity η_0 as a function of salt/surfactant ratio R for 100 mM CPyCl/NaSal, 350 mM CTAB/NaClO$_3$, and 350mM CTAB/KBr solutions. Values are taken from Oelschlaeger et al. [Oelschlaeger et al. 2010].

maximum is attributed to a transition from linear to branched micelles [Porte et al. 1986; Drye and Cates 1992; Lequeux 1992; Croce et al. 2003; Ziserman et al. 2004; Oelschlaeger et al. 2009, 2010; Danino 2012] whereas the second maximum (if present) is related to a change of the number of branching points as well as a change in micellar length [Porte et al. 1986; Drye and Cates 1992; Oelschlaeger et al. 2009]. A second viscosity maximum is mainly observed for CPyCl/NaSal and CTAB/NaSal solutions where NaSal is strongly binding to the micelles [Rehage and Hoffmann 1988, 1991; Nemoto et al. 1995; Mohanty et al. 2001; Galvan-Miyoshi et al. 2008; Oelschlaeger et al. 2009].

1.3.1 Elongational flow of WLM solutions

The elongational rheology of WLM solutions is poorly understood and very little is known about extensional thickening and structure formation in extensional flow. Early investigations were based on opposed jet experiments [Fischer et al. 1997; Lu et al. 1998; Prudhomme and Warr 1994; Walker et al. 1996; Chen and Warr 1997], four-roll mill experiments [Kato et al. 2002, 2004, 2006], entrance flow [Okawara et al. 2008, 2009], two-dimensional squeeze

flow [Takahashi et al. 2001] and flow through porous media experiments [Muller et al. 2004] showing an elongational hardening of WLM solutions which is attributed to strong alignment of the micelles in flow direction. Exceeding a critical elongation rate, the elongational viscosity starts to decrease in line with a decrease of the radius of gyration in flow direction. This has been taken as evidence for a micellar scission induced by elongational flow [Chen and Warr 1997] as predicted theoretically [Vasquez et al. 2007; Cromer et al. 2009; Germann et al. 2013].

In contrast to a possible micellar scission due to elongational flow, the effect of a structure build-up during an elongational deformation is almost uninvestigated. Okawara et al. [Okawara et al. 2008, 2009] analyzed the pressure loss Δp of CTAB/NaSal solutions with surfactant concentrations $c_s = 30$ mM at high salt/surfactant ratios R flowing through two different converging channels and detected structural changes using simultaneous SALS experiments. For a distinct apparent elongation rate regime (regime II), a strong increase of Δp with increasing elongational rate has been observed. Corresponding SALS measurements show a combination of butterfly-type and streak-type pattern indicating a structure build-up. A further increase of the apparent elongation rate (regime III) results in a weaker increase of Δp with increasing $\dot{\varepsilon}$ than in regime II and a change in the SALS patterns indicates a less pronounced structure build-up at these elevated elongation rates. Furthermore, the measurements of Okawara et al. show that the creation of elongation-induced structures (EIS) depends not only on the elongational rate but also on the total Hencky strain.

Takahashi et al. [Takahashi and Sakata 2011] investigated the flow induced structure build-up of similar solutions CTAB/NaSal solutions ($c_s = 30$ and $R > 1$) in planar elongation using a squeeze flow device. In this setup elongational deformation is dominant in the center plane whereas shear dominates close to the walls. Structure formation was verified by the occurrence of opaque regions during flow at the rim close to the walls (shear-induced structure, SIS) as well as in the center plane (elongation-induced structure, EIS). SIS was observed at shorter elapsed times than EIS but at significantly higher critical strains and strain rates. Furthermore, the elongation-induced structures occurred at a critical total strain ε_c irrespective of the salt/surfactant ratio R but all solutions had R values corresponding to the fast breaking limit (branched micelles).

Continuous filament stretching (FiSER) and capillary thinning (CaBER) experiments have been performed to investigate the elongational behavior of WLM solutions in a purely uniaxial deformation field [Rothstein 2003; Yesilata et al. 2006; Bhardwaj et al. 2007a,c; Chellamuthu and Rothstein 2008; Miller et al. 2009; Kim et al. 2010]. These solutions clearly form exponentially thinning cylindrical filaments [Yesilata et al. 2006] and corresponding relaxation time ratios λ_e/λ_s between 0.02 and 2 are reported [Yesilata et al. 2006; Bhardwaj

et al. 2007a; Chellamuthu and Rothstein 2008] similar to concentrated polymer solutions [Oliveira et al. 2006; Arnolds et al. 2010; Clasen 2010].

The only study addressing the role of branching on the extensional rheology of WLM has been performed by Chellamuthu and Rothstein [Chellamuthu and Rothstein 2008]. For a series of linear and branched WLM solutions of sodium oleate (NaOA) and octyltrimethyl ammonium bromide (C_8TAB) these authors observe a dramatic decrease of relaxation time ratio λ_e/λ_s in CaBER and a maximum Trouton ratio in FiSER with the onset of branching. They hypothesize that this is due to the additional stress relief mechanisms caused by sliding or ghost-like crossing effects which are supposed to be more efficient in elongational flows. This study suggests that transient extensional rheology might be suitable to distinguish between branched and linear micelles. But as discussed in section 5.4 (where the most significant results of this dissertation will be shown) the elongational behavior of WLM solutions is more complex than expected by Chellamuthu and Rothstein [Chellamuthu and Rothstein 2008].

2 Open questions and manuscript overview

The introduction already points out that the CaBER data evaluation is based on the $\sigma_{zz} = 0$ assumption and elongational viscosities are only determined as apparent values. So far, this assumption has not been validated experimentally for the CaBER experiment. Deviations obviously occur for the Newtonian case [Liang and Mackley 1994; Kolte and Szabo 1999; McKinley and Tripathi 2000] and are also shown in numerical simulations of the CaBER experiment using different viscoelastic or viscoplastic constitutive equations [Clasen et al. 2006a; Webster et al. 2008; Alexandrou et al. 2009]. Therefore, fluid characterization only based on apparent values (e.g. equation 1.4) might be helpful in comparative studies employed, e.g., for product development purposes. But especially for the determination of the true elongational viscosity η_e from CaBER experiments, it is mandatory to measure the time-dependent axial force F during filament thinning accurately. Furthermore, knowing the axial force F during the whole thinning process might give a better understanding of the CaBER experiment and additional information about the thinning behavior of viscoelastic fluid filaments.

Furthermore, only little is known about the self controlled thinning behavior of concentrated polymer solutions. The dependency of the elongational relaxation time λ_e on the polymer concentration and its relation to the shear relaxation time λ_s is unclear.

Besides covalently bound polymer solutions, self assembly surfactant solutions forming entangled or branched wormlike micelles are still of great scientific as well as technical interest. Investigations so far mainly focused on the shear behavior of such solutions but very little is known about their response to an elongational deformation. Despite some data in the literature [Bhardwaj et al. 2007a; Chellamuthu and Rothstein 2008] a systematic investigation of extensional flow behavior as a function of the salt/surfactant ratio R covering both viscosity maxima (if present) is still lacking and there are still uncertainties and questions that remain open. First, the variation and interpretation of the elongational relaxation time λ_e and its relation to the shear relaxation time λ_s as a function of surfactant or salt concentration is unclear. The question wether extensional rheology is able to distinguish between linear and

branched micelles is also still open. Furthermore, the phenomenon of structure build-up during elongational flow is almost uninvestigated.

The following main part contain three publications focusing on the force determination during capillary thinning (Determination of axial forces during the capillary breakup of liquid filaments - the tilted CaBER method [Sachsenheimer et al. 2012]), the elongational rheology of entangled polymer solutions (Experimental study on the capillary thinning of entangled polymer solutions [Sachsenheimer et al. 2014a]), and finally the first systematic study on the elongational behavior of WLM solutions (Elongational deformation of wormlike micellar solutions [Sachsenheimer et al. 2014b]) which is probably the most significant part of this thesis.

In chapter 3 a new way of performing CaBER experiments is introduced. This so called tilted CaBER method is a simple and accurate way to determine the axial force $F(t)$ during thinning of slender filaments by only analyzing video images. Therefore, the conventional CaBER device is rotated by 90° and the bending of the liquid filament due to gravity is recorded using a high-speed camera. The tilted CaBER method is verified using Newtonian fluids and applied to non-Newtonian poly ethyleneoxide (PEO) solutions. In this context the true elongational viscosity for low-viscosity polymer solutions is determined with CaBER for the first time.

Based in this results the capillary thinning of concentrated and mostly entangled polymer solutions is discussed in detail in chapter 4. Here the so called transient force ratio $X(t)$, which is the ratio of the true axial force F and apparent axial force F_{app} assuming $\sigma_{zz} = 0$, including its effect on the elongational viscosity is discussed. In addition, $X(t)$ data are used to prove the existence of a middle Newtonian regime during the thinning of viscoelastic fluid filaments as predicted earlier [Entov and Hinch 1997; Clasen 2010]. Furthermore, the influence of polymer concentration, temperature, and solvent viscosity on the relaxation time ratio λ_e/λ_S is investigated and a universal scaling of λ_e/λ_S for polymer solutions is given. Finally, CaBER results for some surfactant solutions with filament stretching (FiSER) measurements are compared.

In section 5 the CaBER method is used to get a deeper insight into the rheological behavior of six different WLM solutions covering a broad range of surfactant concentrations c_s and salt/surfactant ratios R including samples knowing to exhibit shear-induced structure formation. General observations of filament formation and subsequent thinning of WLM solutions are discussed in detail. Elongational material properties such as filament lifetime t_{fil} and elongational relaxation time λ_e are related to corresponding shear parameters for solutions in the low and fast breaking limit. More details about the ability of distinguishing

between linear and branched micelles are given. Finally, elongation induced structures (EIS) created during capillary thinning are discussed here for the first time.

3 The tilted CaBER method

3.1 Abstract

The capillary breakup extensional rheometry (CaBER) is a versatile method to characterize the elongational behavior of low-viscosity fluids. Commonly, data evaluation is based on the assumption of zero normal stress in axial direction ($\sigma_{zz} = 0$). In this paper, we present a simple method to determine theaxial force using a CaBER device rotated by 90° and analyzing the deflection of the filament due to gravity. Forces in the range of $0.1 - 1,000\ \mu$N could be assessed. Our study includes experimental investigations of Newtonian fructose solutions and silicon oil mixtures (viscosity range, $0.9 - 60$ Pas) and weakly viscoelastic polyethylene oxide (PEO, $M_w = 10^6$ g/mol) solutionscovering a concentration range from $c \approx c^*$ (critical overlap concentration) up to $c > c_e$ (entanglement concentration). Papageorgiou's solution for the stress ratio σ_{zz}/σ_{rr} in Newtonian fluids during capillary thinning is experimentally confirmed, but the widely acceptedassumption of vanishing axial stress in weakly viscoelastic fluids is not fulfilled for PEO solutions, if c_e is exceeded.

3.2 Introduction

3.2.1 General remarks

Many industrial applications and processes such as coating [Fernando et al. 1989, 2000], spraying [Dexter 1996; Prudhomme et al. 2005] (including mist formation [James et al.

2003] and its prevention [Chao et al. 1984]), inkjet printing [Agarwal and Gupta 2002; Han et al. 2004; Vadillo et al. 2010] or fiber spinning [McKay et al. 1978] include flow kinematics with large elements of elongational flow. Due to this high technical relevance, the correlation between rheological properties against elongational deformation and fluid behavior in processes is a major subject of research.

Technically relevant liquids are often complex multicomponent systems with special flow properties adjusted by adding small amounts of rheological modifier or thickener. A great number of these additional materials are commercially available, e.g., biopolymers (polysaccharides) like xanthan gum, starch, carrageenan, or especially cellulose derivatives, inorganic substances like silica or water-swellable clay, or simply synthetic polymers like polyacrylates, polyvinylpyrilidone, or polyethylene oxide (PEO) [Braun and Rosen 2000]. Therefore, understanding the elongational flow properties of such viscoelastic polymer solutions is of fundamental importance in process optimization and product development. Unfortunately, measuring the elongational viscosity of low-viscosity fluids is still a very challenging task, resulting in only a few investigations which correlate the elongational behavior of complex fluids with their application properties [Meadows et al. 1995; Kennedy et al. 1995; Ng et al. 1996; Solomon and Muller 1996; Tan et al. 2000; Stelter et al. 2002; Plog et al. 2005].

Nevertheless, a simple and versatile method for the characterization of low-viscosity fluids has been suggested more than 20 years ago [Bazilevsky et al. 1990; Entov and Hinch 1997; Bazilevsky et al. 2001], this so called capillary breakup extensional rheometer (CaBER) is even commercially available now. In this experiment, an instable liquid filament is created by applying a step strain, and the diameter of this liquid bridge is monitored as a function of time. In contrast to other techniques, CaBER allows for large Hencky strains which are of great significance to industrial practice. Unfortunately, evaluating the elongational viscosity is not trivial for CaBER experiments since no axial force is measured. Accordingly, apparent elongational viscosities are often calculated for CaBER.

In this paper, we introduce the tilted CaBER method as a simple and accurate way to determine the axial force $F(t)$ and the elongational rate $\dot{\varepsilon}$ during filament thinning at the same time by only analyzing video images. The conventional CaBER device is rotated by 90ř, and the bending of the liquid filament due to gravity is recorded using a high-speed camera. First, we describe the principles of calculating the (apparent) elongational viscosity from CaBER measurements and discuss the typical decrease of the diameter for Newtonian and viscoelastic fluids. Then, we describe how to calculate the force from the deflection of a fluid filament. After this, we present the experimental setup and give a short overview of the samples used, including preparation and characterization. Following with the experimental part, we verify the tilted CaBER method using Newtonian fluids and apply it to

22

non-Newtonian PEO solutions. Finally, concluding remarks are given.

3.2.2 Force balance for a straight vertical cylindrical thread

The axial force F in a cylindrical filament with axial orientation into the direction of gravity (here, z-direction) is assumed to be independent of the z-position, but F may depend on time. Taking into account the surface tension Γ, the normal stresses σ_{zz} and σ_{rr}, but neglecting gravity and inertia effects (see figure 3.1), the total force balances in z-direction reads as follows:
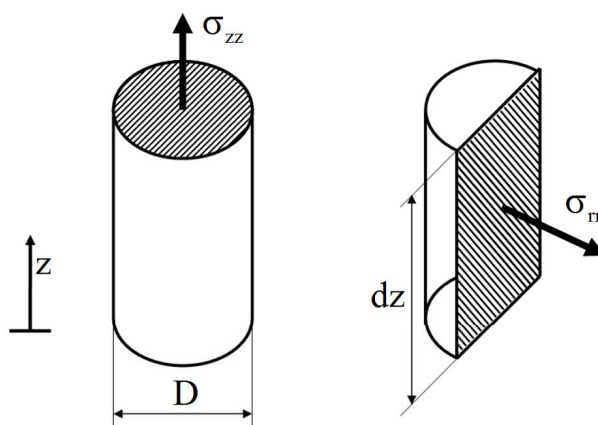
Figure 3.1: Cut filament (hatched areas) with normal stresses σ_{zz} and σ_{rr}

$$\frac{\pi}{4}\,\sigma_{zz}\,D^2 + \pi\,\Gamma\,D = F \qquad \Rightarrow \qquad \sigma_{zz} = \frac{4\,(F - \pi\,\Gamma\,D)}{\pi\,D^2}\ . \tag{3.1}$$

McKinley and Tripathi [McKinley and Tripathi 2000] used the ratio X between the true axial force F in the filament and the value resulting from the assumption $\sigma_{zz} = 0$ in order to quantify the influence of the axial normal stress σ_{zz}.

$$X = \frac{F}{F_{\sigma_{zz}=0}} = \frac{F}{\pi\,\Gamma\,D}\ . \tag{3.2}$$

For an infinitesimal volume element with length $\mathrm{d}z$ and diameter D, the force balance in r-direction reads as follows:

$$\sigma_{rr}\,D\,\mathrm{d}z + 2\Gamma\,\mathrm{d}z = 0 \qquad \Rightarrow \qquad \sigma_{rr} = -\frac{2\Gamma}{D}\ . \tag{3.3}$$

3.2.3 Calculation of the elongational viscosity

The elongational viscosity η_e for uniaxial elongational flows like, e.g., in CaBER experiments is given by Schümmer and Tebel [Schümmer and Tebel 1983]:

$$\eta_e = \frac{\sigma_{zz} - \sigma_{rr}}{\dot{\varepsilon}} \ . \tag{3.4}$$

Insertion of the axial normal stress σ_{zz} (equation 3.1) and the radial normal stress σ_{zz} (equation 3.3) into equation 3.4 results in the following expression for the true elongational viscosity valid for cylindrical or at least slender filaments:

$$\eta_e = \frac{4F - 2\pi\,\Gamma\,D}{\pi\,D^2\,\dot{\varepsilon}} \ . \tag{3.5}$$

Using the definition of the elongation rate

$$\dot{\varepsilon} = -\frac{2}{D}\frac{\mathrm{d}D}{\mathrm{d}t} \ , \tag{3.6}$$

equation 3.5 yields

$$\eta_e = \frac{\Gamma}{\mathrm{d}D/\,\mathrm{d}t} - \frac{2F}{\pi\,D\,\mathrm{d}D/\,\mathrm{d}t} \ . \tag{3.7}$$

For the sake of completeness, expressions for the radial normal stress and the elongational viscosity in case of non-cylindrical filaments are given in Appendix (chapter 3.7).

It is obvious from equation 3.7 that for calculating η_e, the diameter D and the force F are needed. Therefore, CaBER experiments with simultaneous force measurements allow for the determination of the true elongational viscosity for any fluid without assumption of special constitutive equations.

But the evaluation ofequation 3.7 is not trivial for CaBER experiments since no axial force measurement is included, and, hence, the normal stress σ_{zz} is not known. Instead, η_e is often evaluated using the assumption $\sigma_{zz} = 0$. Then an apparent elongational viscosity for CaBER experiments is obtained [Anna and McKinley 2001]:

$$\eta_{e,app} = -\frac{\Gamma}{\mathrm{d}D/\,\mathrm{d}t} \ . \tag{3.8}$$

So far, the $\sigma_{zz} = 0$ assumption has not been validated experimentally for the CaBER experiment. Deviations obviously occur for the Newtonian case [Liang and Mackley 1994; Kolte and Szabo 1999; McKinley and Tripathi 2000] and also shown in numerical simulations of the CaBER experiment using different viscoelastic or viscoplastic constitutive equations [Clasen et al. 2006a; Webster et al. 2008; Alexandrou et al. 2009].

Therefore, fluid characterization based on equation 3.8 might be helpful in comparative studies employed, e.g., for product development purposes. But especially for the determination of the true elongational viscosity from CaBER experiments, it is mandatory to measure the time-dependent axial force F during filament thinning accurately. The magnitude of this force can be roughly estimated from the force balance in axial direction equation 3.1 using the σ_{zz} assumption. Typically, Γ is in the range of $20 - 70$ mN/m, and the filament diameter decays from 1 mm to about 10 μm. This corresponds to a force range $0.5\ \mu N < F(t) < 220\ \mu N$. The first attempt to implement a force transducer into a CaBER device was done by Klein et al. [Klein et al. 2009]. They mounted a commercial quartz load cell to the fixed bottom plate of their apparatus. Due to oversampling of the force signal, a nominal sensitivity of 50 μN was reached, but calibration was only done in the force range larger than 2,000 μN. Thus, reliable force detection during capillary thinning of fluid filaments was not possible.

3.2.4 Time evolution of the filament diameter for Newtonian and weakly viscoelastic fluids

The time evolution of the diameter during capillary thinning is controlled by a balance of capillary and viscous or viscoelastic forces. Different characteristic in diameter vs. time curves are observed for different types of fluids, e.g., Bingham plastic, power law, and Newtonian or viscoelastic fluids. The midpoint diameter D_{mid} of a Newtonian fluid in a CaBER experiment decreases linearly with time t according to Papageorgiou [Papageorgiou 1995] and McKinley and Tripathi [McKinley and Tripathi 2000]:

$$D_{mid} = D_1 - \Theta \frac{\Gamma}{\eta_0} t \ , \tag{3.9}$$

where D_1 is the initial diameter of the liquid bridge at time $t = 0$ at which linear thinning of the filament sets in, Γ is the surface tension, Θ is a constant numerical factor, and η_0 is the shear viscosity. The local force balance ($\sigma_{zz} = 0$) for a thinning liquid yields $\Theta = 0.333$ if only the surface tension is considered. Papageorgiou [Papageorgiou 1995] calculated the numerical factor to $\Theta = 0.1418$ in case of negligible inertia (Reynolds number Re $\to 0$). Considering inertia (Re > 0), Eggers [Eggers 1993, 1997] and Brenner [Brenner et al. 1996] estimated the numerical factor to $\Theta = 0.0608$ and showed that this solution is valid near the filament break up.

McKinley and Tripathi [McKinley and Tripathi 2000] confirmed the numerical results of Papageorgiou ($\Theta = 0.1418$) experimentally using glycerol samples and related the factor Θ to the force ratio X (equation 3.2).

$$X = \frac{3\Theta + 1}{2} \tag{3.10}$$

The experimental validated $\Theta = 0.1418$ value corresponds to $X = 0.713$. This indicates that the axial force is not only given by the surface tension, and an additional axial normal stress must be present for Newtonian liquid filaments.

In contrast to Newtonian liquids, weakly elastic polymer solutions with concentrations $c < c_e$ form cylindrical filaments, and their diameter decreases exponentially with time in CaBER experiments [Bazilevsky et al. 1990; Entov and Hinch 1997; Anna and McKinley 2001; Arnolds et al. 2010].

$$D(t) = D_1 \left(\frac{G\, D_1}{\Gamma} \right)^{1/3} \exp\left(-\frac{t}{3\lambda_e} \right) \tag{3.11}$$

where D_1 is the initial diameter of the filament at the beginning of the exponential decrease, G is the elastic modulus, and λ_e is the elongational relaxation time, which is related to the constant elongation rate $\dot{\varepsilon} = 2/(3\lambda_e)$ (see also equation 3.6).

Exponential thinning for viscoelastic fluids can also result if an exponentially increasing normal stress is assumed instead of $\sigma_{zz} = 0$ [Clasen et al. 2006a]. Clasen et al. [Clasen et al. 2006a] stated that σ_{zz} increases with the same time constant as $D(t)$. Then equation 3.11 has to be corrected by a factor of $4^{1/3} \approx 0.63$, but the elongational relaxation time λ_e remains unaffected.

There is no simple universal relationship between this characteristic elongational relaxation time and shear relaxation time. For a series of PIB solutions, $\lambda_e \approx 3\overline{\lambda}_s$ was reported, with $\overline{\lambda}_s$ defined as an average shear relaxation time [Liang and Mackley 1994]. For PS Boger fluids with concentrations $c \approx c^*$, elongational relaxation times λ_e close to the Zimm relaxation time λ_Z were found [Bazilevskii et al. 1997]; but on the other hand, it was clearly shown for PEO as well as PS solutions that λ_e can vary drastically even at $c < c^*$ and λ_e/λ_Z values between 0.1 and 10 have been documented [Tirtaatmadja et al. 2006; Christanti and Walker 2001b, 2002b; Clasen et al. 2006a,b]. Oliveira et al. [Oliveira et al. 2006] related λ_e to the longest relaxation time λ_s estimated from small amplitude oscillatory shear and found $\lambda_e \approx \lambda_s$ for PEO solutions with $c \approx c^*$. Arnolds et al. [Arnolds et al. 2010] observed that $\lambda_e/\lambda_s \leq 1$ and strongly decreases with increasing c for PEO solutions with $c^* < c < c_e$ and attributed this to the large deformation the solutions experience during filament thinning. They used a simple factorable integral model including a single relaxation time and a damping function to calculate $\lambda_e \approx \lambda_s$ and obtained good agreement with experimental results.

Other more complex systems like surfactant solutions forming entangled wormlike micelles, polyelectrolyte complexes in solution or aggregated acrylic thickener solutions also exhibit relaxation time ratios $\lambda_e/\lambda_s < 1$, but these systems are supposed to undergo structural changes in strong elongational flow [Bhardwaj et al. 2007b; Kheirandish et al. 2008; Willenbacher et al. 2008].

Finally, it should be mentioned that PEO solutions with $c > c_e$ still form cylindrical filaments, but the time evolution of the filament diameter is no longer exponential and cannot be characterized by a single relaxation time λ_e [Arnolds et al. 2010].

3.2.5 Determination of the axial force in a horizontally stretched filament

A fluid filament is bent when gravity is acting in radial direction and the axial force within the liquid can be calculated from the bending line. Figure 3.2 shows a section of a liquid filament with infinitesimal length, ds, and the acting gravity force, dF_G. The axial force is
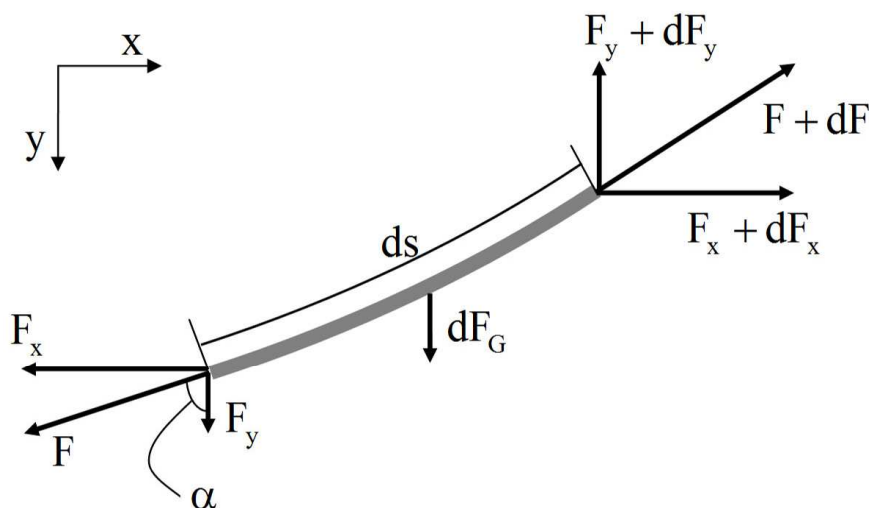

Figure 3.2: Forces in a tilted liquid thread (gray) with infinitesimal length ds

generally not constant, which is considered in the contribution of the infinitesimal force, dF, between the left and right edge of the pictured thread. In order to evaluate the axial force, all forces are balanced with respect to a (x, y) coordinate system fixed in space. Figure 3.3 presents the constructional realization of the tilted CaBER method and the bent liquid filament.

It is clearly shown in figure 3.2 that the force balances in x- and y-direction results in $dF_x = 0$ or $F_x = C_1$, where C_1 is a constant of integration and $dF_y = dF_G$. The gravity force is proportional to the volume dV and is calculated assuming constant diameter D and density ϱ:

$$dF_G = g\,dm = \varrho\,g\,dV = \frac{\pi}{4}\varrho\,g\,D^2\,ds \ . \tag{3.12}$$
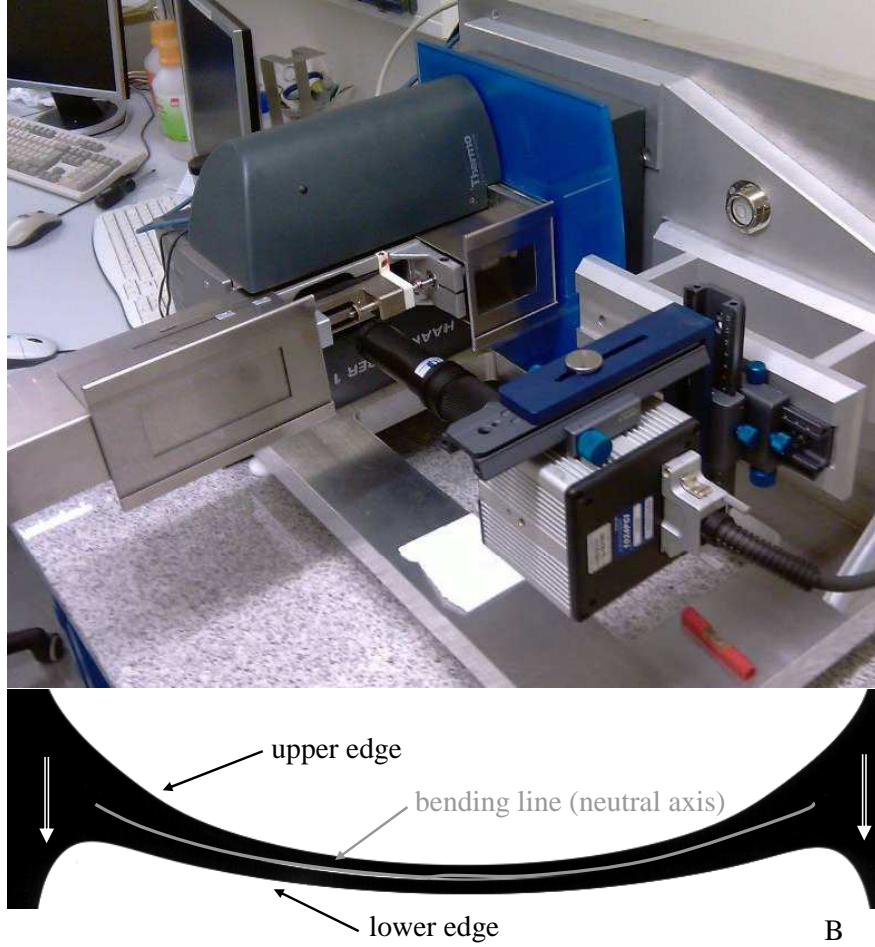
Figure 3.3: a) The constructional realization of the tilted CaBER method. b) The bent liquid filament

Furthermore, $\mathrm{d}s$ can be written as

$$\mathrm{d}s = \sqrt{(\,\mathrm{d}x)^2 + (\,\mathrm{d}y)^2} = \mathrm{d}x\sqrt{1 + \left(\frac{\mathrm{d}y}{\mathrm{d}x}\right)^2} \tag{3.13}$$

and finally

$$\frac{\mathrm{d}F_y}{\mathrm{d}x} = \frac{\mathrm{d}F_G}{\mathrm{d}x} = \frac{\pi}{4}\varrho\,g\,D^2\sqrt{1 + (y')^2}\,, \tag{3.14}$$

where y' is the first derivative of the bending line y with respect to x. The left side of equation 3.14 is obtained from the geometrical ratio

$$\frac{F_x}{F_y} = \frac{\mathrm{d}x}{\mathrm{d}y} \qquad \Rightarrow \qquad \frac{\mathrm{d}F_y}{\mathrm{d}y} = F_x\,y''\,. \tag{3.15}$$

Combining equations 3.14 and 3.15 yields the differential equation for the bending line of the so called torquefree curved beam (see also [Großet al. 2004]):

$$y'' = \frac{\pi\,\varrho\,g\,D^2}{4F_x}\sqrt{1 + (y')^2}\,. \tag{3.16}$$

We use the substitutions $y' = u$ and $y'' = u'$ to solve the differential equation 3.16, and we choose the position of maximum deflection as point of reference to calculate the constants of integration. Thus, we get the second derivative of the bending line y'' as a function of the x-position and the force component F_x:

$$y'' = \frac{\pi \, \varrho \, g \, D^2}{4F_x} \cosh\left(\frac{\pi \, \varrho \, g \, D^2}{4F_x} x\right) \; . \tag{3.17}$$

The absolute value of the force F can be calculated as a function of F_x and x analogous to the approach taken in equation 3.13, using equation 3.15 and the identity $\cosh^2(\varphi) - \sinh^2(\varphi) = 1$.

$$F = F_x \cosh\left(\frac{\pi \, \varrho \, g \, D^2}{4F_x} x\right) \tag{3.18}$$

Equations 3.17 and 3.18 can be developed in Taylor series. Taking into account the first two terms $(O(2))$, the axial force F is no longer a function of the position x and is given by

$$F = \frac{\pi \, \varrho \, g}{4w''} D^2 \; . \tag{3.19}$$

For sake of clarity, we use the symbol w for the approximated bending line and w'' for its second derivative.

The data evaluation is based on a least square approximation of the bending line by using a second order polynomial and calculating the constant second derivative w'' to be inserted in equation 3.19 However, a constant diameter is assumed so far. This disadvantage can be avoided using the deflection of the liquid thread instead of the curvature of the bending line. Then, integrating equation 3.19 twice yields the following relationship between the axial force and the diameter $D(t, x)$:

$$F = \frac{\pi \, \varrho \, g}{4w} \int\limits_0^x \int\limits_0^{\tilde{x}} D(\hat{x})^2 \; \mathrm{d}\hat{x} \, \mathrm{d}\tilde{x} \; . \tag{3.20}$$

The double integral in equation 3.20 can be solved numerically without any fitting of the bending line or any other assumptions.

We estimate the approximation error, which may be defined as follows:

$$\beta = 1 - \frac{w}{y} \tag{3.21}$$

where y is the true and w the approximated bending line. For given F and D, F_x is calculated numerically in order to estimate the approximation error β. Lines of constant β are shown in figure 3.4 for a cylindrical fluid filament with density $\varrho = 1$ g/cm^3 and length $2x = 12$

mm. For the experiments presented here, β was always below 0.1%. It should be noted that the length of the filament has a drastic influence on the approximation error. For example, doubling the length of the filament to 24 mm while leaving the other parameters unchanged results in $1\% < \beta < 10\%$.
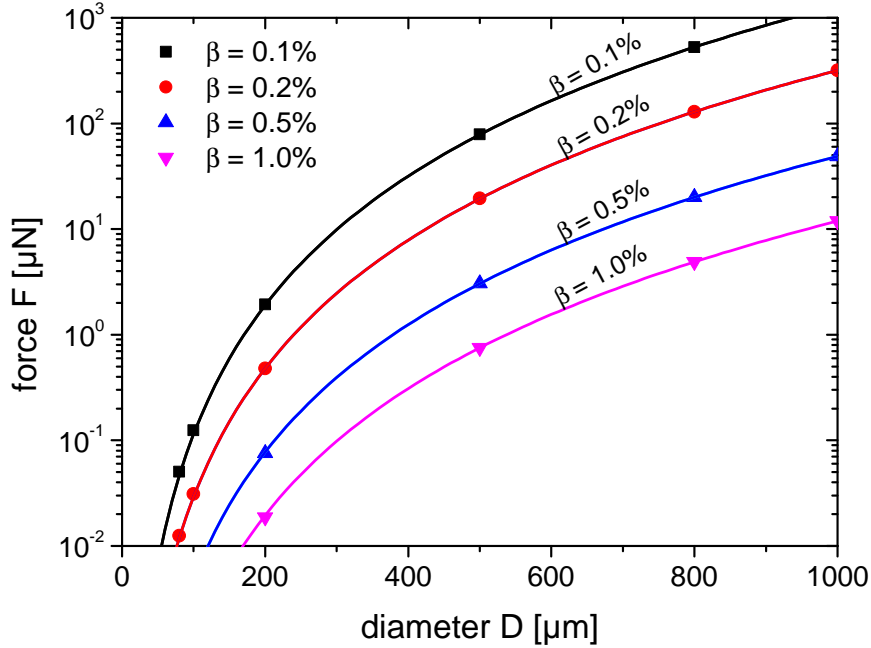

Figure 3.4: Lines of constant approximation error $\beta = 1 - w/y$ in the force-diameter plane

3.3 Experimental realization

3.3.1 The (tilted) CaBER device

The tilted CaBER method has been realized by mounting a commercial CaBER-1 (Thermo Scientific, Karlsruhe) on a customized L-shaped aluminum construction in order to rotate the whole device by 90ř, as shown in figure 3.3a. Thus, the liquid thread is stretched in horizontal direction and bents due to the action of gravity (figure 3.3b).

The device is equipped with plates of diameter $D_0 = 6$ mm. The liquid bridge is created by separating the plates from a displacement of $h_i = 0.51$ mm or $h_i = 0.75$ mm to a final displacement of $h_f = 6.5$ mm or $h_f = 11.5$ mm within a constant strike time of $t_s = 40$ ms. The upper plate or, in case of the tilted experiment, the left plate reaches its final position at time $t_1 = t_0 + t_s$ where the filament diameter is referred to $D_1 = D(t_1)$. This notation considers the mismatch between time t_0 when the experiment starts and time t_1 when the capillary thinning begins. The thinning of the filament is recorded using a high-

speed camera (Photron Fastcam-X 1024 PCI), a telecentric objective (MaxxVision TC4M 16, magnification: x1) and a blue telecentric background light (Vision and Control, TZB30-B) as described by Niedzwiedz et al. [Niedzwiedz et al. 2009]. The experimental setup allows observations within a resolution of 1,024 x 1,024 px (1 px $\approx$ 16 μm) and a frame rate of 1,000 fps. We assume that at least two pixels are needed for a reliable determination of the filament diameter, and we do not consider diameters lower than 32 μm. Each individual image is analyzed in order to determine the upper and lower edge of the filament. Here, we have taken care that edges are detected properly correct without any impaired results, which can occur due to pixel fault (too bright or dark pixel) of the camera or defective image recognition. Therefore, we have implemented an automatic procedure in MATLAB to examine each image individually relating to two aspects: the absolute value of the determined filament diameter must be lower than the diameter of the plates used and the maximum acceptable slope of the diameter is $(\mathrm{d}D/\mathrm{d}x)_{max} = 0.1$. All data points which do not satisfy these conditions are ignored in subsequent calculations.

Therewith, the experimental determined bending line or neutral axis (see also figure 3.3b) is calculated to apply equations 3.19 and 3.20 for the force calculation. The neutral axis is named W, this experimental value corresponds to the model value w in the case of the approximated theory and y in the case of the general theory. Regardless of the applicability of equations 3.19 and 3.20, which will be discussed in more details below, the force calculation from the bending line (equation 3.20) requires a further treatment of the measured data. The insufficient horizontal adjustment of the CaBER device in a range of a few micrometers and a shear flow perpendicular to the axial filament direction (double arrows in figire3.3b) in the contact areas between the fluid filament and the CaBER-plates (which can differ for each plate) induced a different position of filament for the left and the right edge in the tilted experiment. Therefore, we carried out a baseline correction for our data, which is based on the assumption of filament symmetry relative to the point of maximum deflection and contains the following strategy. We calculate the first derivative of the filament diameter $\mathrm{d}D/\mathrm{d}x$ and determine the section where $\mathrm{d}D/\mathrm{d}x < 0.01$. The two discrete $\mathrm{d}D/\mathrm{d}x$ values which are nearest to 0.01 are named L_1 for the left side and R_1 for the right side of the filament (figure 3.5a). These values define the borders for the baseline correction. Then the next five points in positive x-direction are considered, and the average value $W_L = \sum_{i=1}^{5} W(L_{1+i})/6$ is calculated; then $W_R = \sum_{i=1}^{5} W(R_{1-i})/6$ is obtained analogously averaging over six points starting from $W(R_1)$ going into negative x-direction. Finally, the baseline BL is defined as the line connection of W_L and W_R (figure 3.5b). Then the corrected bending line Wcorr is calculated according to $W_{corr} = W - BL$ and the lowest point of W_{corr} is chosen as point of reference so that $(W_{corr})_{min} = 0$ is guaranteed. Finally, the force is calculated applying

equation 3.20. It has to be noted that the baseline correction has no visible influence for the force calculation based on equation 3.19.
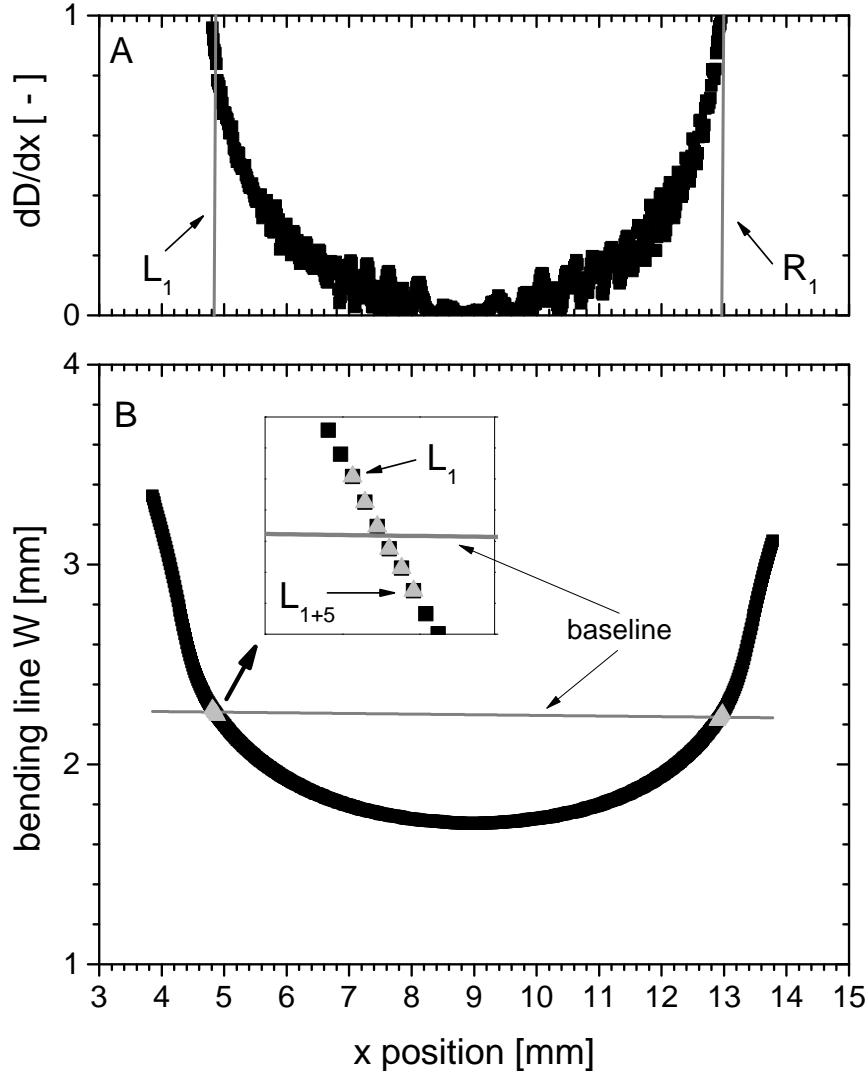
Figure 3.5: a) Derivation of the diameter with the determined left edge, L_1, and right edge, R_1. b) Experimentally determined bending line W as a function of x-position. The gray lines represent the baseline BL calculated from L_1 to L_{1+5} and R_{1-5} to R_1 data points

3.3.2 Sample preparation and characterization

In this study, we used two different Newtonian model systems and one viscoelastic system. The first Newtonian system was composed of fructose (Carl Roth GmbH, Karlsruhe, Germany) solutions with mass fractions between 76 and 81 % in an aqueous mixture of 0.1 wt. % Tween20 (Carl Roth GmbH, Karlsruhe, Germany). The samples were stirred and heated

for 3 h using a magnetic stirrer and were measured within 2 days to prevent recrystallization of the highly concentrated solutions ($c \geq 80$ %). Zero shear viscosities eta_0 were determined from steady state measurements using a MARS II rotational rheometer (Thermo Scientific) equipped with cone plate geometry (60/35 mm in diameter and 1° cone angle) at 20 °C.

The surface tension (measured with a platinum-iridium Wilhelmy-plate mounted on a DCAT 11, DataPhysics tensiometer) was constant for all samples within experimental error and was determined to $\Gamma \approx 62.8$ mN/m, which is approximately 20 mN/m lower than the surface tension of the pure aqueous fructose solutions. Therefore, the addition of surfactant has two effects: the filament lifetime of the fructose solutions is increased and the surface tension exhibits the same value as for the PEO solutions describe below. The second Newtonian system were mixtures of silicon oil AK50000 in AK1000 (both Wacker Chemie AG, Munich, Germany) with mass fractions between 0 and 100 %. Silicon oils are obviously non-Newtonian fluids, but they exhibit Newtonian flow behavior in CaBER experiments because the longest relaxation time λ_s is much smaller than the filament lifetime (compare figure 3.8 and data in table 3.1). The elasto-capillary number Ec [Anna and McKinley 2001; Clasen 2010] provides a quantitative criterion to estimate this effect.

$$\mathrm{Ec} = \frac{2\lambda_s \, \Gamma}{\eta_0 \, D} \tag{3.22}$$

It compares the viscous timescale $t_v = \eta_0 \, D/2\Gamma$ with the timescale of elastically controlled thinning, assumed as the longest shear relaxation time λ_s which was determined by small amplitude oscillatory shear experiments according to

$$\lambda_s = \lim_{\omega \to 0} \frac{G'}{G'' \, \omega} \tag{3.23}$$

using a Physica MCR 501 (Anton Paar) equipped with cone plate geometry (50mm diameter and 1° cone angle) at 20 °C.

Elastically driven capillary thinning sets in when $\mathrm{Ec} \approx 1$. For the silicon oil mixtures investigated here, the maximum elasto-capillary number Ec_{max} were calculated using the minimal observable diameter of $D_{min} = 32$ μm. In all cases investigated here, $\mathrm{Ec}_{max} << 1$ was detected, corresponding data are summarized in table 3.1.

Therefore, silicon oils are a useful Newtonian model system for CaBER experiments. The surface tension was only measured for pure AK1000 due to the high viscosity of the other samples, and we assumed a constant surface tension for all silicon oil mixtures. PEO solutions with polymer mass fractions between 1 and 5 % were used as viscoelastic model system. The polymer powder (Aldrich Chemical Co., UK) had a weight average molecular weight of $M_w = 10^6$ g/mol and was dissolved in distilled water by means of shaking. The samples were

stored at 7 °C up to the point of measurement. The surface tension of the PEO solutions is $\Gamma \approx 62.4$ mN/m and independent of polymer concentration up to $c \approx 4$ %. A lower surface tension was observed for higher polymer concentration, probably due to systematic errors inferred from the high sample viscosity.

All data, including the density of the samples determined using a pycnometer with a total volume of 10.706 cm^3 at 20 °C, are summarized in table 3.1.

**Table 3.1:** Physical properties of the measured model systems

Type	$c/$ %	$\eta_0/$Pas	$\lambda_s/$ms	$\Gamma/$mN/m	$\varrho/$g cm^{-3}	Ec$_{max}$
Fructose/Tween20	76.0	0.88 ± 0.01	-	61.8 ± 2.3	1.380	-
	77.0	1.19 ± 0.03	-	64.4 ± 1.9	1.385	-
	78.0	1.64 ± 0.08	-	62.2 ± 0.7	1.390	-
	79.2	2.47 ± 0.05	-	61.9 ± 0.3	1.398	-
	80.0	3.59 ± 0.07	-	62.0 ± 0.8	1.402	-
	81.0	5.00 ± 0.11	-	62.4 ± 0.6	1.420	-
AK50000	0	1.04 ± 0.01	0.19 ± 0.05	20.8 ± 0.5	0.972	0.2
	20	2.97 ± 0.01	0.82 ± 0.07			0.4
	40	8.11 ± 0.07	1.71 ± 0.03			0.3
	60	17.68 ± 0.23	3.26 ± 0.05			0.2
	80	34.11 ± 0.41	4.63 ± 0.12			0.2
	100	60.27 ± 1.18	5.97 ± 0.10			0.1
PEO 10^6 g/mol	1.0	0.04 ± 0.01	9.7 ± 1.3	61.7 ± 0.6	0.992	935
	1.5	0.14 ± 0.02	26 ± 2	62.7 ± 0.3	0.992	728
	2.0	0.38 ± 0.01	54 ± 3	61.7 ± 0.4	0.991	548
	2.5	0.94 ± 0.02	110 ± 8	62.8 ± 0.1	0.994	459
	3.0	2.01 ± 0.06	189 ± 8	62.8 ± 0.6	0.993	369
	3.5	4.10 ± 0.17	340 ± 15	62.5 ± 0.2	0.994	324
	4.0	8.58 ± 0.30	425 ± 21	62.8 ± 0.4	0.996	194
	4.5	12.97 ± 0.43	635 ± 27	61.0 ± 0.8	1.000	187
	5.0	25.46 ± 0.66	1005 ± 31	57.5 ± 0.5	1.005	142

3.4 Results and discussion

3.4.1 Validation of the force calculation method

Figure 3.6 shows typical results of force calculation from gravity-driven bending of horizontally stretched fluid filaments as a function of diameter.
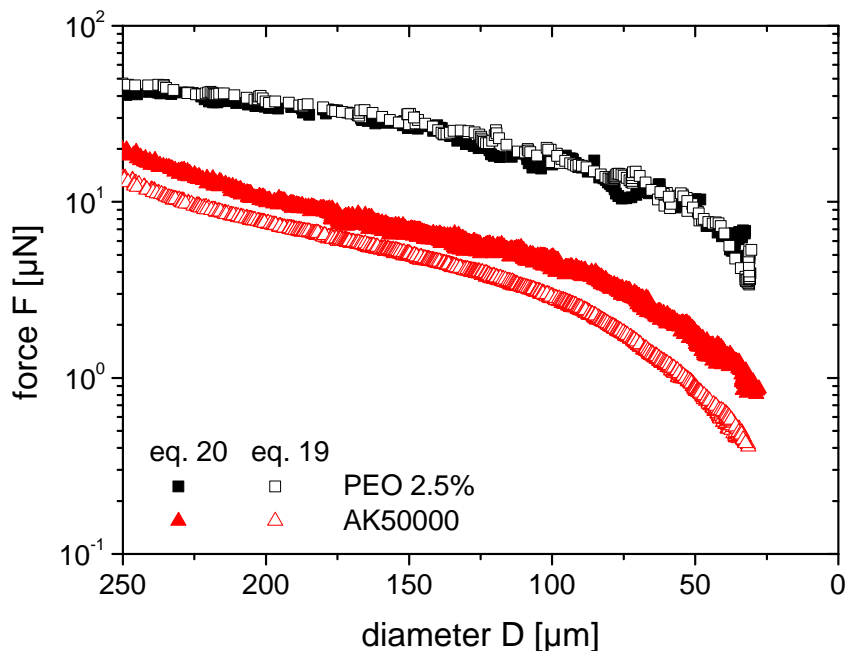

Figure 3.6: Measured force F as a function of the diameter for the end of the filament thinning (measurement properties, $h_i = 0.51$ mm, $h_f = 11.5$ mm). Closed symbols represent data evaluation, using equation 3.20; and open symbols represent data evaluation, using equation 3.19, for a 2.5 % PEO solution (squares) and silicon oil AK50000 (triangles)

The squares represent the 2.5 % PEO solution which behaves like a typical weakly viscoelastic fluid, indicated by a cylindrical thread in the CaBER experiment. The forces calculated using equation 3.20 (open symbols) and equation 3.19 (closed symbols) are identical within experimental uncertainty. Therefore, the simplified force calculation method, and particularly the parabolic fit of the bending line, yields good results as long as the thread is cylindrical.

The Newtonian silicon oil AK50000 forms slightly concave filaments. The calculated forces (triangles in figure 3.6) differ from each other due to the non-constant diameter. The force values calculated using the numerical integration of the diameter (equation 3.20), represented by closed symbols, are significantly larger than the force values calculated byequation 3.19 with the assumption of constant diameter (open symbols). The corresponding Trouton ratios

Tr defined as the ratio of the true elongational viscosity, calculated by applying equation 3.7, and the shear viscosity are Tr = 3.2 when the force is calculated according to equation 3.20 and Tr = 2.0 if equation 3.19 is applied. Of course, the correct Trouton ratio is three for a Newtonian fluid. This demonstrates that the filament curvature has to be taken into account for non-cylindrical filaments and as a consequence, we determine the force only by applying equation 3.20 for all cylindrical and noncylindrical threads. Figure 3.7 (left) shows
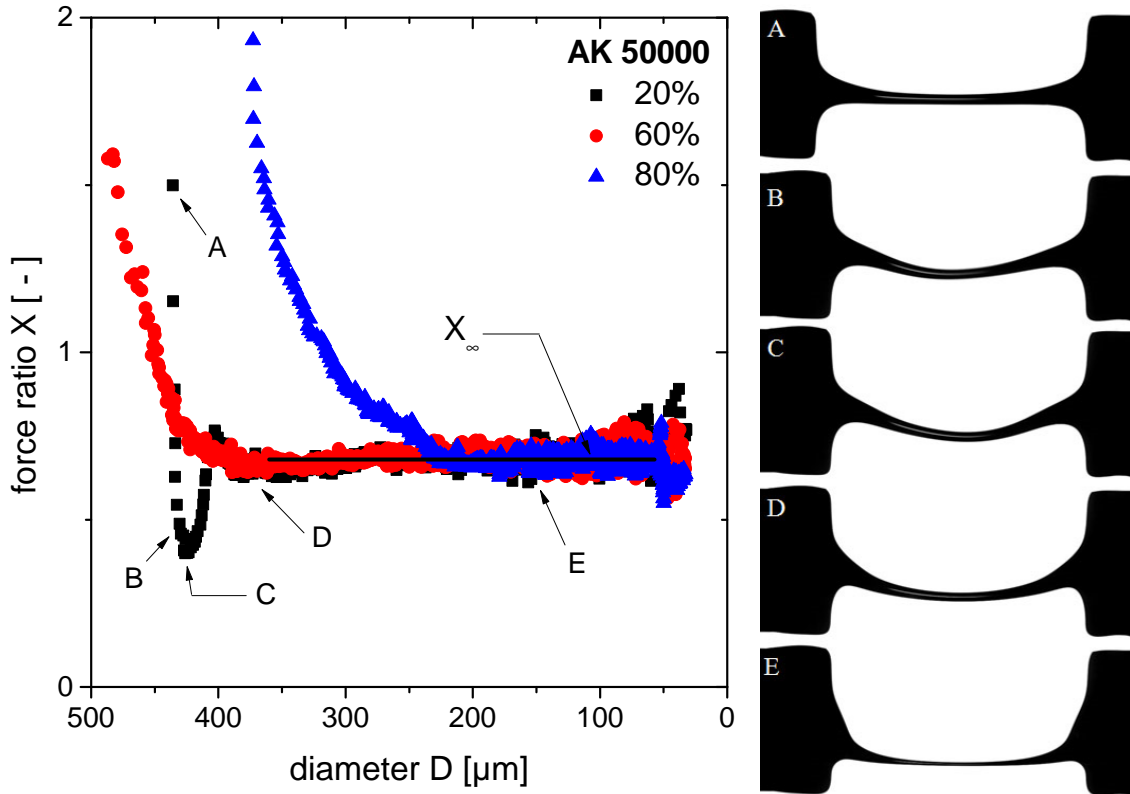
Figure 3.7: Left: Force ratio as a function of diameter for AK50000 in AK1000 mixture for three different concentrations given in the diagram. Right: Image sequence of the deflection during the capillary breakup in the tilted CaBER experiment for the 20 % AK50000 mixture

the force ratio X as a function of diameter calculated directly from the force measurements according to equation 3.2 for three silicon oil mixtures.

For all samples investigated here, X strongly decreases with decreasing diameter to a constant final value X_∞. This decrease is associated with the initial deflection of the liquid tread. The critical filament diameter, where X_∞ is reached, is shifted to lower values with increasing AK50000 concentration and correspond to the inflection point of the filament diameter vs. time curves, shown in figure 3.8.
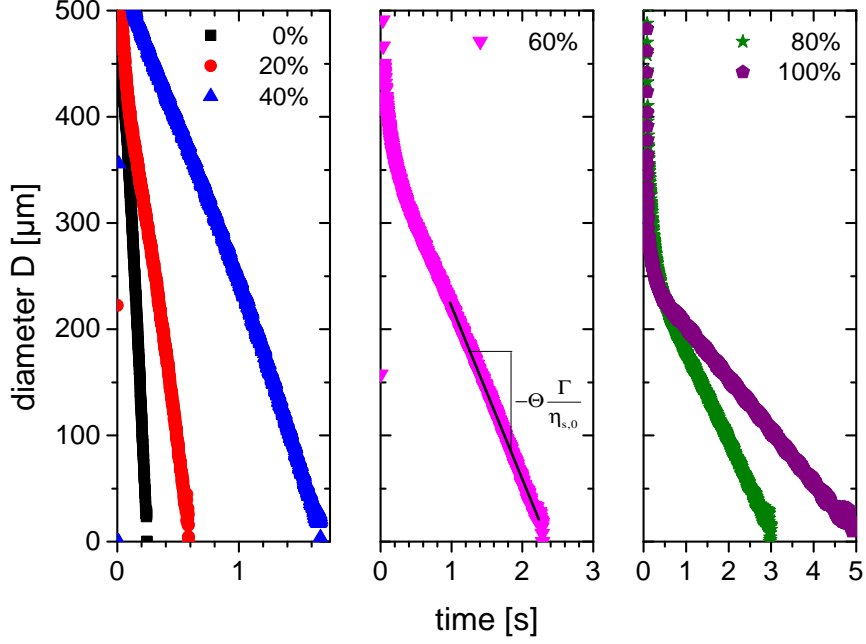
Figure 3.8: Diameter as a function of time for the AK50000 in AK1000 mixtures ($h_i = 0.51$ mm, $h_f = 11.5$ mm)

The low viscous silicon oil mixture including of 20 % AK50000 additionally exhibits a sharpminimum before the constant X_∞ value is reached. This initial variation of X is attributed to a wave traveling through the filament after the plates have reached their final position. This wave results in a shift of the point of maximum deflection as shown in the images in figure 3.7. Image D where the filament deflection is symmetric corresponds to the diameter where X_∞ is reached. This finding is typical for low viscous Newtonian fluids with $\eta_0 < 15$ Pas. For the viscoelastic PEO solutions investigated here, a wave through the filament was only observed at a zero shear viscosity of $\eta_0 = 0.04$ Pas, corresponding to a concentration of 1.0 %. This phenomenon did not occur for solutions with higher PEO concentrations and this is attributed to the well-known stabilization effect of the stretched polymer coils [Lenczyk and Kiser 1971; Tirtaatmadja et al. 2006].

The consideration of the final force ratio allows for another way for the validation of the force calculation method. On one hand, X_∞ is determined directly from the force measurement as described above. On the other hand, X_∞ can also be calculated from the slope of $D(t)$ which is proportional to $-\Theta\Gamma/\eta_0$ (see figure 3.8, as expected for Newtonian fluids. Using equation 3.10 and the additionally measured zero shear viscosity, the numerical factor Θ is linked to the force ratio X_∞.

Figure 3.9 shows the experimentally determined force ratios, as a function of viscosity for the two series of Newtonian fluids. Here, silicon oil mixtures (squares) were measured with an
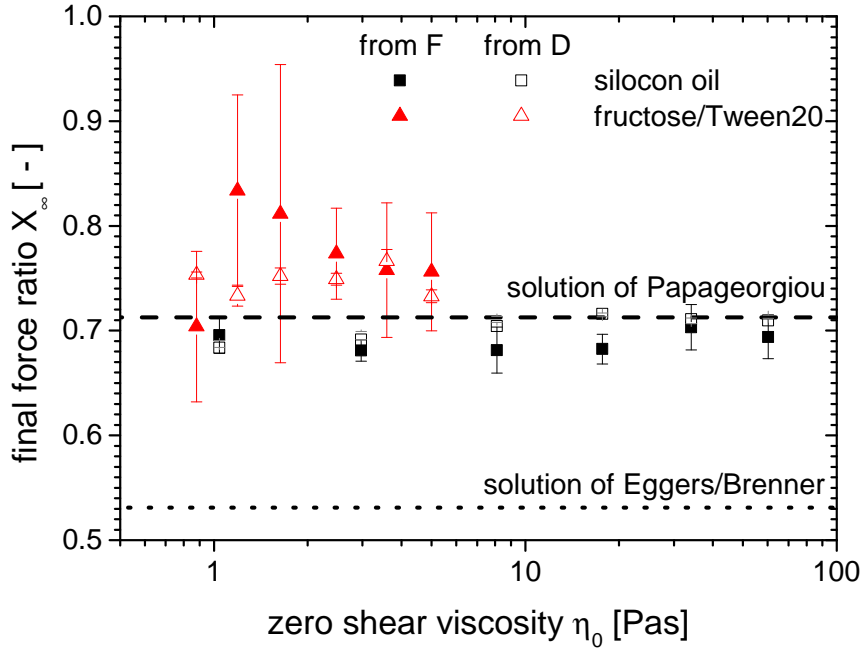
Figure 3.9: Force ratio as a function of zero shear viscosity for silicon oil mixtures ($h_i = 0.51$ mm, $h_f = 11.5$ mm) and fructose/Tween20 solutions ($h_i = 0.75$ mm, $h_f = 6.5$ mm). The filled symbols represent X_∞ values using the calculated force, and the open symbols represent X_∞ values using the diameter

initial height of $h_i = 0.51$ mm and a final height of $h_f = 11.5$ mm and the fructose/Tween20 solutions (triangles) were measured with $h_i = 0.75$ mm and $h_f = 6.5$ mm. The large scale error bars of the fructose/Tween20 solutions are caused by the high capillary velocity Γ/η_0, and, hence, a short filament lifetime. The force ratio values determined from the diameter (open symbol) and the force (filled symbols) using equation 3.20 are identical within experimental error. Considering all force measurement experiments, we obtain an average force ratio $X_\infty = 0.728 \pm 0.059$, which is in excellent agreement with the solution of Papageorgiou [Papageorgiou 1995] and which is far away from the solution of Eggers [Eggers 1993, 1997] and Brenner et al. [Brenner et al. 1996]. All these experiments validate the tilted CaBER method including the force calculation from equation 3.20 as an accurate and robust method for the determination of the axial force in a fluid filament during capillary thinning elongational flow.

3.4.2 Sign of the axial normal stress

From a theoretical point of view, the minimum $\sigma_{zz}/|\sigma_{rr}|$ value is -1 because lower values would result in negative elongational viscosities. Figure 3.10 shows the dimensionless normal stress ratio $\sigma_{zz}/|\sigma_{rr}|$ as a function of diameter for a silicon oil mixture of 60 % AK50000 in

AK1000 (filled squares) and a 3.5 % PEO solution (open triangles).
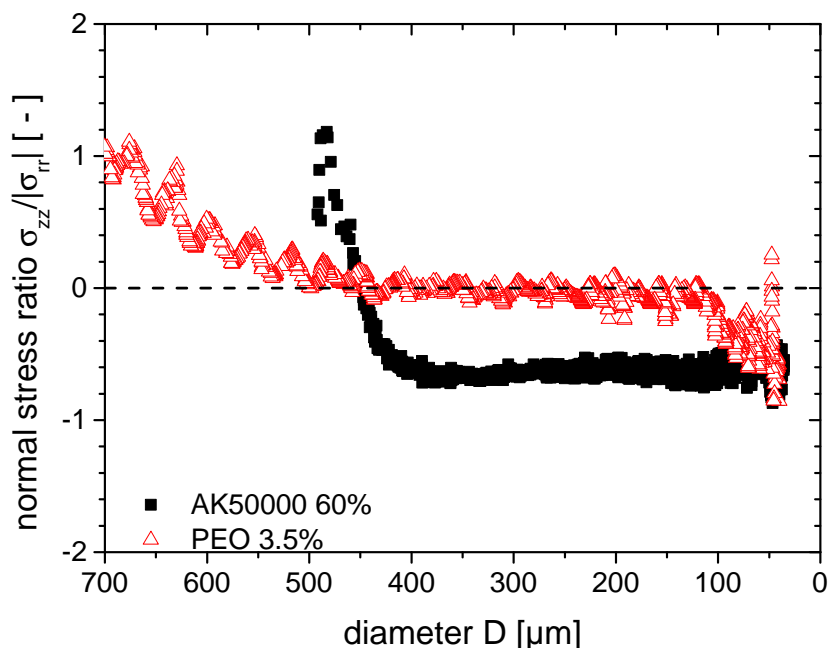
Figure 3.10: Normal stress ratio for a 3.5 % PEO 10^6 g/mol solution (f illed squares) and a 60 % AK50000 mixture (open triangles)

During the initial thinning period dominated $\sigma_{zz}/|\sigma_{rr}|$ strongly decays in both cases. This decay is faster for fluids of lower viscosity and is presumably due to inertial effects. After this induction period $\sigma_{zz}/|\sigma_{rr}|$ reaches a constant value $\sigma_{zz}/|\sigma_{rr}| = -0.54 \pm 0.12$ for all Newtonian fluids. The negative sign corresponds to a compressive stress, which causes the pronounced deflections of Newtonian filaments. Such compressive stresses are not observed for the PEO solutions and, hence, the deflection is less pronounced compared to the Newtonian samples discussed in the previous section. The induction period is much shorter for all the investigated PEO solutions than for the silicon oils due to the damping properties of the polymer coils Accordingly, the asymptotic value for the normal stress ratio is reached much faster. A limiting value $\sigma_{zz}/|\sigma_{rr}| \approx 0$ is observed for the PEO solutions with concentrations lower than 4 %. For these sparsely concentrated solutions, it is not possible to check the assumption of Clasen et al. [Clasen et al. 2006a] that σ_{zz} increases exponentially due to the measuring accuracy and the scatter of the data points. Anyway, σ_{zz} must be significantly smaller than σ_{rr}, and in this case, the widely used assumption $\sigma_{zz} = 0$ obviously is valid for the evaluation of the elongational viscosity from CaBER measurements. But constant values $\sigma_{zz}/|\sigma_{rr}| > 0$ are observed for higher polymer concentrations as discussed in the next section. This finding is the experimental proof of significant exponentially increasing axial

normal stresses as predicted by Clasen et al. [Clasen et al. 2006a].

$$\frac{\sigma_{zz}}{|\sigma_{rr}|} = \text{const.} \qquad \Rightarrow \qquad \sigma_{zz} \propto \exp\left(\frac{t}{3\lambda_e}\right) \tag{3.24}$$

The normal stress ratio is related to the force ratio X discussed in the previous section. The force balance (equations 3.1 and 3.3) yields:

$$\frac{\sigma_{zz}}{|\sigma_{rr}|} = 2\left(\frac{F}{\pi\,D\,\Gamma} - 1\right) \tag{3.25}$$

Combining equation 3.25 with the definition of the force ratio (equation 3.2) results in

$$X = \frac{1}{2}\frac{\sigma_{zz}}{|\sigma_{rr}|} + 1 \tag{3.26}$$

Therefore, the sign of σ_{zz} is obvious from the force ratio, as discussed above. For vanishing axial stresses, the force ratio is one. $X < 1$ values correspond to a compressive axial normal stress, and $X > 1$ values correspond to a tensile normal stress.

3.4.3 Applying the tilted CaBER method to non-Newtonian fluids

Recently, the behavior of semi-dilute and concentrated entangled PEO solutions in regular CaBER experiments has been discussed in detail [Arnolds et al. 2010]. They obtained $c^* \approx 0.4$ % and $c_e \approx 2.5$ % for PEO with $M_w = 10^6$ g/mol from their steady and small amplitude oscillatory shear experiments. Here, we focus on the variation of the axial force in this concentration range investigating PEO solutions with concentrations between 1 % and 5 %.

The filament lifetime of these PEO solutions strongly increases with polymer concentration. Diameter data are shown in figure 3.11a. The PEO solutions with $c < 4$ % exhibit the typical exponential thinning (lines in figure 3.11a), with characteristic relaxation time λ_e, calculated according to equation 3.11. For higher polymer concentrations, the filaments are still cylindrical but do not exhibit an exponential thinning regime and, hence, λ_e cannot be determined. The findings are in good agreement with Arnolds et al. [Arnolds et al. 2010]. Corresponding force measurement data are shown in figure 3.11b. The force F decreases monotonically with time to a minimal value of about 1 μN.

Calculated force ratios as a function of diameter D for PEO solutions with $c = 3.5$ % and $c = 5.0$ % as well as for the Newtonian silicon oil mixture AK50000 60 % are shown in figure 3.12a.
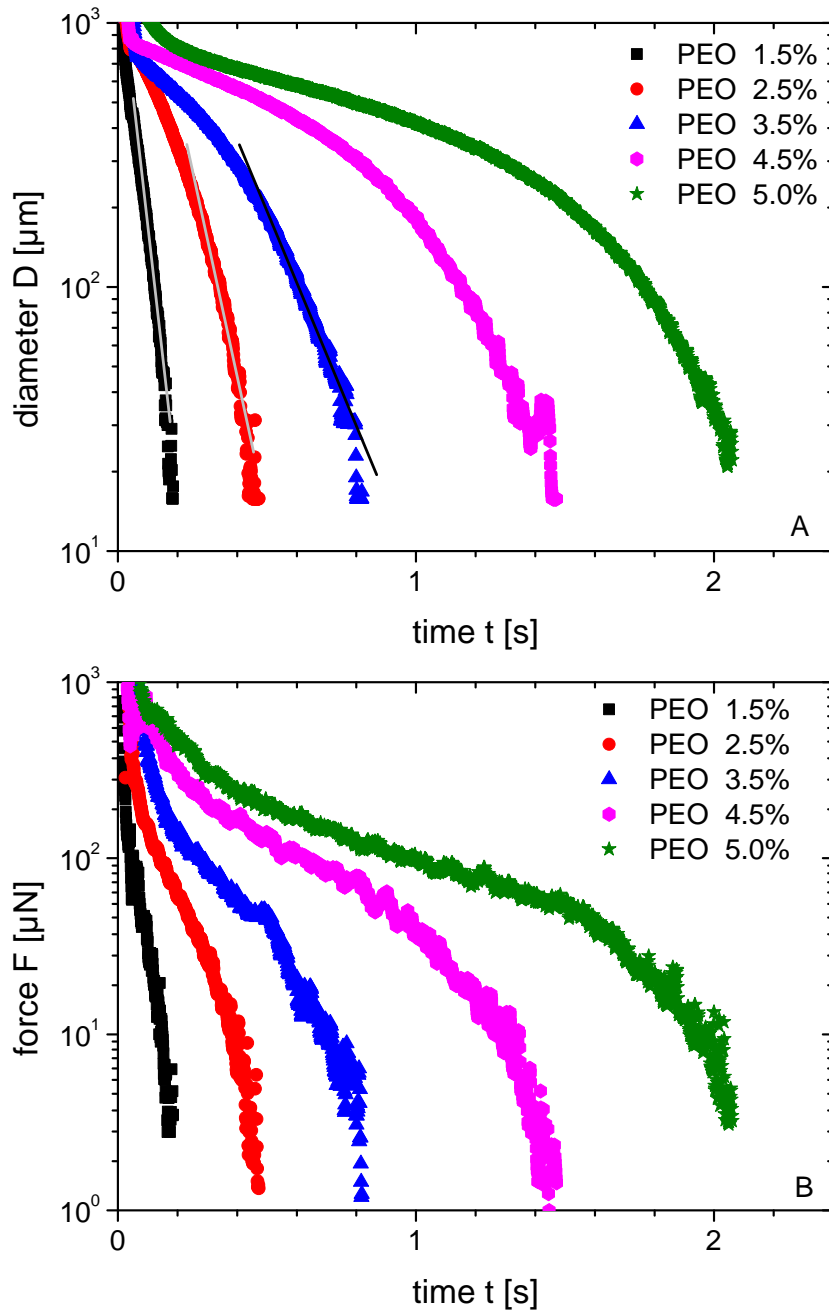
Figure 3.11: PEO solutions CaBER measurements (measurement properties, $h_i = 0.51$ mm, $h_f = 11.5$ mm). a) Diameter as a function of time. The lines represent exponential fits to the data. b) Force as a function of time

The measured force ratios for the PEO solutions investigated here are always higher than the force ratio for the Newtonian liquid. Remarkably, this finding disagrees with the observation of Clasen [Clasen 2010] for capillary breakup of semi-dilute polymer solutions. He observed that the thinning process splits up into four regimes: (1) early thinning which is controlled by

gravitational sagging; (2) Newtonian thinning behavior (viscocapillary) described by equation 3.9; (3) extensional thinning (still viscocapillary) described by a power law; and finally (4) elasto-capillary thinning described by equation 3.11.
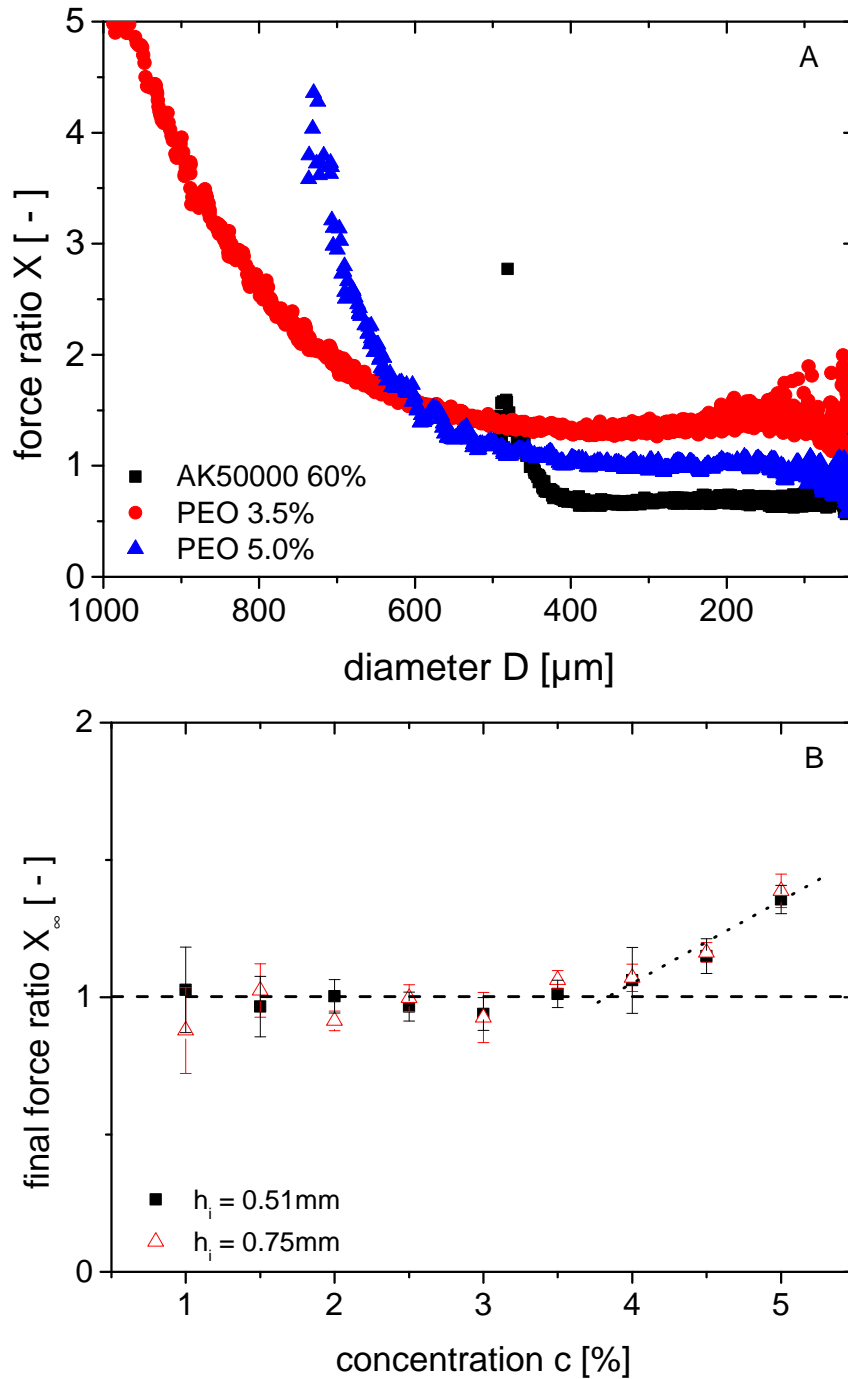
Figure 3.12: a) Force ratio as a function of diameter. b) Final force ratio as a function of concentration c for two different initial heights $h_i = 0.51$ mm (filled squares) and $h_i = 0.75$ mm (open triangles). The dashed line represents a vanishing axial normal stress

It is clearly shown in figure 3.12a that the $X(D)$ data do not support the existence of Newtonian thinning regime because the Newtonian limit of $X_\infty = 0.728 \pm 0.059$ is never reached during the thinning process. This emphasizes that the interpretation of the $D(t)$ data (figure 3.11a) as, e.g., done by Clasen [Clasen 2010] is not unambiguous since the corresponding force ratio is not considered. Therefore, the force measurement gives additional information for the interpretation of the thinning behavior of liquid filaments.

The extracted final force ratios X_∞ versus concentration c for the investigated PEO solutions are shown in Ffigure 3.12b. Remarkably, this ratio is one for the clearly elasto-capillary exponentially thinning solutions ($c < 3.5$ %). $X_\infty = 1$ means that there is no axial stress in the filament during capillary thinning. Therefore, the simplified approach of calculating the elongational viscosity according to equation 3.8 is valid for these weakly elastic PEO solutions. However, the final force ratio deviates significantly from $X_\infty = 1$, indicating that $\sigma_{zz} \neq 0$ and increases monotonically for concentrations $c \geq 4$ %. Non-vanishing σ_{zz} values for non-Newtonian fluids are directly detected here for the first time performing CaBER experiments. This clearly indicates the limitations of the widely used, simplified data analysis for calculating the elongational viscosity (equation 3.8) and demonstrates that an accurate force measurement is mandatory for a determination of absolute η_e values (equation 3.7) from CaBER experiments.

The concentration where X_∞ begins to differ from unity ($c = 4$ %) is much greater than the overlap concentration of c^* and roughly coincides with the entanglement concentration c_e. It seems that a significant axial normal stress is due to the entanglements present in these solutions and gives rise to the observed nonexponential thinning of the filament diameter.

In figure 3.13, the elongational viscosity η_e obtained from the force measurement is compared to the apparent elongational viscosity $\eta_{e,app}$ calculated fromΓ and $D(t)$ using the $\sigma_{zz} = 0$ assumption for a 4.0 % PEO solution (3.13a) and a 5.0 % PEO solution (3.13b). Here, we have smoothed the diameter data applying the floating average method in order to calculate the elongation rate numerically.

In the initial period of capillary thinning right after the upper plate has reached its final position ($t > t_1$), the elongational viscosity η_e obtained from the force measurements goes through a sharp maximum, which does not appear in $\eta_{e,app}$. Similar results were obtained for all PEO solutions investigated here, but the apparent viscosity maximum is less pronounced for PEO solutions with higher polymer concentration. The physical interpretation of this phenomenon is not yet clear, but it might be due to inertial effects as already discussed above (see chapter 3.4.1 and chapeter 3.4.2). It also has to be noted that the elongation rate goes through a distinct minimum during this period of thinning. This topic requires further investigations which are beyond the scope of this paper.
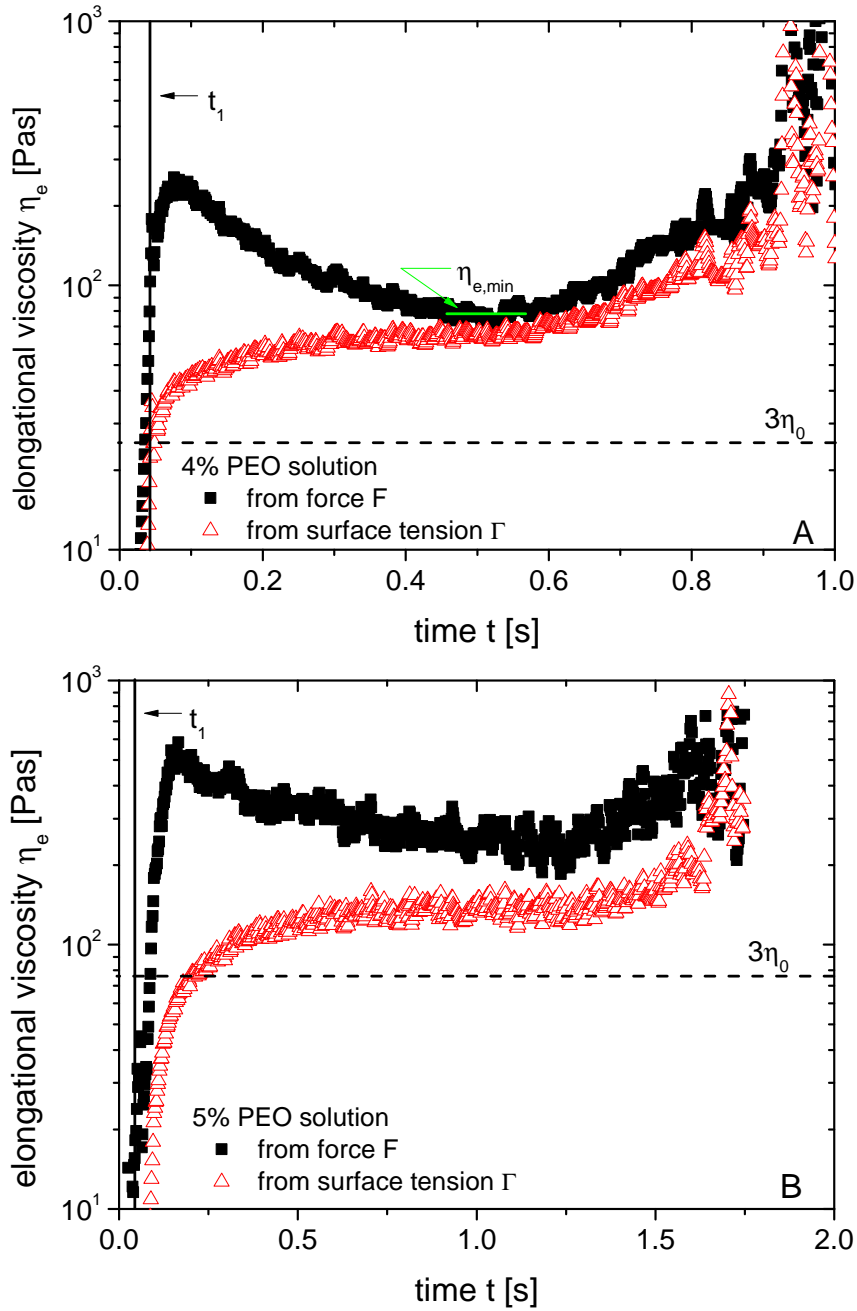
Figure 3.13: Elongational viscosity as a function of time (measurement parameters, $h_i = 0.75$ mm, $h_f = 11.5$ mm), calculated from force measurement data according to equation 3.7 (filled squares) and the surface tension equation 3.8 assuming $\sigma_{zz} = 0$ (open triangles).a) 4.0 % PEO solution. b) 5.0 % PEO solution

The time when η_e reaches its minimum corresponds to the time when the force ratio X reaches its limiting value. For the PEO solutions with $c \leq 4$ %, the time also corresponds to the inset of the exponential thinning. In this case, the limiting value is independent of polymer concentration ($X_\infty = 1.1 \pm 0.1$). During the final stage of capillary thinning, both

elongational viscosity values η_e and $\eta_{e,app}$ strongly increase during the capillary thinning due to the well-known progressive entropic resistance to the deformation of the polymer chains; but in this case, $\eta_{e,app}$ is a reasonable approximation for the true elongational viscosity. For the 5 % PEO solution with $X_\infty > 1$, the apparent elongational viscosity during the final stage of thinning is significantly lower than the true value obtained from the force measurements.

3.5 Conclusions

We have introduced a new way of performing CaBER experiments named tilted CaBER method. This method comprises a horizontal stretching of fluid filaments and allows for a determination of the axial force in the liquid bridge from the gravity-driven bending of the filament applying chain bending theory. This method provides reliable values for the axial force in a liquid filament in a range of $N = 1,000 - 0.1$ μN and allows for a determination of the true elongational viscosity without additional assumptions or specific constitutive equations. For Newtonian fluids, the existence of a negative axial normal stress was proved experimentally, and the solution of Papageorgiou [Papageorgiou 1995] was confirmed for the linear thinning of Newtonian liquids by using two different sets of samples covering a viscosity range of $\eta_0 = 0.9 - 60$ Pas. The tilted CaBER method has been applied to non-Newtonian PEO solutions with concentrations $c \approx c^*$ and $c > c_e$. The assumption of vanishing axial normal stress for evaluating CaBER experiments was confirmed for solutions with $c < c_e$, and a positive axial normal stress was detected for concentrations above the entanglement concentration. In this case, the time evolution of the filament diameter no longer follows a simple exponential decay law. The elongational viscosity calculated from the measured force exhibits the well-known elongational hardening behavior also observed for other polymer solutions [Sridhar et al. 1991; Solomon and Muller 1996].

3.6 Acknowledgements

3.7 Appendix

Equation 3.7 for the calculation of the elongational viscosity in axial direction is only valid for slender filaments as investigated in this paper. Filament curvature must be taken into account in case of strongly noncylindrical filaments which are typical for, e.g., yield stress fluids. At the position of the neck, the equilibrium condition in radial direction then reads as follows:

$$\sigma_{rr} = -\Gamma \left(\frac{2}{D_{mid}} - \frac{1}{|R_c|} \right) \tag{3.27}$$

where D_{mid} is the diameter and Rc is the radius of curvature in axial direction at the neck. The expression for σ_{zz} does not change, and accordingly, the true elongational viscosity is given by

$$\eta_e = \frac{\sigma_{zz} - \sigma_{rr}}{\dot{\varepsilon}} = \frac{1}{\mathrm{d}D/\mathrm{d}t} \left(\Gamma - \frac{2F}{\pi\, D_{mid}} + \frac{\Gamma\, D_{mid}}{2\,|R_c|} \right) \ . \tag{3.28}$$

4 Experimental study on the capillary thinning of entangled polymer solutions

4.1 Abstract

The transient elongation behavior of entangled polymer and wormlike micelles (WLM) solutions has been investigated using capillary breakup extensional rheometry (CaBER). The transient force ratio $X = 0.713$ reveals the existence of an intermediate Newtonian thinning region for polystyrene and WLM solutions prior to the viscoelastic thinning. The exponential decay of $X(t)$ in the first period of thinning defines an elongational relaxation time λ_X which is equal to elongational relaxation time λ_e obtained from exponential diameter decay $D(t)$ indicating that the initial stress decay is controlled by the same molecular relaxation process as the strain hardening observed in the terminal regime of filament thinning. Deviations in true and apparent elongational viscosity are discussed in terms of $X(t)$. A minimum Trouton ratio is observed which decreases exponentially with increasing polymer concentration leveling off at $\mathrm{Tr}_{min} = 3$ for the solutions exhibiting intermediate Newtonian thinning and $\mathrm{Tr}_{min} \approx 10$ otherwise. The relaxation time ratio λ_e/λ_s, where λ_s is the terminal shear relaxation time, decreases exponentially with increasing polymer concentration and the data for all investigated solutions collapse onto a master curve irrespective of polymer molecular weight or solvent viscosity when plotted versus the reduces concentration $c[\eta]$, with $[\eta]$ be-

ing the intrinsic viscosity. This confirms the strong effect of the non-linear deformation in CaBER experiments on entangled polymer solutions as suggested earlier. On the other hand $\lambda_e \approx \lambda_s$ is found for all WLM solutions clearly indicating that these non-linear deformations do not affect the capillary thinning process of these living polymer systems.

4.2 Introduction

Capillary breakup extensional rheometry (CaBER) is a common technique for the determination of the elongational behavior of low-viscosity fluids. This simple and versatile method has been suggested more than 20 years ago [Bazilevsky et al. 1990; Entov and Hinch 1997; Bazilevsky et al. 2001] and is commercially available (Haake CaBER 1, Thermo Scientifics). In contrast to other techniques, CaBER allows for large Hencky strains up to $\varepsilon_{max} = 8...13$ which are of great significance to industrial practice. The CaBER experiment is based on the creation of an instable liquid bridge. After applying a step strain within a short strike time in a range of typically $t_s \approx 20...100$ ms , the diameter of the liquid filament decreases due to the acting surface tension. Monitoring of the filament diameter as a function of time allows for the determination of characteristic elongational flow properties such as the apparent elongational viscosity [Anna and McKinley 2001], the elongational relaxation time [Entov and Hinch 1997; Clasen 2010] or the elongational yield stress [Niedzwiedz et al. 2009, 2010; Martinie et al. 2013].

In a commercial CaBER setup, the only measured quantity during filament thinning is thediameter decay $D(t)$ at a single position in the filament. Different extensions of theexperimental setup are reported in the literature such as optical shape recognition using a(high speed) camera [Christanti and Walker 2001b; Niedzwiedz et al. 2009; Nelson et al. 2011; Gier and Wagner 2012; Sattler et al. 2012], force measurement during initial step strain [Klein et al. 2009] as well as during the whole capillary thinning process [Sachsenheimer et al. 2012]. Unfortunately, controlling the temperature of the thinning liquid thread is not possible due to the lack of an appropriate temperature control unit for CaBER and, therefore, capillary thinning is only performed at room temperature. In a study on polyacrylonitrile solutions samples have been preheated and an elevated constant temperature was assumed due to the short time of experimentation although these measurements were done at room temperature [Tan et al. 2012]. In contrast extensional rheometry of polymer melts has been performed at elevated temperatures. The "universal extensional rheometer" of Munstedt [Münstedt 1975, 1979; Münstedt et al. 1998] stretches polymer melt filaments in a tempered silicon oil bath in order to maintain an accurate temperature control spatially as well as temporally. Furthermore, a filament stretching extensional rheometer (FiSER) has been equipped with

an oven [Bach et al. 2003] in order to determine the elongational properties of polymer melts up to a temperatures $T = 200$ °C. The length of the filament is continuously increased, therefore FiSER experiments require very large devices and an accurate temperature control is complicated due to convection in the oven. To reduce a vertical temperature gradient Bach et al. [Bach et al. 2003] used six temperature transducers combined with eight heat elements as well as a nitrogen flow through the oven smearing out temperature gradients. To the best of our knowledge, no capillary thinning experiments under controlled temperature conditions other than room temperature have been reported so far.

The thinning behavior of a liquid thread is controlled by the capillary force and viscous or visco-elastic forces. The interplay of these forces results in characteristic diameter vs. time curves observed experimentally and predicted theoretically for different types of fluids, e.g. Bingham plastic, power law, Newtonian or visco-elastic fluids. However, the classical way of calculating the elongational viscosity from CaBER experiments is based on the assumption of vanishing axial normal stress (axial force is only caused by the surface tension). Recently, we introduced the so called tilted CaBER method [Sachsenheimer et al. 2012] to determine the true axial force during the capillary thinning process. In this type of experiment, the filament is stretched horizontally and the axial force can be determined from gravity driven bending of the filament in a range of $F = 1,000 - 0.1$ μN.

Using the CaBER technique, we want to improve our knowledge of the self controlled thinning behavior of concentrated and mostly entangled polymer solutions. Therefore, we give first a brief introduction into the theory of filament thinning and CaBER experiments of non-Newtonian fluids focusing on the elongational relaxation time and the true elongational viscosity. Then, we present the experimental setup and give a short overview of the samples used including preparation and characterization. Following with the experimental part, we analyze the effect of different geometrical setups. The transient force ratio including its effect on the elongational viscosity is discussed. After this, we discuss the elongational relaxation time and the relaxation time ratio including a universal scaling for polymer solutions. Finally, we compare CaBER results for some surfactant solutions with filament stretching (FiSER) experiments and give a short conclusion.

4.3 Filament thinning and CaBER experiment

4.3.1 Diameter vs. time evolution during capillary thinning Newtonian

Newtonian fluids form nearly cylindrical filaments. The midpoint diameter D_{mid} of such a thread decreases linearly with time t in a CaBER experiment according to [Papageorgiou 1995; McKinley and Tripathi 2000]:

$$D_{mid}(t) = D_1 - \Theta \frac{\Gamma}{\eta_0} t \tag{4.1}$$

where D_1 is the initial diameter of the linear filament thinning region (this corresponds to time $t = 0$ in the model equation), Γ is the surface tension, η_0 is the shear rate independent shear viscosity of the Newtonian liquid and Θ is a constant numerical factor. Neglecting inertia Papageorgiou [Papageorgiou 1995] predicted $\Theta = 0.1418$ which was confirmed experimentally [McKinley and Tripathi 2000; Sachsenheimer et al. 2012] for the capillary thinning of a Newtonian fluid.

Weakly visco-elastic fluids like dilute and semi-dilute solutions of linear, flexible polymers form perfect cylindrical filaments and their diameter decreases exponentially with time in CaBER experiments [Bazilevsky et al. 1990; Renardy 1994, 1995; Brenner et al. 1996; Bazilevskii et al. 1997; Eggers 1997; Liang and Mackley 1994; Entov and Hinch 1997; Kolte and Szabo 1999; Anna and McKinley 2001; Rodd et al. 2005; McKinley 2005; Ma et al. 2008; Tuladhar and Mackley 2008; Miller et al. 2009; Clasen 2010; Arnolds et al. 2010; Vadillo et al. 2010; Campo-Deaño and Clasen 2010; Sachsenheimer et al. 2012; Vadillo et al. 2012]. Assuming, that the force in the filament is only caused by the surface tension, i.e. no axial normal stresses are considered ($\sigma_{zz} = 0$), the diameter vs. time curve is given by

$$D(t) = D_1 \left(\frac{G\,D_1}{2\,\Gamma} \right)^{1/3} \exp \left(-\frac{t}{3\,\lambda_s} \right) \tag{4.2}$$

where D_1 is the filament diameter at the time when the exponential filament thinning sets in (this corresponds to time $t = 0$ in the model equation), G is the elastic modulus and λ_e is the so called elongational relaxation time which depends on polymer concentration. The prefactor in equation 4.2 can differ, if the $\sigma_{zz} = 0$ assumption is not fulfilled [Clasen et al. 2006a]. Evaluating the elongational relaxation time λ_e seems to be easy but technically it is not always unambiguous. Generally, the exponential decay in the diameter vs. time curves occurs at an intermediate stage of filament thinning. Purely viscous stresses dominate initially, while finite extensibility leads to an accelerated filament decay prior the filament

breakup [Entov and Hinch 1997]. For entangled polymer solutions, the exponential thinning region is barely observable [Clasen 2010] or even completely absent [Arnolds et al. 2010; Sachsenheimer et al. 2012] even if the filament shape still remains cylindrical.

The elongational relaxation time λ_e has been compared to a mean shear relaxation time defined as [Liang and Mackley 1994]

$$\overline{\lambda}_s = \frac{\sum 3\, g_i\, \lambda_i}{\sum g_i} \tag{4.3}$$

calculated from the relaxation time spectrum which can be obtained from small oscillatory shear (SAOS) experiments without assuming a specific constitutive equation. However, the comparison with λ_e was not satisfactory: for a series of polyisobutylene (PIB) solutions they found $\lambda_e \approx 3\overline{\lambda}_s$ but for the fluid S1 $\lambda_e \approx 15\overline{\lambda}_s$.

From a theoretical point of view, Entov and Hinch [Entov and Hinch 1997] analyzed the effect of a relaxation time spectrum on the capillary thinning of viscoelastic filaments using a multi-mode FENE model. For so called middle elastic times resulting in a diameter decay given according to

$$D(t) = D_1 \left[\frac{D_1}{2\Gamma} \sum_{i=1}^{N} g_i \exp\left(-\frac{t}{\lambda_i} \right) \right]^{1/3} \tag{4.4}$$

where g_i and λ_i are the strength and time parameter of the i-th component of the relaxation time spectrum and N the number of elements. However, it is obvious that a simple exponential filament thinning as observed for e.g. weakly viscoelastic polymer solutions can only be observed if all modes $i > 1$ are relaxed and equation 4.4 reduces to equation 4.2 with $\lambda_e \equiv \lambda_1$ (longest relaxation time of the spectrum). The difference between the diameter calculated from equation 4.4 and equation 4.2 is indeed decreasing with time and less than 5 % for times $t > 2.5\lambda_1$. Therefore, the higher modes should only affect the initial non-exponential thinning process. Using polystyrene based Boger fluids, Anna and McKinley [Anna and McKinley 2001] also showed the equivalence of the Zimm relaxation time λ_Z as e.g. defined in Rubinstein and Colby [Rubinstein and Colby 2009] and the elongational relaxation time determined from the exponential diameter decay. However, more detailed experimental studies have found relaxation time ratios $\lambda_e/\lambda_Z = 0.1...30$ for polyethylenoxied (PEO) and polystyrene (PS) solutions with concentrations $c \leq c^*$, where c^* is the critical overlap concentration [Christanti and Walker 2001a, 2002a; Tirtaatmadja et al. 2006; Clasen et al. 2006a,b; Campo-Deaño and Clasen 2010; Vadillo et al. 2012; Haward et al. 2012b]. For concentrations $c \geq c^*$, relaxation time rations $\lambda_e/\lambda_Z = 1...100$ have been reported [Rodd et al. 2005; Clasen 2010; Haward et al. 2012b] for different polymer solutions.

Finally, λ_e has been related to the terminal shear relaxation time λ_s estimated from small amplitude oscillatory shear (SAOS) in the terminal flow region ($\omega \to 0$) according to

$$\lambda_s = \lim_{\omega \to 0} \frac{G'}{\omega \, G''} \tag{4.5}$$

$\lambda_e/\lambda_s \leq 1$ values have been documented for PEO and PS solutions with concentrations $c^* < c < c_e$ [Oliveira et al. 2006; Arnolds et al. 2010; Clasen 2010] where c_e is the entanglement concentration. Arnolds et al. [Arnolds et al. 2010] have quantified the effect of non-linear deformation in CaBER experiments using a single factorizable integral model including a damping function which has been determined from steady shear data. The decrease of the λ_e/λ_s ratio with increasing polymer concentration could be predicted quantitatively.

In short, the elongational relaxation time has been compared to different molecular and shear relaxation times but no simple and universal correlation between these values could be found. However, different shear relaxation times differ from each other. Using the well-known expressions for G' and G'' of the multi-mode Maxwell model with discreet relaxation time spectrum (g_i, λ_i), the terminal shear relaxation time defined by equation 4.5 reads

$$\lambda_{s,Max} = \frac{\sum g_i \, \lambda_i^2}{\sum g_i \, \lambda_i} = \frac{\sum g_i \, \lambda_i^2}{\eta_0} \tag{4.6}$$

where $\eta_0 = \sum g_i \, \lambda_i$ is the zero shear viscosity. Accordingly, λ_s can be interpreted as the centroid of the relaxation time distribution [Böhme 2000]. Obviously, $\lambda_{s,Max}$ (given by equation 4.6) differs from the mean relaxation time $\overline{\lambda}_s$ suggested by Liang and Mackley [Liang and Mackley 1994] and also from the longest relaxation time λ_1 of the spectrum. Using the complex moduli G' and G'' of the Rouse and Zimm model [Rubinstein and Colby 2009], the characteristic model time constants can be related to the terminal shear relaxation time (equation 4.5) according to $\lambda_R = 2\lambda_s$ and $\lambda_Z = [1 - 1/(3\nu)]^{-1} \lambda_s$, respectively. Here ν is the scaling exponent associated with solvent quality.

4.3.2 Determination of the elongational viscosity from capillary thinning experiments

The uniaxial elongational viscosity η_e is generally defined as [Schümmer and Tebel 1983]:

$$\eta_e = \frac{\sigma_{zz} - \sigma_{rr}}{\dot{\varepsilon}} \tag{4.7}$$

where σ_{zz} is the axial normal stress in the fluid filament, σ_{rr} is the radial normal stress and $\dot{\varepsilon}$ is the elongational rate.

Taking into account mass conversation as well as axial and radial force balances on a cylindrical filament undergoing elongation but neglecting gravity and inertia effects, equation 4.7 yields [Sachsenheimer et al. 2012]

$$\eta_e = \frac{\Gamma}{\mathrm{d}D/\mathrm{d}t} - \frac{2F}{\pi\,D\,\mathrm{d}D/\mathrm{d}t}\ , \tag{4.8}$$

where Γ is the surface tension, F the axial force in the filament with diameter D. Unfortunately, F is not measured in standard CaBER experiments. Instead $\sigma_{zz} = 0$ is assumed and the axial force is calculated from the surface tension alone ($F = \rho\,D\,\Gamma$). This results in a simplified expression for the elongational viscosity, the so called apparent elongational viscosity [Anna and McKinley 2001]

$$\eta_{e,app} = -\frac{\Gamma}{\mathrm{d}D/\mathrm{d}t} \tag{4.9}$$

which is widely used in literature [Rothstein 2003; Yesilata et al. 2006; Oliveira et al. 2006; Bhardwaj et al. 2007a,c; Sattler et al. 2007; Chellamuthu and Rothstein 2008; Kheirandish et al. 2008; Tuladhar and Mackley 2008; Chen et al. 2008; Yang and Xu 2008; Kheirandish et al. 2009; Arratia et al. 2009; Miller et al. 2009; David et al. 2009; Regev et al. 2010; Bischoff White et al. 2010; Clasen 2010; Becerra and Carvalho 2011; Erni et al. 2011; Rathfon et al. 2011; Nelson et al. 2011; Haward et al. 2012b; Haward and McKinley 2012; Gier and Wagner 2012; Tembely et al. 2012; Vadillo et al. 2012; Sankaran and Rothstein 2012].

Deviations from the $\sigma_{zz} = 0$ assumption obviously occur for Newtonian liquids [Liang and Mackley 1994; Kolte and Szabo 1999; McKinley and Tripathi 2000; Sachsenheimer et al. 2012] and polymer solutions [Clasen et al. 2006a; Sachsenheimer et al. 2012] and this may quantified using the dimensionless force ratio [McKinley and Tripathi 2000; Sachsenheimer et al. 2012]

$$X = \frac{F}{\pi\,D\,\Gamma} \tag{4.10}$$

where $\pi D\Gamma$ is the force due to the surface tension of the liquid and the $\sigma_{zz} = 0$ assumption is fulfilled as long as the force ratio is $X = 1$. However, the tilted CaBER method can be used measuring the true elongational viscosity η_e from CaBER experiments using equation 4.8 without any assumptions.

4.4 Measurement techniques

4.4.1 Capillary thinning (CaBER) measurements

We have used the commercially available Haake CaBER 1 (Thermo Scientifics, Karlsruhe, Germany) for our elongational measurements. The fluid under test is placed between two

plates of diameter $D_0 = 6$ mm. At time $t = t_0$, a liquid bridge is created by separating the upper plate from a initial displacement h_i to a final displacement h_f within a constant strike time of $t_s = 40$ ms using a linear stretching profile (constant velocity). Plate separation parameters have been varied between 0.51 mm $< h_i < 3$ mm and 7.4 mm $< h_f < 12$ mm. At time $t_1 = t_0 + t_s$, the liquid thread with an initial diameter of $D_1 = D(t_1)$ begins to thin due to the acting surface tension until the filament breaks. Filament shapes were captured using an optical setup including a high speed camera and telecentric illumination [Niedzwiedz et al. 2009; Sachsenheimer et al. 2012]. In order to determine the axial force in the filament, the whole CaBER setup has been rotated by 90°. Horizontal filament stretching experiments have always been performed with $h_i = 0.75$ mm and $h_f \approx 11.5$ mm. The axial force F was calculated from the bending line w of the liquid filament [Sachsenheimer et al. 2012] according to

$$F = \frac{\pi \rho g}{4w} \int\limits_0^x \int\limits_0^{\tilde{x}} D\left(\hat{x}\right)^2 \, \mathrm{d}\hat{x} \, \mathrm{d}\tilde{x} \, , \tag{4.11}$$

where ρ is the density and g the gravitational constant.

For analyzing wormlike micelles solutions, the experimental setup with a resolution of 16 μm has been changed using a mirrorless interchangeable-lens camera (Nikon 1 V2) with a 14 megapixel image sensor yielding a resolution of 2.5 μm. Gentle stretching conditions with $h_i = 1$ mm and $h_f = 8$ mm have to be selected in order to create a filament. A higher initial stretching would not yield a homogenous liquid thread.

4.4.2 Temperature control unit

In order to investigate polymer solutions at different temperatures a special temperature control unit has been constructed. It consists of a temperate camber mounted on the CaBER device as shown in figure 4.1 and a temperature sensor installed in the CaBER bottom plate next to the sample. Special glass windows allow for capturing the filament shape using our optical setup as described above and recording the diameter as a function of time using the laser micrometer of the device. The cell can also act as solvent trap. Therefore, solvent is filled into the cell creating a saturated atmosphere to prevent evaporation of solvent from the fluid filament even at elevated temperatures or long filament lifetimes. In contrast to the oven of Bach et al. [Bach et al. 2003] where several electric heating elements have been used, our temperature control unit is connected to a water bath thermostat. This allows for a very precise temperature adjustment between 5 °C and 90 °C with an accuracy of 0.2 °C.
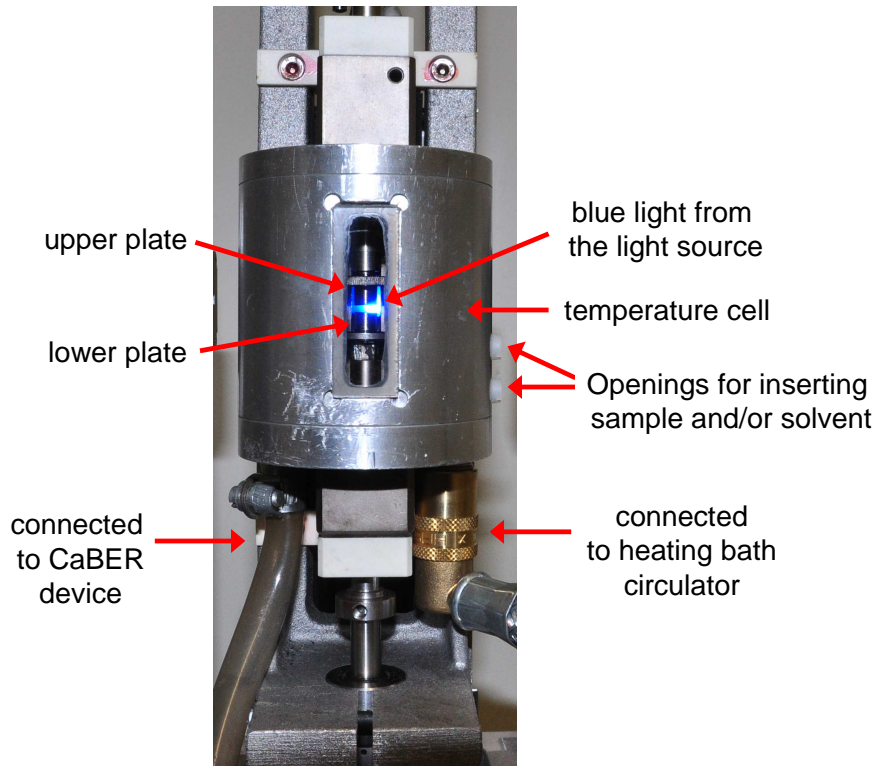
Figure 4.1: Picture of the temperature cell mounted on a CaBER device

4.4.3 Supplementary measurements

Zero shear viscosity η_0 and longest relaxation time (according to equation 4.5) were determined from small amplitude oscillatory shear (SAOS) experiments using a Physica MCR501 (Anton Paar, Graz, Austria) equipped with a cone-plate geometry (50 mm diameter and 1° cone angle). Surface tension Γ has been determined at $T = 20\ °\text{C}$ using a DCAT1 tensiometer (DataPhysics, Filderstadt, Germany) equipped with a platinum-iridium Wilhelmy-plate within an experimental error of $\Delta\Gamma = \pm 1$ mN/m. Density measurements have been preformed using a pycnometer with a total volume of $V = 10.706\ \text{cm}^3$ at $T = 20\ °\text{C}$.

4.5 Sample preparation and characterization

Polystyrene (PS), polyethylene oxide (PEO) and cetylpyridinium chlorid/sodium salicylate/sodium chloride (CPyCl/NaSal/NaCl) solutions have been used as model systems to study the elongational behavior of viscoelastic, semi-dilute and concentrated polymer solutions ($c > c^*$). Polystyrene (Polymer Standards Service, Mainz, Germany) with a weight average molecular weight of $M_w = 3 \cdot 10^6$ g/mol and a polydispersity index of $PDI = 1.17$ has been dissolved in diethyl phthalate (Merck, Darmstadt, Germany) with a zero shear

viscosity of $\eta_0 = 12.6 \pm 0.3$ mPas. Polyethylene oxide (Sigma-Aldrich, Missouri, USA) with weight average molecular weight of $M_w = 1 \cdot 10^6$ g/mol, $M_w = 2 \cdot 10^6$ g/mol, and $M_w = 4$ $\cdot 10^6$ g/mol has been dissolved in distilled water. Additionally, aqueous solutions of a low molecular weight PEO ($M_w = 3.5 \cdot 10^4$ g/mol , in the following labeled as PEG) with concentrations $c = 8$ % ($\eta_0 = 17.3 \pm 0.1$ mPas) and $c = 16.7$ % ($\eta_0 = 97.0 \pm 0.5$ mPas) have been used as solvent for the PEO sample with $M_w = 1 \cdot 10^6$ g/mol. Aqueous PEO solutions are in the Θ-state at room temperature. Therefore, adding PEG will not change the solvent quality. All polymer solutions were prepared by adding the polymer powder to the solvent. Samples were homogenized by means of shaking at room temperature until the solutions becomes totally clear. Long shaking times of approximately one moth were needed for the highly concentrated PS solutions. The surfactant solution CPyCl/NaSal/NaCl is common model systems for linear wormlike micelles (WLM) in the entangled state and corresponding linear viscoelastic data are e.g. given in Berret et al. [Berret et al. 1993]. In addition to the reptation time scale λ_{rep} of covalently bounded polymers, WLM break and reform with a characteristic time λ_{br} . For $\lambda_{br} << \lambda_{rep}$, the rheological behavior is described by a single Maxwell model with relaxation time $\lambda_s = \sqrt{\lambda_{br} \lambda_{rep}}$ [Rehage and Hoffmann 1988; Cates 1987, 1988]. The CPyCl/NaSal/NaCl solutions have been prepared following Berret et al. [Berret et al. 1993] at molar surfactant concentrations between 40 mM and 120 mM and constant salt surfactant ratio of $R = 0.5$. A 0.5 M NaCl solution has been used as solvent to ensure a constant electrostatic screening length while varying the CPyCl and NaSal concentration. NaSal is strongly binding to the surfactant und both, CPyCl and NaSal, are responsible for creation of the wormlike structures. Therefore, we have calculated the living polymer concentration c as the sum of the mass concentrations of CPyCl and NaSal.

Viscoelastic behavior can be observed in a CaBER experiment if the timescale of the elastically controlled thinning (assumed to be the terminal shear relaxation time λ_s) exceeds the viscous timescale (assumed to be $t_v = \eta_0 D/2\Gamma$) quantified using the dimensionless elasto-capillary number [Anna and McKinley 2001; Clasen 2010]

$$\mathrm{Ec} = \frac{2\lambda_s \Gamma}{\eta_0 D} \ . \tag{4.12}$$

Since the diameter D is a function of time and, hence, the elasto-capillary number is a function of time, too. Figure 4.2 shows the minimum elasto-capillary number Ec_0 calculated using the initial diameter of $D_0 = 6$ mm for PS, aqueous PEO and CPyCl/NaSal/NaCl solutions investigated in this study. The elasto-capillary number Ec decreases with increasing polymer concentration in good agreement with literature [Clasen 2010; Sachsenheimer et al. 2012] since the zero shear viscosity varies stronger with polymer concentration than the shear relaxation time. For low polymer concentrations, Ec is nearly constant. The critical

concentration where Ec begins to decrease is equal to the entanglement concentration c_e determined from shear viscosity data. These values are summarized in table 4.1.

Table 4.1: Entanglement concentrations c_e and intrinsic viscosities $[\eta]$

material	c_e / %	$[\eta]$ / cm^3g^{-1}
PS	2.5	295
PEO 1Mio	1.7	598
PEO 2Mio	1.3	1027
PEO 4Mio	0.66	1764

CPyCl/NaSal/NaCl solutions investigated here do not show a constant Ec value for low concentrations indicating that all surfactant solutions are in the entangled state. However, $Ec_0 < 1$ values may indicate that the beginning of the thinning process is controlled by viscous forces instead of viscoelastic as suggested by Clasen [Clasen 2010] for PS solutions.
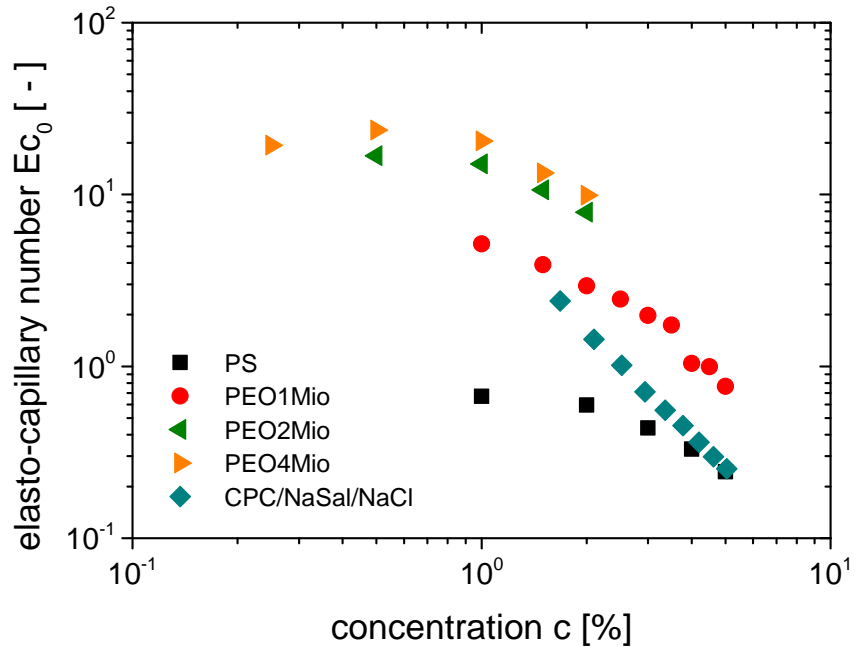

Figure 4.2: Initial elasto-capillary number as a function of polymer concentration for PS solutions (squares), aqueous PEO solutions with $M_w = 1 \cdot 10^6$ g/mol (circles), aqueous PEO solutions with $M_w = 2 \cdot 10^6$ g/mol (diamonds), aqueous PEO solutions with $M_w = 4 \cdot 10^6$ g/mol (triangles), and CPyCl/NaSal/NaCl (hexagons).

4.6 Results and discussion

4.6.1 Effect of stretching ratio on the diameter vs. time curve

Low initial heights h_i and high final heights h_f are needed for horizontally filament stretching experiments in order to create a measurable deflection of the liquid thread and prevent liquid dropping out of the initial gap of the plates. Dramatically changing of the stretching parameter might influence the thinning behavior of a liquid thread. In addition to Miller et al. [Miller et al. 2009] and Kim et al. [Kim et al. 2010], we studied these effects using PEG/PEO solutions. Figure 4.3 shows exemplarily the diameter vs. time curve for 1 % PEO
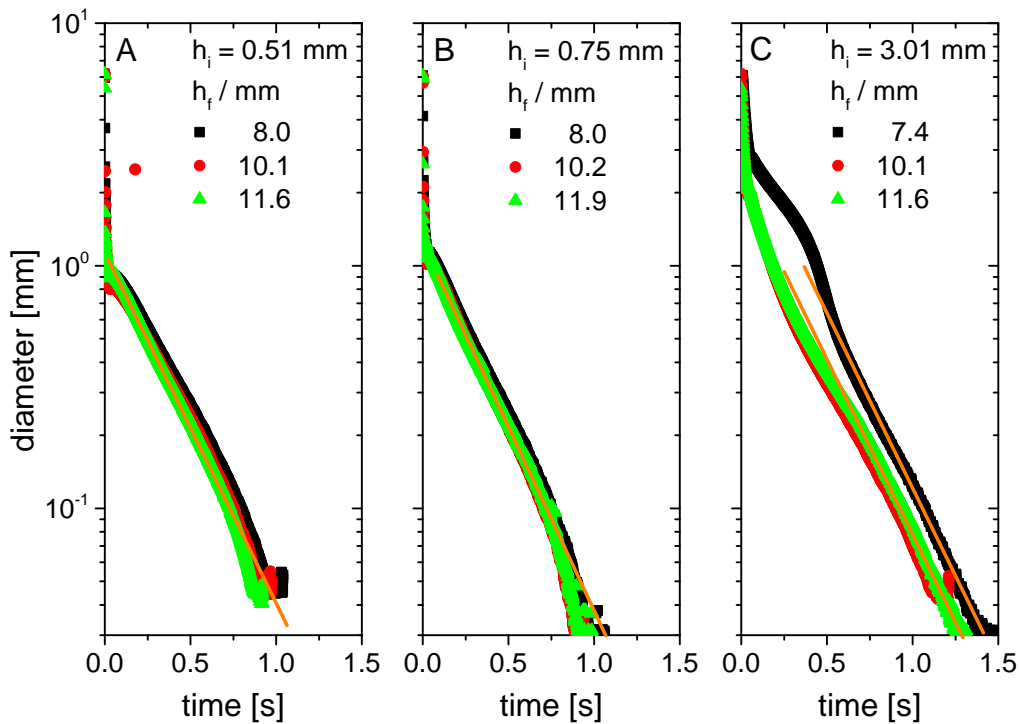
Figure 4.3: Filament diameter as a function of time for a 1 % PEO of $M_w = 1 \cdot 10^6$ g/mol dissolved in a 16.7 % PEG solution with given initial and final leights.

of $M_w = 1 \cdot 10^6$ g/mol dissolved in a 16.7 % PEG solution using different initial ($h_i = 0.51$ mm, $h_i = 0.75$ mm, and $h_i = 3.01$ mm) and final heights ($h_f \approx 8$ mm, $h_f \approx 10$ mm, and $h_f \approx 12$ mm). Filament lifetime t_{fil} increases with increasing initial height h_i but significant differences between $h_i = 0.51$ mm and $h_i = 0.75$ mm cannot be observed. Highest filament lifetimes are observed for the lowest stretching ratio ($h_i = 3.01$ mm and $h_f = 7.4$ mm). Differences in t_{fil} might be due to differences in the capillary stress $\sigma_{rr}(t_1) = -2\Gamma/D$ right after the upper plate has reached the end position. Higher filament lifetimes correspond to higher D_1 values (see for example figure 4.3 C) and therefore to lower initial radial stresses.

An exponential decrease of the filament diameter is clearly and easily visible allowing for a determination of the elongational relaxation time λ_e according to equation 4.2. However, for higher polymer concentrations the onset of the exponential decay regime is shifted to lower diameters and λ_e can only be determined in the final stage of thinning close to filament breakup. Finally, at concentrations $c > 4$ % [Arnolds et al. 2010] the exponential diameter decay is no longer observable. In these solutions a high force ratio $X > 1$ is present [Sachsenheimer et al. 2012] during the whole thinning process. But for solutions with increased solvent viscosity (added PEG) λ_e can be determined from exponential filament thinning up to 5 % (8 % PEG).

Nevertheless, all experiments yield an identical value for the elongational relaxation time independent of h_i and h_f in agreement with the literature [Kim et al. 2010; Miller et al. 2009]. The diameter $D_{exp,0}$ where the filament begins to thin exponentially decreases with increasing stretching ratio. Therefore, the elasto-capillary number Ec at which the exponential decrease sets in is not a material parameter as suggested by Clasen [Clasen 2010] but also depends on the choice of h_i and h_f.

4.6.2 Transient force ratio and its relation to the elongational viscosity

Figure 4.4 shows typical results for a 2 % PEG/PEO and a 4 % PS solution for the force ratio X as a function of the normalized time t/t_{fil} where t_{fil} is the filament lifetime. The force ratio decreases exponentially at the early state of the thinning process indicating a characteristic initial relaxation process. The sudden separation of the lower and upper plate provokes a huge and rapid deformation of the liquid thread. The diameter of the filament decreases from the initial diameter $D_0 = 6$ mm to a diameter $D_1 \approx 1$ mm observed right after the upper plate has reached its final position corresponding to an initial Hencky strain of $\varepsilon_0 = 3.6$. For an typical strike time of $t_s = 40$ ms, the initial deformation occurs at an average elongation rate $< \dot{\varepsilon}_0 >= \varepsilon_0/t_s \approx 90$ s^{-1}. This initial step strain results in an (initial) axial normal stress σ_{zz} which relaxes after the step strain. For PEO solutions with low polymer concentrations $c \leq 2.5c_e$, the transient force ratio $X(t)$ levels off to a final value of $X = 1.00 \pm 0.04$ independent of concentration. For higher PEO concentrations, the force ratio X_∞ increases monotonically with polymer concentration and the exponentially decreasing diameter region is not longer observed (Arnolds et al. 2010, Sachsenheimer et al. 2012). A force ratio $X = 1$ corresponds to a vanishing axial normal stress σ_{zz} and, therefore, to an axial force F only given by the surface tension Γ and the diameter D of the liquid thread.
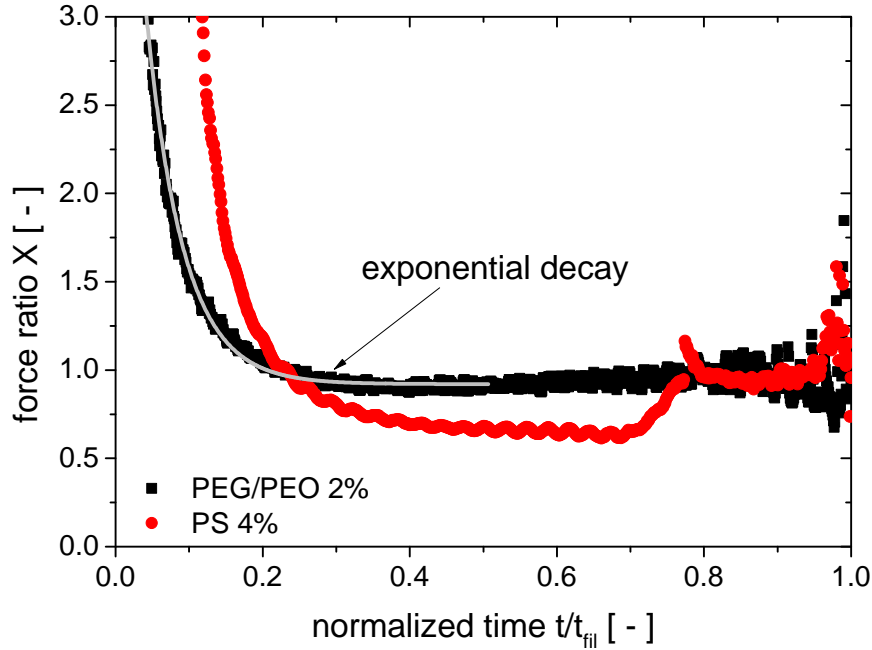
Figure 4.4: Transient force ratio X as a function of normalized time for a 2 % PEO of $M_w = 1 \cdot 10^6$ g/mol dissolved in a 16.7 % PEG solution and a 4 % PS solution. The grey line illustrated the exponential decay in the force ratio fitting equation 4.15 with $\tilde{X} = X_\infty$ to the experimental data.

The PS and CPyCl/NaSal/NaCl solutions show a more complex behavior. After the initial decrease, the transient force ratio levels off to a much lower value of $X_{min} = 0.75 \pm 0.05$ for PS and CPyCl/NaSal/NaCl independent of the concentration (except of the 1 % PS solution for which the force signal is too low and no X_{min} could be detected). These values agree well with the theoretical value of $X_{New} = 0.713$ for a Newtonian liquid [Papageorgiou 1995]. A force ratio $X < 1$ corresponds to a compressive axial normal stress σ_{zz} in the fluid filament [Sachsenheimer et al. 2012]. After passing the X_{min} region, the force ratio starts to increase to a final force ratio of $X_\infty = 0.98 \pm 0.08$ for all PS and CPyCl/NaSal/NaCl solutions investigated here. These force measurements confirm the occurrence of an early viscocapillary controlled regime and a transition to an elasto-capillary controlled regime for PS and CPyCl/NaSal/NaCl solutions as suggested by Entov and Hinch [Entov and Hinch 1997] as well as Clasen [Clasen 2010]. The visco-capillary thinning regime occurs due to the low elasto-capillary numbers of these solutions. However, changing the solvent viscosity of PEO solutions by adding PEG does not cause an early Newtonian thinning regime. The viscosity of 16.7 % PEG solution is about seven times higher than the viscosity of diethyl phthalate but elasto-capillary numbers $\text{Ec}_0 > 1$ are found independent of solvent viscosity η_{sol}.

The elongational viscosity η_e is often calculated as apparent value $\eta_{e,app}$ using the $\sigma_{zz} = 0$ assumption (corresponding to $X = 1$) according to equation 4.9. Generally, the elongation rate $\dot{\varepsilon}$ changes during capillary thinning in CaBER experiments, but it remains constant for a liquid thread with exponentially decreasing diameter. Then, the elongation rate is related to the elongational relaxation time according to $\dot{\varepsilon} = 2/(3\lambda_e)$. The normal stresses σ_{zz} and σ_{rr} (if present) also depend on time. In consequence, the elongational viscosity η_e or $\eta_{e,app}$ are transient values even if the elongation rate $\dot{\varepsilon}$ is constant.

Figure 4.5 shows the true and apparent elongational viscosity as a function of time t for the 3 % PEG/PEO and the 4 % PS solution exemplarily. In the first thinning period, η_e decreases with time according to the decrease of the force ratio $X(t)$ whereas $\eta_{e,app}$ increases monotonically. As the capillary thinning proceeds further, the transient elongational viscosity η_e goes through a distinct minimum with $\eta_{e,min}$, and finally increases exponentially as expected for a Maxwell fluid with a single relaxation time. This strain hardening is a consequence of the well-known entropy elasticity of polymer chains. During this last stage of thinning, $\eta_{e,app}$ and η_e are equal as expected for $X = 1$. Similar results are found for all solutions investigated in this study. For the PS and CPyCl/NaSal/NaCl solutions the intermediate regime is controlled by visco-capillary thinning ($X = 0.713$) as discussed above yielding an apparent elongational viscosity substantially higher than the true value.

The differences between true and apparent elongational viscosity are caused by the axial normal stress σ_{zz} in the filament which can be expressed in terms of the force ratio X and the radial normal stress σ_{rr} according to [Sachsenheimer et al. 2012]

$$\sigma_{zz} = 2\sigma_{rr}\left(1 - X\right) \ . \tag{4.13}$$

The ratio of the true elongational viscosity and the apparent elongational viscosity then reads as follows

$$\frac{\eta_e}{\eta_{e,app}} = \frac{\sigma_{zz} - \sigma_{rr}}{-\sigma_{rr}} = 2X - 1 \ . \tag{4.14}$$

From equation 4.14, it becomes obvious that a force ratio $X < 1$, as observed for a Newtonian controlled thinning, results in an elongational viscosity smaller than the apparent value and $X > 1$, as e.g. observed during the initial period of thinning or for highly concentrated PEO solutions [Sachsenheimer et al. 2012], causes $\eta_e > \eta_{e,app}$. Both elongational viscosities (true and apparent) are only equal if the force ratio is $X = 1$.

In addition, the uniaxial elongational viscosity of polymer solutions can be obtained from filament stretching extensional rheometer (FiSER) measurements. In such an experiment the liquid under test is also placed between to parallel plates, but the upper plate is separated continuously until the filament breaks [Tropea 2007].
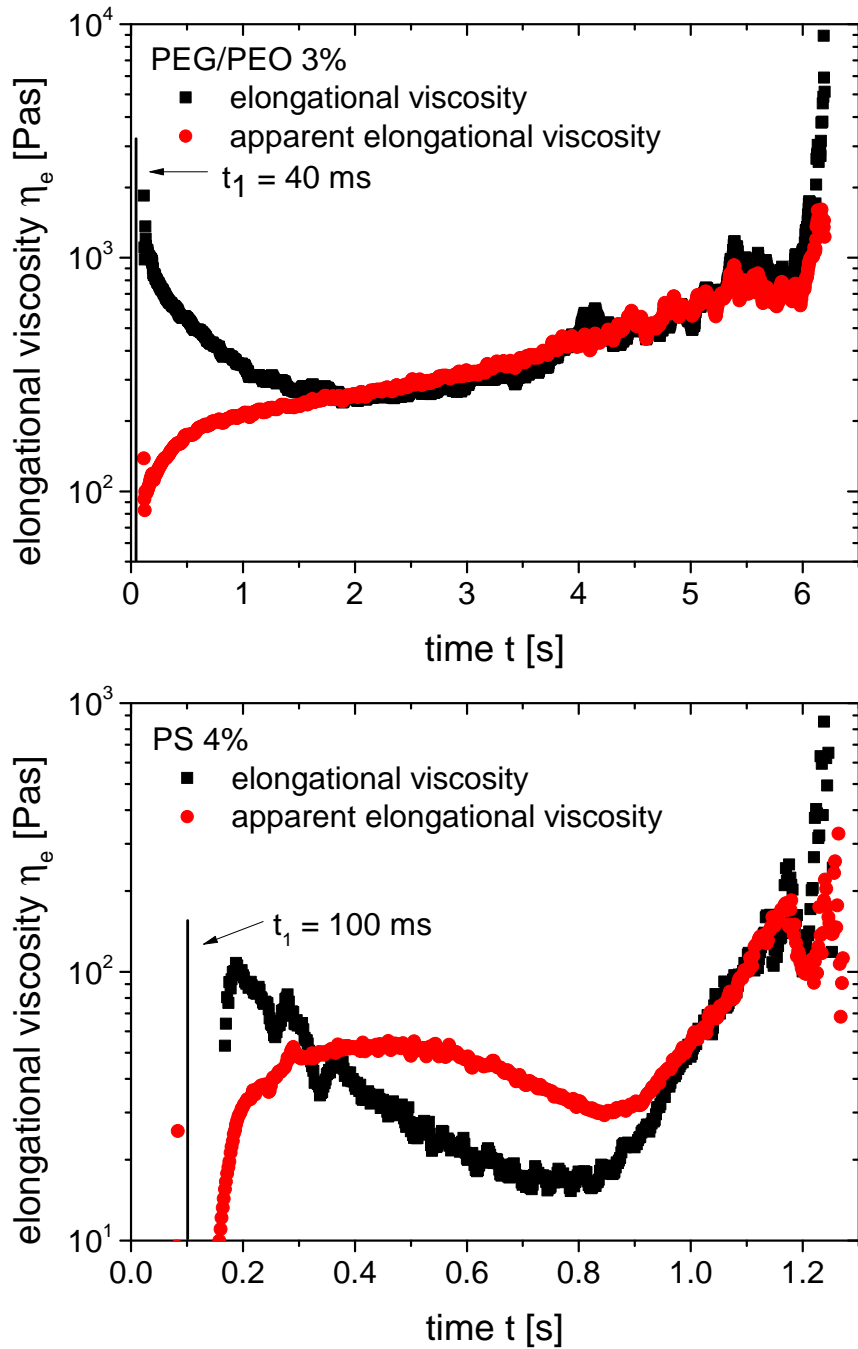
Figure 4.5: Elongational viscosity (squares) and apparent elongational viscosity (circle) as a function of time for a 3 % PEO of $M_w = 1 \cdot 10^6$ g/mol dissolved in a 16.7 % PEG solution (top) and a 4 % PS (bottom) solution.

Generally, two types of velocity profiles are possible [Kolte et al. 1997]: The upper plate is separated with an exponentially increasing velocity or the plate velocity is controlled, such that the filament diameter decreases exponentially corresponding to constant elongational rate during the whole experiment [Kolte et al. 1997; Tropea 2007]. The transient elongational

viscosity is computed from the tensile force exerted by the fluid column on the endplate and the filament diameter at the axial midpoint [McKinley et al. 2001]. More details about FiSER are given in [Tirtaatmadja and Sridhar 1993; Spiegelberg et al. 1996; Anna et al. 1999; Orr and Sridhar 1999; McKinley et al. 2001; McKinley and Sridhar 2002; Anna et al. 2001; Rothstein and McKinley 2002a,b; Rothstein 2003; Tropea 2007].

However, FiSER measurements yield higher values for the maximum elongational viscosity η_e^{max} than CaBER [Bhardwaj et al. 2007a]. Similar results are obtained for CPyCl/NaSal/NaCl solutions investigated in this study (data not shown). The observed differences between both techniques may be explained by the simplified CaBER analysis using the $\sigma_{zz} = 0$ assumption. But as shown above, $X = 1$ was found the final period of thinning for WLM solutions. Therefore, the $\sigma_{zz} = 0$ assumption is fulfilled and cannot be the reason for the differences in $\eta_{e,max}$. It seems to be more likely, that differences in strain history and failure mechanism affect the material behavior in elongational flow. Indeed, FiSER experiments of the 2.94 % CPyCl/NaSal/NaCl solution show a very high maximum force ratio of $X_\infty^{FiSER} = D_{min}\sigma_{max}/4\Gamma \approx 60$ and a diameter $D_{min} \approx 1$ mm at filament rupture clearly indicating the difference in the thinning mechanism.

Figure 4.6 shows the minimum viscosity ratio $Tr_{min} = \eta_{e,min}/\eta_0$ for the investigated polymer
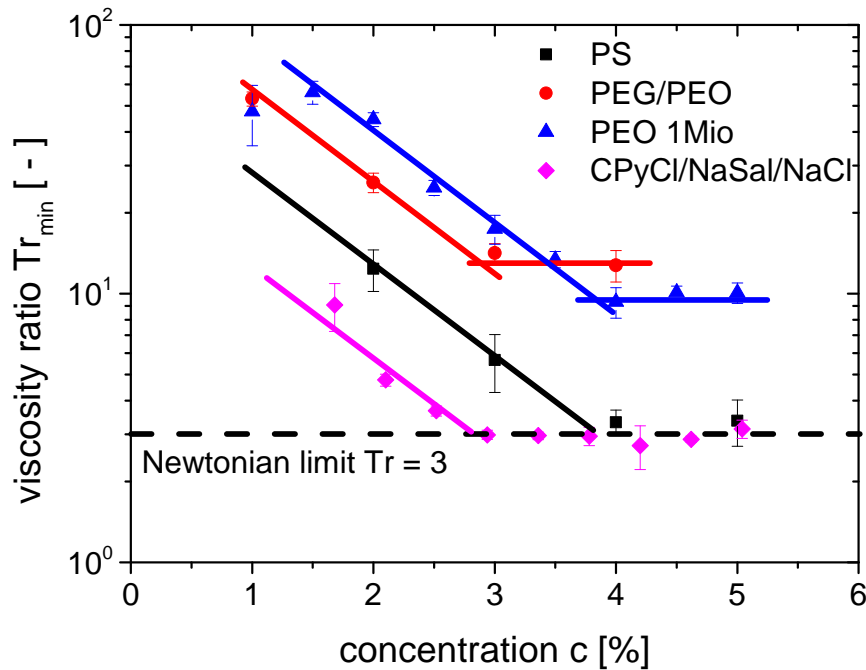
Figure 4.6: Minimum viscosity ratio $Tr_{min} = \eta_{e,min}/\eta_0$ as a function of concentration for PS (squares), PEO of $M_w = 1 \cdot 10^6$ g/mol dissolved in a 16.7 % PEG solution (circles), aqueous PEO of $M_w = 1 \cdot 10^6$ g/mol (triangles) and CPyCl/NaSal/NaCl (diamonds) solutions.

solutions as a function of polymer concentration c. The viscosity ratio Tr_{min} decreases exponentially with increasing polymer concentration c according to $\text{Tr}_{min} \propto \exp\left(-0.74 \pm 0.02 c/\%\right)$ and levels off at a constant value for polymer concentrations $c > c_e$ for all solutions including CPyCl/NaSal/NaCl. For PEO solutions with $M_w = 1 \cdot 10^6$ g/mol Tr_{min} is between 60 and 70 for low concentrations and levels off to $\text{Tr}_{min} = 9.5 \pm 0.8$. Obviously, the initial step strain results in a non-linear change of polymer configuration which does not relax and capillary thinning does not start from the equilibrium where $\text{Tr} = 3$ would be expected. Increasing the solvent viscosity results in a slight increase of Tr_{min} for high PEO concentrations ($\text{Tr}_{min} = 13.4 \pm 0.8$ for PEO with $M_w = 1 \cdot 10^6$ g/mol dissolved in a aqueous solution of 16.7 % PEG) and in a similar shift of the concentration at which the limiting value of Tr_{min} is reached. In contrast, for PS and CPyCl/NaSal/NaCl solutions Tr level off at $\text{Tr}_{min} = 3$ indicating a relaxation of initial stresses and a pure Newtonian response for high polymer concentrations before the beginning of the elastocapillary thinning process. Nevertheless, at low concentrations min $\text{Tr} \gg 3$ is found even though an intermediate Newtonian thinning regime is observed for these solutions.

However, analyzing the minimum Trouton ratio Tr_{min} seems to be useful due to two reasons. The determination of the minimum elongational viscosity $\eta_{e,min}$ is very convenient whereas a determination of the maximum elongational viscosity or maximum Trouton ratio often calculated for surfactant solutions [Bhardwaj et al. 2007a,c] includes large experimental uncertainties. All solutions (including the CPyCl/NaSal/NaCl surfactant solutions) investigated in this study thin to very tiny diameters which are hard to be determined accurately. The minimum elongational viscosity also indicates a transition in the thinning behavior. In the initial stage of the experiment, the thinning behavior is controlled by an initial relaxation of the axial normal stress (decrease of η_e) followed by a pronounced increase of the radial normal stress (increasing of η_e) at the final stage of thinning.

4.6.3 Elongational relaxation time

In addition to the determination of elongational viscosities, CaBER experiments also allow for measuring the elongational relaxation time λ_e. Commonly, λ_e is determined from the exponential diameter decay of the liquid filament undergoing capillary thinning according to equation 4.2. Figure 4.7 shows three independently determined elongational relaxation times for the PEO ($M_w = 1 \cdot 10^6$ g/mol) and PS solutions investigated in this study: the elongational relaxation time λ_e determined from the diameter vs. time curve of a vertically stretched filament, the elongational relaxation time λ_e determined from the diameter vs. time curve of an horizontally stretched filament and the force relaxation time λ_X calculated

from the initial exponential decay of the transient force ratio in the initial thinning period. Although the filament diameter does not decrease exponentially in this regime, the force ratio follows an exponential decrease in time according to

$$X(t) = C \exp\left(-\frac{t}{\lambda_X}\right) + \tilde{X} \ , \tag{4.15}$$

where C is a constant and $\tilde{X}$ is the value of the force ratio after the initial decay ($\tilde{X} \equiv X_\infty \approx 1$ for PEO solutions and $X_{min} \approx 0.75$ for PS and CPyCl/NaSal/NaCl solutions). A representative result a fit of equation 4.15 to experimental data for 2 % PEO dissolved in the 16.7 % PEG solution is shown as gray line in figure 4.4. We also analyzed the influence of the strike time $20\mathrm{ms} < t_s < 480\mathrm{ms}$ on the force relaxation time as shown in the inset of figure 4.7 (top) for the aqueous 4 % PEO ($M_w = 1 \cdot 10^6$ g/mol) solution. In the investigated parameter range λ_X is found to be independent of the strike time. This indicates that the initial relaxation of the force ratio $X(t)$ is not influenced by inertia effects as expected since Reynolds numbers defined as $\mathrm{Re} = \rho v D_0/\eta_0$, where v is the velocity of the upper plate during step strain $v = (h_f - h_i)/t_s$, are less than one. For the 4 % PEO solution (insert in figure 4.7) with a zero shear viscosity of $\eta_0 = 8.6$ Pas, corresponding Reynolds numbers are between 0.016 and 0.38 for strike times varying from 480 ms and 20 ms. However, considering our standard setup with $t_s = 40$ ms, maximum Reynolds numbers of $\mathrm{Re} = 4$ are found for solutions where a force relaxation time could be determined. But even in this cases inertia effects may be neglected since the filaments are stabilized elastically [Sachsenheimer et al. 2012].

Nevertheless, too high strike times should not be chosen because a superposition of stretching and capillary thinning has to be avoided. Therefore, we propose an appropriate strike time of $t_s < 0.1 t_{fil}$.

All three elongational relaxation times agree well within experimental error irrespective of the polymer concentration as long as $X_\infty = 1$. The impressive agreement between λ_e and λ_X suggests that the first stage of capillary thinning, where the diameter does not thin exponentially, is controlled by the same relaxation process as the terminal thinning regime with its exponential filament decay. The excellent agreement between all three relaxation times also shows that gravity has no influence on the elasto-capillary thinning of viscoelastic fluids demonstrating the equivalence of upright and tilted CaBER experiments.

Furthermore, the elongational relaxation times increase monotonically with increasing polymer concentration c. The force relaxation times λ_X of PEO solutions with concentrations c = 4 % (corresponding to $c > 2c_e$) show a stronger increase with concentration c than elongational relaxation times for concentrations $c < 2c_e$. However, a determination of λ_e was not possible for these solutions due to the absence of an exponentially decreasing diameter region

[Arnolds et al. 2010]. These solutions also exhibit a final force ratio $X > 1$ [Sachsenheimer et al. 2012].
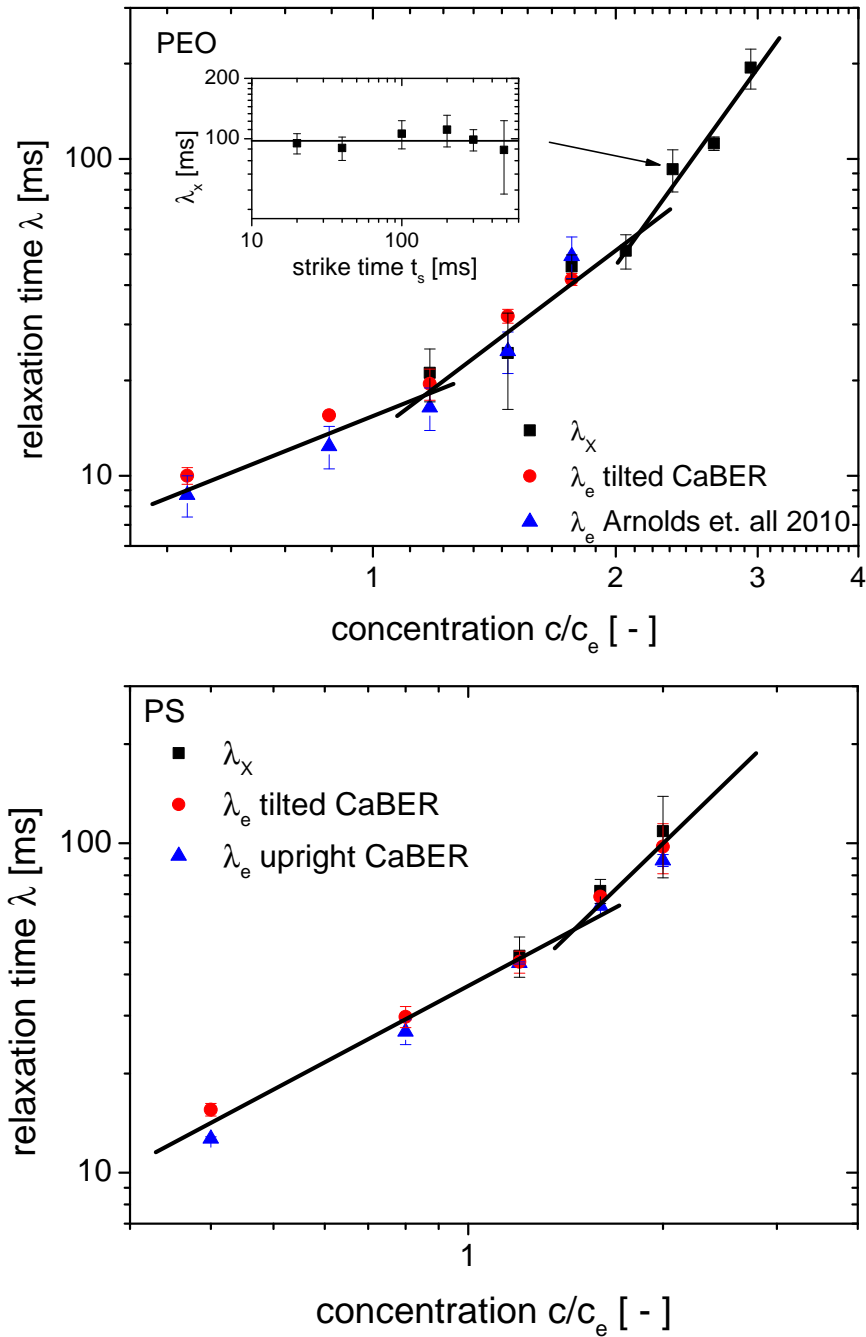
**Figure 4.7:** Elongational relaxation times from CaBER experiments for aqueous PEO of $M_w = 1 \cdot 10^6$ g/mol (top) and PS solutions (bottom). Relaxation time values for PEO solutions in the upright CaBER experiment are taken from Arnolds et al. [Arnolds et al. 2010]. The inserted diagram represents the force ratio relaxation time as a function of the strike time for a 4 % PEO solution. Lines are a guide to the eye.

4.6.4 Correlation between shear and elongational relaxation time

In figure 4.8, the relaxation time ratio λ_e/λ_s, is shown as a function of polymer concentration c. Data for PEO solutions with different molar mass and solvent viscosities as well
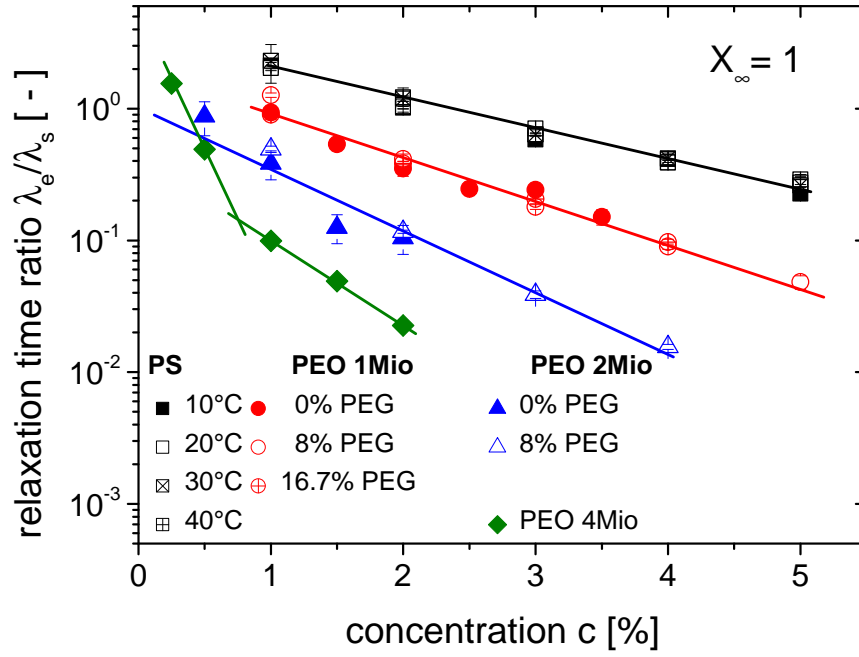
Figure 4.8: Relaxation time ratio as a function of concentration for different polymer solutions with different solvent viscosity and temperature as shown in the legend of the diagram.

as PS solutions at different temperatures are displayed. In all cases, the relaxation time ratio decreases exponentially with increasing polymer concentration c covering up to two orders of magnitude. PEO solutions with higher PEO molar mass show lower λ_e/λ_s values (at constant polymer concentration c) and a stronger dependence on polymer concentration. Investigations on PEO solutions shows that the solvent viscosity does not affect the relaxation time ratio λ_e/λ_s. Varying the temperature of the PS solution between 10°C and 40°C corresponds to a viscosity as well as a shear and elongational relaxation time change but does not affect the relaxation time ratio. Slight changes in surface tension or solvent quality upon temperature variation are not considered to be relevant for the λ_e/λ_s ratio.

Obviously, changing the solvent viscosity or the temperature affects the relaxation of dissolved polymer molecules in the same way for elongational and shear flows. The elongational relaxation time λ_e therefore, is a characteristic parameter of the polymer solution but not equal to the terminal shear relaxation time λ_s. Comparing λ_e to a mean shear relaxation time $\overline{\lambda}_s$ as suggested by Liang and Mackley [Liang and Mackley 1994] according to equation 4.3 requires the knowledge of the relaxation time spectrum which can not be determined

unambiguously. However, the PS solutions investigated here are thermo-rheologically simple so that the viscosity function $\eta(\omega)$ of all investigated PS solutions (independent of concentration or temperature) can be plotted as dimensionless master curve by scaling the viscosity with the zero shear viscosity η_0 and the angular frequency with the terminal shear relaxation time λ_s. Accordingly, all relaxation times scale with λ_s and any average relaxation time like e.g. $\overline{\lambda}_s$ exhibit the same dependence on concentration or temperature. As a consequence, the ratio of λ_e and any average relaxation time should be constant independent of concentration or temperature. The strong decrease of λ_e/λ_s must therefore be related to a non-linear material property as already suggested by Arnolds et al. [Arnolds et al. 2010].

Finally, it is interesting to note that the exponential decrease of λ_e/λ_s with increasing concentration seems to be a universal feature of entangled polymer solutions. Figure 4.9 displays the λ_e/λ_s values as a function of normalized concentration $c[\eta]$, where $[\eta]$ is the intrinsic viscosity of the polymer solution, for solutions of PEO and PS with different molecular weight, solvent viscosity and temperature. Obviously, all data collapse onto a single master curve
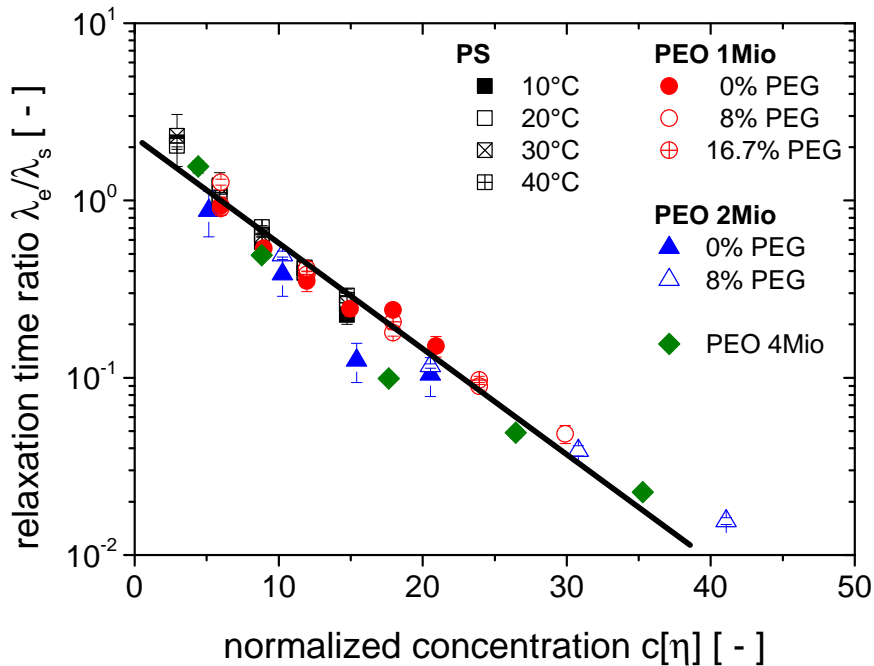
Figure 4.9: Relaxation time ratio as a function of normalized concentration for polymer solutions shown in figure 4.8.

when potted as a function of $c[\eta]$ and follow a unique exponential decay.

For comparison, we have investigated a series of CPyCl/NaSal/NaCl solutions which represent simple Maxwell fluids characterized by one relaxation time [Cates 1996; Berret et al. 1993] as shown in the insert of figure 4.10 where G' and G'' data for two CPyCl/NaSal/NaCl

solutions are shown. Solid lines represent the best fit of the Maxwell model to the exper-
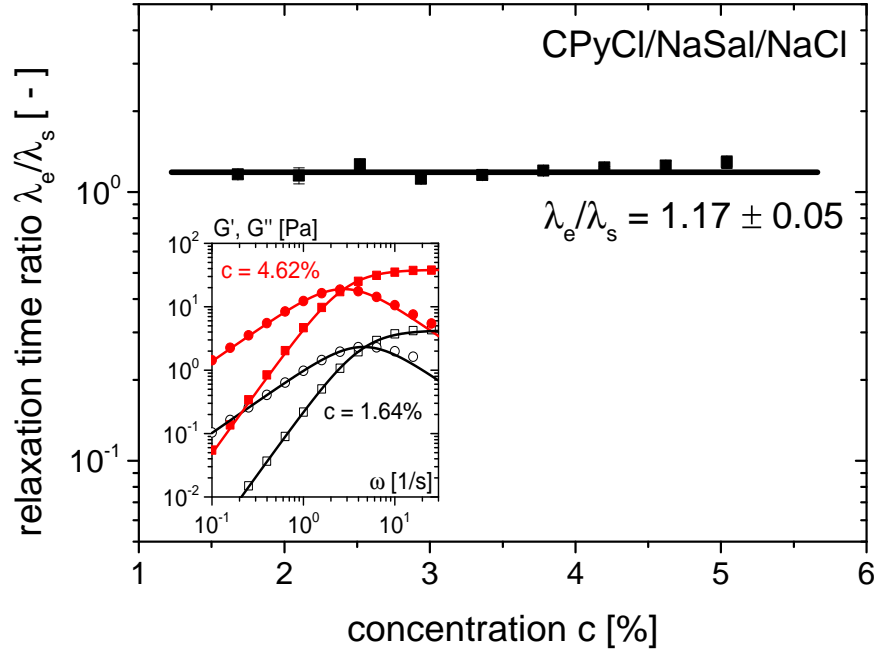
Figure 4.10: Relaxation time ratio as a function of concentration for different CPyCl/NaSal/NaCl solutions. The line represents the relaxation time ratio mean value of $\lambda_e/\lambda_s = 1.17 \pm 0.05$. The insert shows the storage (squares) and loss modulus (circles) as a function of angular frequency for the 4.42 % (filled symbols) and the 1.64 % CPyCl/NaSal/NaCl solution (open symbols). Best fits of experimental data, using a single Maxwell model, are represented in the insert as solid lines.

imental data. The relaxation time ratio for these simple Maxwell fluids is shown in figure 4.10. Surprisingly, all solutions show a constant value of $\lambda_e/\lambda_s = 1.17 \pm 0.05$ independent of concentration indicating that the elongational behavior of WLM solutions is only given by linear fluid properties determined in small amplitude oscillatory shear. This result is remarkable because the relaxation time of a wormlike structure strongly depends on the mean length of the micelles. Finding $\lambda_e \approx \lambda_s$ suggests, that the mean length does not change during the elongational deformation as discusses theoretically [Vasquez et al. 2007; Cromer et al. 2009; Germann et al. 2013]. A change in micellar length due to a deformation induced increase of the breakage rate would dramatically shorten the relaxation time and $\lambda_e/\lambda_s << 1$ would be expected.

On the other hand, $\lambda_e \approx \lambda_s$ implies that non-linear effects are not relevant in CaBER experiments of these surfactant solutions. Identifying the shear relaxation time λ_s as characteristic relaxation time of the material and considering $\dot{\varepsilon} = 2/(3\lambda_e)$, the relaxation time ratio λ_e/λ_s might be interpreted as an inverse Weissenberg number $\mathrm{Wi}^{-1} = (\dot{\varepsilon}\lambda_s)^{-1} = 3\lambda_e/(2\lambda_s)$. For

CPyCl/NaSal/NaCl solutions, Wi = 0.6 is independent of surfactant concentration indicating a linear viscoelastic response. Unfortunately, the model of Arnolds et al. [Arnolds et al. 2010] taking into account the strong deformation during capillary thinning cannot be applied here. The damping function cannot be determined from independent steady shear experiments since shear banding is prominent in these flows [Bhardwaj et al. 2007a,c].

4.7 Conclusion

We have investigated capillary thinning of entangled polymer solutions focusing on weakly elastic systems showing exponential diameter decay.

The tilted CaBER method has been used to determine the force ratio X and the true elongational viscosity η_e. The force ratio decays exponentially and levels off at $X_\infty = 1$ for the PEO solutions with high elasto-capillary numbers Ec_0. However, for the PS and CPyCl/NaSal/NaCl solutions with $Ec_0 \leq 1$ an intermediate Newtonian thinning regime was confirmed based on the measured force ratio $X = 0.713$ as already suggested by Clasen [Clasen 2010]. The initial stress decay after step strain filament formation is characterized by a relaxation time λ_X equal to the relaxation time λ_e determined from the terminal exponential thinning region. Obviously, the corresponding initial decrease of the elongational viscosity η_e is controlled by the same molecular processes like the increase of η_e (strain hardening) in the final regime of thinning. Since η_e goes through a distinct minimum during filament thinning a characteristic minimum Trouton ratio Tr_{min} can be determined accurately. This Trouton ratio decreases exponentially with increasing polymer concentration for all investigated solutions and levels off at $Tr_{min} = 10$ for all PEO solutions irrespective of solvent viscosity. For the PS and CPyCl/NaSal/NaCl solutions characterized by low elasto-capillary numbers $Tr_{min} = 3$ is found.

The relaxation time ratios λ_e/λ_s decreases exponentially with increasing polymer concentration and the data for all investigates PEO and PS solutions collapse onto a single master curve irrespective of polymer molecular weight, solvent viscosity or temperature when plotted versus reduced concentration $c[\eta]$. This decrease is due to the strong non-linear deformation in CaBER experiments as suggested earlier [Arnolds et al. 2010] but not due to a different weighting of relaxation times in the different flow kinematics.

On the other hand, $\lambda_e \approx \lambda_s$ is found for all investigated CPyCl/NaSal/NaCl solutions clearly indicating that non-linear effects are not relevant in capillary thinning of these "living" polymer systems.

4.8 Acknowledgments

5 Elongational deformation of wormlike micellar solutions

5.1 Synopsis

We have investigated the uniaxial elongation behavior of six different wormlike micelle (WLM) systems covering a broad range of surfactant concentrations c_s and salt/surfactant ratios R using the Capillary Breakup Elongational Rheometry (CaBER).

In the fast-breaking limit (high c_s and R) filament lifetime t_{fil} is controlled by the equilibrium shear modulus G_0 and the breakage time λ_{br} obtained from small oscillatory shear according to $t_{fil}/G_0 \propto \lambda_{br}^{2/3}$ and relaxation time ratios $\lambda_e/\lambda_s \approx 1$ are found.

When reptation dominates (high c_s , low R) $\lambda_e/\lambda_s < 1$ is observed similar as for solutions of covalently bound polymer. In this concentration regime the micellar structure seems not to be affected by the strong elongational flow. In contrast, high filament lifetimes up to 1000 s and λ_e/λ_s values up to 10 are observed at lower c_s irrespective of R. This indicates the formation of elongation induced structures (EIS). A minimum viscosity and a minimum initial diameter are required for creating EIS. Additional filament stretching experiments indicate that a critical total deformation has to be exceeded for structure build-up.

Finally, our experiments reveal a distinct difference regarding the dependence between solutions of linear and branched micelles of filament lifetime on viscosity suggesting that CaBER is a versatile means to distinguish between these structures.

5.2 Introduction

5.2.1 General remarks

Surfactant solutions forming wormlike micelles (WLM) are widely used in home and personal care products (e.g. cosmetics, detergents) [Yang 2002] and are becoming increasingly important in e.g. enhanced oil recovery [Padding 2009], agrochemical spraying [Xue et al. 2008] and drag reduction agents [Arora et al. 2002; Li and Hao 2008; Hadri and Guillou 2010]. Respective applications involve complex flow kinematics with strong extensional components, which can cause large and rapid deformation of the fluid microstructure. The resulting stretching and alignment of micelles leads to a range of unconventional phenomena including flow-induced chain scission [Vasquez et al. 2007; Germann et al. 2013], structure formation [Vasudevan et al. 2010] and elastic instabilities [Pathak and Hudson 2006]. A fundamental understanding of material properties as well as the ability to predict changes that occur within the material during processing is extremely important for industrial application. Investigations so far mainly focused on the shear-banding phenomenon [Britton and Callaghan 1997, 1999; Haward et al. 2012a; Fischer and Callaghan 2001; Salmon et al. 2003], shear-thickening even in dilute solutions [Hu and Matthys 1995; Cappelaere et al. 1994; Hartmann and Cressely 1997a,b,c; Cressely and Hartmann 1998; Hartmann and Cressely 1998; Wheeler et al. 1998; Hu et al. 1998; Nowak 2001; Berret and Serero 2001; Azzouzi et al. 2005; Vasudevan et al. 2008] and the corresponding shear-induced structure (SIS) [Wheeler et al. 1996; Kadoma et al. 1997; Ouchi et al. 2006a,b] using different techniques such as turbidity [Yamamoto and Taniguchi 2012; Schubert et al. 2004; Lerouge et al. 2008; Herle et al. 2005], flow birefringence [Dehmoune et al. 2007; Berret et al. 2002; Wunderlich et al. 1987; Oda et al. 1997; Ouchi et al. 2006b], light scattering [Liu and Pine 1996; Boltenhagen et al. 1997], cryo transmission electron microscopy (cryo-TEM) [Oda et al. 1997; Lu et al. 1998], particle image velocimetry (PIV) [Hu et al. 1998], and small-angle neutron scattering (SANS) [Hofmann et al. 1991; Schmitt et al. 1995; Berret et al. 1998; Münch et al. 1993; Herle et al. 2007; Dehmoune et al. 2009; Lutz-Bueno et al. 2013]. This structure formation phenomenon has been mainly investigated for surfactant systems composed of CTAB/NaSal [Hu et al. 1994; Liu and Pine 1996; Shikata et al. 1988; Kadoma and van Egmond 1998; Humbert and Decruppe 1998; Vasudevan et al. 2008; Dehmoune et al. 2009; Lutz-Bueno et al. 2013] and CPyCl/NaSal [Wheeler et al. 1998; Fischer et al. 2002; Callaghan et al. 1996; Mair and Callaghan 1997; Britton and Callaghan 1999; Schmitt et al. 1994] but so far this effect is not yet fully understood and very little is known about extensional thickening and structure formation in extensional flow. In this study we use Capillary Breakup

Elongational Rheometry (CaBER) to get a deeper insight into the rheological behavior and flow-induced structural change of WLM solutions in uniaxial elongational flow. In particular two aspects are covered. In the first part of this paper, general observations of filament formation and subsequent thinning of WLM solutions are discussed in detail. In the second part, elongational material properties such as filament lifetime and elongational relaxation time are related to corresponding shear parameters and the occurrence of elongation-induced structures (EIS) is discussed in detail. Prior to presenting our results we describe the state of art regarding the behavior of WLM solutions in elongational flows particularly focusing on the CaBER method and its application to WLM systems. We finish this paper with a short conclusion.

5.2.2 Capillary Breakup Extensional Rheometry (CaBER)

In CaBER experiments [Bazilevsky et al. 1990; Entov and Hinch 1997; Bazilevsky et al. 2001; McKinley 2005] a fluid drop is placed between two plates and subsequently exposed to an extensional step strain thus forming an unstable liquid filament. The following thinning process of the fluid filament is driven by capillary stresses and resisted by viscous and/or elastic stresses developed in the liquid thread during flow. The CaBER technique can be applied to liquids covering a wide range of viscosities, from about 50 mPas up to 100 Pas. The technique is straightforward, fast and requires only a small amount of sample ($V < 0.1$ ml) and, in contrast to other techniques, CaBER allows for large Hancky strains up to $\varepsilon = 10$ which are of great significance to technical applications.

In the common CaBER setup, the only measured quantity during filament thinning is the diameter decay $D(t)$ at a single position in the filament. However, different extensions are reported in the literature such as optical shape recognition using a high speed camera [Christanti and Walker 2001b; Niedzwiedz et al. 2009; Nelson et al. 2011; Gier and Wagner 2012; Sattler et al. 2012], force measurement during initial step strain [Klein et al. 2009] as well as during the whole capillary thinning process [Sachsenheimer et al. 2012]. Recently, also a temperature control option has been presented allowing for a uniform temperature distribution within the filament [Sachsenheimer et al. 2014a].

The thinning behavior strongly depends on the type of material. Different characteristic diameter vs. time curves are reported in the literature [McKinley 2005]. For Newtonian fluids, a slightly non-cylindrical filament shape is observed and the corresponding minimum diameter decreases linearly according to [Papageorgiou 1995; McKinley and Tripathi 2000;

Sachsenheimer et al. 2012]

$$D(t) = D_1 - 0.1418\frac{\Gamma}{\eta_0}t \ , \tag{5.1}$$

where Γ is the surface tension, η_0 is the viscosity of the Newtonian fluid, and D_1 is the diameter at the beginning of the linear decay. For viscoelastic fluids such as polymer solutions [Bazilevsky et al. 1990; Entov and Hinch 1997; Anna and McKinley 2001; Arnolds et al. 2010; Clasen 2010; Sachsenheimer et al. 2012, 2014a] or surfactant solutions [Yesilata et al. 2006; Bhardwaj et al. 2007a; Chellamuthu and Rothstein 2008; Miller et al. 2009; Kim et al. 2010; Sachsenheimer et al. 2014a], cylindrical filaments are observed and at least in a certain stage of thinning the diameter decreases exponentially with time according to

$$D(t) \propto \exp\left(-\frac{t}{3\lambda_e}\right) \ , \tag{5.2}$$

where λ_e is the elongational relaxation time. Differences between this elongational relaxation time and the characteristic shear relaxation time λ_s obtained from small amplitude oscillatory shear are related to the strong non-linear deformation in CaBER experiments [Arnolds et al. 2010; Sachsenheimer et al. 2014a]. The exponential diameter decay directly corresponds to an exponentially increasing viscosity which has its physical origin in the loss of entropy during stretching of e.g. polymer molecules or wormlike micellar structures.

5.2.3 Elongational flow of WLM solutions

The elongational rheology of WLM solutions is, up to now, poorly understood. Early investigations were based on opposed jet experiments [Fischer et al. 1997; Lu et al. 1998; Prudhomme and Warr 1994; Walker et al. 1996; Chen and Warr 1997], four-roll mill experiments [Kato et al. 2002, 2004, 2006], entrance flow [Okawara et al. 2008, 2009], two-dimensional squeeze flow [Takahashi et al. 2001] and flow through porous media experiments [Muller et al. 2004] showing an elongational hardening (increase of elongational viscosity with increasing elongation rate) of WLM solutions which is attributed to strong alignment of the micelles in flow direction. However, all these experiments were not purely extensional or had an unknown pre-shear history.

Recently, extensional rheology of WLM has been investigated using continuous filament stretching (FiSER) or capillary thinning (CaBER) experiments [Rothstein 2003; Yesilata et al. 2006; Bhardwaj et al. 2007a,c; Chellamuthu and Rothstein 2008; Miller et al. 2009; Kim et al. 2010; Sachsenheimer et al. 2014a] which allow for applying a purely extensional flow field to these low-viscosity liquids.

Yesilata [Yesilata et al. 2006] have used the CaBER method to measure the extensional behavior of erucyl bis(hydroxyethyl)methylammonium chloride (EHAC) and iso-propanol in a brine of ammonium chloride in deionized water. These solutions clearly form exponentially thinning cylindrical filaments. The elongational relaxation time λ_e was about a factor of three lower than the longest relaxation time λ_s calculated from small amplitude oscillatory shear measurements. This is different from CaBER results for Boger fluids where $\lambda_e \approx \lambda_s$ was found [Anna and McKinley 2001] but similar to concentrated polymer solutions [Oliveira et al. 2006; Arnolds et al. 2010; Clasen 2010; Sachsenheimer et al. 2014a]. Later CaBER measurements for a series of CTAB/NaSal solutions showed that the ratio of the extensional relaxation time and the shear relaxation time λ_e/λ_s starts at values less than one ($\lambda_e/\lambda_s = 0.5$) and increases linearly with increasing surfactant concentration, eventually reaching a plateau at roughly $\lambda_e/\lambda_s \approx 1$ [Bhardwaj et al. 2007a]. The onset of the plateau corresponds approximately to the surfactant concentration where a maximum in zero-shear viscosity is observed for a given salt/surfactant ratio. For CPyCl/NaSal solutions λ_e/λ_s also begins at a value much less than one ($\lambda_e/\lambda_s = 0.2$) and then monotonically increases with increasing surfactant concentration but without reaching a plateau value at large surfactant concentrations.

The only study addressing the role of branching on the extensional rheology of WLM has been performed by Chellamuthu and Rothstein [Chellamuthu and Rothstein 2008]. For a series of linear and branched WLM solutions of sodium oleate (NaOA) and octyltrimethyl ammonium bromide (C_8TAB) these authors observe a dramatic decrease of relaxation time ratio λ_e/λ_s in CaBER and a maximum Trouton ratio in FiSER with the onset of branching. They hypothesize that this is due to the additional stress relief mechanisms caused by sliding or ghost-like crossing effects which are supposed to be more efficient in elongational flows. This study suggests that transient extensional rheology might be suitable to distinguish between branched and linear micelles. Other mechanical techniques are so far not available for differentiating branched WLM solutions from linear entangled micelle solutions [Decruppe and Ponton 2003]. Also in neutron or light scattering experiments, linear micelles and branched micelles show similar behavior. So far, the only method that can directly distinguish linear and branched micelles is cryo-TEM [Danino et al. 2000, 2001; Croce et al. 2003; Ziserman et al. 2004; Abezgauz and Danino 2007; Helgeson et al. 2010; Danino 2012]. All these studies have indicated that the first viscosity maximum occurring at a critical salt/surfactant ratio R_{max} is attributed to the transition from linear to branched micelles.

Using the CaBER technique, Sachsenheimer et al. [Sachsenheimer et al. 2014a] recently reported a detailed analysis of CPyCl/NaSal ($R = 0.5$) dissolved in aqueous solution of 500 mM sodium chloride (NaCl). These solutions with different surfactant concentrations

between 40 mM and 120 mM show an intermediate Newtonian thinning region ($X = 0.713$) followed by visco-elastic thinning indicated by a change of the dimensionless fore ratio from $X = 0.713$ to $X = 1$ where $X = F/\pi\Gamma D$ is defined as the ratio of the true axial force F in the filament and the force due to surface tension ($\pi\Gamma D$). The exponential diameter decay allows for a robust determination of the elongational relaxation time λ_e and a relaxation time ratio $\lambda_e/\lambda_s \approx 1$ was found independent of surfactant concentration. This indicates that the equilibrium conformation of the WLM is not affected by the strong elongational flow during capillary thinning.

There are only a few studies dealing with a structure build-up in elongational flows. Combining the opposed nozzle technique with small-angle light scattering (SALS) the apparent elongational viscosity and the radius of gyration R_G in elongational direction of a WLM (TTAB/NaSal) solution were determined simultaneously. Both quantities exhibit a pronounced maximum upon variation of strain rate $\dot{\varepsilon}$ at the same critical value. The decrease of the elongational viscosity and R_G is attributed to the scission of micelles as predicted theoretically [Vasquez et al. 2007; Cromer et al. 2009; Germann et al. 2013]. However, it could not be resolved whether the increase in R_G observed at low elongation rates is just due to alignment and elongation of micelles in flow direction or whether fusion of micelles occurs increasing the average micellar contour length [Chen and Warr 1997]. Okawara et al. [Okawara et al. 2008, 2009] investigated the pressure loss Δp of CTAB/NaSal ($c_s = 30$ mM) solutions at high salt/surfactant ratios R flowing through two different converging channels and analyzed structural changes using simultaneous SALS experiments. For a distinct apparent elongation rate regime (regime II), a strong increase of Δp with increasing elongational rate has been observed. Corresponding SALS measurements show a combination of butterfly-type and streak-type pattern indicating a structure build-up. A further increase of the apparent elongation rate (regime III) results in a weaker increase of Δp with increasing $\dot{\varepsilon}$ than in regime II and a change in the SALS patterns indicates a less pronounced structure build-up at these elevated elongation rates. Furthermore, the measurements of Okawara et al. show that the creation of elongation-induced structures (EIS) depends not only on the elongational rate but also on the total Hencky strain.

Takahashi et al. [Takahashi and Sakata 2011] investigated the flow induced structure build-up of similar CTAB/NaSal solutions ($c_s = 30$ mM, $R > 1$) in planar elongation using a squeeze flow device. In this setup elongational deformation is dominant in the center plane whereas shear dominates close to the walls. Structure formation was verified by the occurrence of opaque regions during flow at the rim close to the walls (shear-induced structure, SIS) as well as in the center plane (elongation-induced structure, EIS). SIS was observed at shorter elapsed times than EIS but at significantly higher critical strains and strain rates.

Furthermore, the elongation-induced structures occurred at a critical total strain ε_c irrespective of the salt/surfactant ratio R but all solutions had R values corresponding to the fast breaking limit (branched micelles). To our knowledge these are the only studies directly showing structure build-up in elongational flow of WLM solutions.

In summary, the extensional flow properties of WLM solutions deserve further exploration. Despite some data in the literature [Bhardwaj et al. 2007a; Chellamuthu and Rothstein 2008] a systematic investigation of extensional flow behavior as a function of R covering both viscosity maxima (if present) is still lacking and there are still uncertainties and questions that remain open. First, the variation and interpretation of the elongational relaxation time λ_e and its relation to the shear relaxation time λ_s as a function of surfactant or salt concentration is unclear. The question whether extensional rheology is able to distinguish between linear and branched micelles is also still open. Furthermore, the phenomenon of structure build-up during elongational flow is almost uninvestigated.

5.3 Experimental setup and sample preparation

5.3.1 Capillary Breakup Extensional Rheometry (CaBER)

In our setup, the CaBER-1 (Thermo Scientific, Karlsruhe) is extended with an optical train, including a high speed camera (Photron Fastcam-X 1024 PCI) as well as a telecentric objective (MaxxVision TC4M 16, magnification: x1) and blue telecentric backlight illumination (Vision & Control TZB30-B), allowing for full filament assessment with high spatial and temporal resolution of 16 μm/px and up to 3000 fps. In case of very stable filaments, the high-speed camera has been replaced by a PIKE CCD camera (Allied Vision Technologies) achieving a frame rate of 10 fps. Further details about the experimental setup and the data analysis are given in Niedzwiedz et al. and Sachsenheimer et al. [Niedzwiedz et al. 2009; Sachsenheimer et al. 2012]. A representative sketch of the experiment can be found e.g. in Bhardwaj et al. [Bhardwaj et al. 2007a] Plates with a diameter $D = 6$ mm are used in all experiments. Filaments are stretched from $h_i = 1.5$ mm to $h_f = 6$ mm within a strike time of $t_s = 40$ ms as discussed in section 5.4.1. Our customized temperature control unit [Sachsenheimer et al. 2014a] was used for measurements at elevated temperatures. Furthermore, this unit providing a saturated athmosphere thus preventing solvent evaporation was used for measurements of solutions showing high filament lifetimes.

5.3.2 Filament Stretching Extensional Rheometer (FiSER)

Liquid filaments were stretched continuously using the home made FiSER setup of Prof. Rothstein at the University of Massachusetts [Anna et al. 2001; Rothstein and McKinley 2002a,b; Rothstein 2003]. Plates with a diameter $D = 5$ mm and an initial displacement $L_0 = 0.75$ mm were separated with increasing speed in order to achieve a constant stretching rate according to

$$\dot{\varepsilon}_L = \frac{1}{L} \frac{\mathrm{d}L}{\mathrm{d}t} \tag{5.3}$$

A metal grid was glued onto the plates to increase the adhesion between plates and liquids under test. The diameter vs. time curve was recorded using a laser micrometer. Unfortunately, axial forces were too low so that only the evolution of $D(t)$ could be recorded. Filament stretching experiments were performed at room temperature of 25°C $\pm$ 3°C.

5.3.3 Shear rheology

Steady shear experiments and small amplitude oscillatory shear (SAOS) were performed using a MARS II (Thermo Fischer, Karlsruhe, Germany) equipped with a cone plate fixture (60 mm diameter and 1° cone angle) or a coaxial cylinder system (Z20DIN) depending on sample viscosity.

Steady shear data were obtained in a shear rate range of $\dot{\gamma} = 0.1 - 500$ s^{-1}. A sudden increase of viscosity occurring for CTAB/NaSal and CPyCl/NaSal solutions at a critical shear rate was taken as evidence for shear-induced structure (SIS) formation because these systems are well known to undergo structural formations during non-linear deformation [Liu and Pine 1996; Wheeler et al. 1998; Herle et al. 2005; Ouchi et al. 2006b; Vasudevan et al. 2008; Takahashi and Sakata 2011; Lutz-Bueno et al. 2013].

during flow.

The shear modulus $G^* = G' + iG''$ was obtained from small amplitude oscillatory shear experiments covering the frequency range $\omega = 0.01 - 50$ rad/s. Based on these measurements the terminal shear relaxation time and the zero shear viscosity

$$\lambda_s = \lim_{\omega \to 0} \frac{G'}{G'' \, \omega} \qquad \text{and} \qquad \eta_0 = \lim_{\omega \to 0} \frac{G''}{\omega} \tag{5.4}$$

were determined.

High frequency shear modulus data were obtained from oscillatory squeeze flow experiments using a piezo-driven axial vibrator (PAV) described in Crassous et al. and Oelschlaeger et al. [Crassous et al. 2005; Oelschlaeger et al. 2009]. These experiments cover the frequency

range up to $\omega = 50,000$ rad/s and were used for a reliable assessment of the plateau modulus G_0 and the breakage time $\lambda_{br} = 1/\omega\,(G''_{min})$ [Fischer and Rehage 1997; Yesilata et al. 2006].

5.3.4 Additional Techniques

Surface tension Γ has been determined for CPyCl/NaSal and CTAB/NaSal solutions with an experimental error of $\Delta\Gamma = \pm 1$ mN /m using a DCAT1 tensiometer (DataPhysics, Filderstadt, Germany) equipped with a platinum-iridium Wilhelmy-plate at $T = 20°$C.

5.3.5 Test fluids

The surfactants hexadecyltrimethylammonium bromide (CTAB) and cetylpyridinium chloride (CPyCl) as well as the salts sodium salicylate (NaSal), potassium bromide (KBr), sodium nitrate (NaNO$_3$), sodium chlorate (NaClO$_3$) and sodium chloride (NaCl) were purchased as powder with a purity of at least 98% from Carl Roth GmbH (Karlsruhe, Germany) and were used without further treatment. Surfactants and salts were dissolved in distilled water and homogenized by means of shaking for five days at room temperature. Solutions were then stored for another five days before measuring to ensure the formation of the equilibrium micelles structure. Solutions of CPyCl/NaSal, CTAB/NaSal, CTAB/KBr, CTAB/NaNO$_3$, and CTAB/NaClO$_3$ were prepared at constant surfactant concentration but different salt/surfactant ratios R covering the dilute and semi-dilute regime. For the sake of clarity it should be noted that all concentrations given in this paper refer to the concentration of the surfactant molecules and not to the total concentration of both, surfactant and salt. For selected R values the systems CPyCl/NaSal and CTAB/NaSal were analyzed at differ-

Table 5.1: Investigated salt/surfactant systems with measurement temperatures

| System	Surfactant concentration	Measurement temperature
CPyCl/NaSal	5 mM - 100 mM	20°C
CPyCl/NaSal/NaCl	40 mM - 120 mM	25°C
CTAB/NaSal	5 mM - 25 mM	20°C
CTAB/KBr	150 mM	35°C
CTAB/NaNO$_3$	75 mM	25°C
CTAB/NaClO$_3$	150 mM	30°C

ent surfactant concentrations. In addition, CPyCl/NaSal/NaCl solutions were prepared at a fixed CPyCl/NaSal ratio of $R = 0.5$ with surfactant concentrations between 40 mM and 120

mM and a NaCl concentration of 500mM as described by Berret et al [Berret et al. 1993]. Different measurement temperatures were applied in order to prevent crystallization of the surfactant solutions. Sample compositions and measurement temperatures are summarized in table 5.1.

Figure 5.1A shows the variation of the zero shear viscosity η_0 as a function of salt/surfactant ratio R for WLM solutions with constant surfactant concentration investigated in this study. Corresponding values for CPyCl/NaSal/NaCl solutions are shown elsewhere [Berret et al. 1993]. At low salt/surfactant ratios R, all systems show an increase of the zero shear viscosity with increasing R in good agreement with earlier observations (e.g. [Rehage and Hoffmann 1988; Azzouzi et al. 2005; Oelschlaeger et al. 2009, 2010]). At higher salt/surfactant ratios, differences between the different surfactant solutions occur. For CPyCl/NaSal and CTAB/NaSal, the viscosity as a function of the salt/surfactant ratio R shows two maxima but only one broad viscosity maximum is observed for CTAB/NaClO$_3$. The systems CTAB/NaNO$_3$ and CTAB/KBr show a monotonic increase of viscosity in the investigated R range. For CPyCl/NaSal and CTAB/NaSal solutions the first viscosity maximum occurs at the same salt/surfactant ratio of $R_{max} = 0.6 \pm 0.1$. In order to study differences in capillary thinning at similar zero shear viscosity η_0 the surfactant concentrations for these two systems were chosen such that η_0 values obtained for $R < R_{max}$. The shear relaxation time was analyzed in two different ways: the terminal shear relaxation time λ_s (figure 5.1B) calculated according to equation 5.4 and the crossover relaxation time $\lambda_{s,c}$ defined as the inverse of the crossover frequency at which $G' = G''$. Shear relaxation time ratios $\lambda_s/\lambda_{s,c} = 1$ are found for solutions in the fast breaking limit with $R > R_{max}$ where R_{max} denotes the salt/surfactant ratio at which the first viscosity maximum occurs. For $R < R_{max}$, $\lambda_s > \lambda_{s,c}$ is observed corresponding to a multi-exponential decay of the shear stress. In the following, only the terminal shear relaxation time λ_s will be considered. However, for very low R values the terminal flow region where $G' \propto \omega^2$ and $G'' \propto \omega$ could not be observed. In these cases the zero shear viscosity was determined from steady shear experiments but no λ_s values could be obtained.
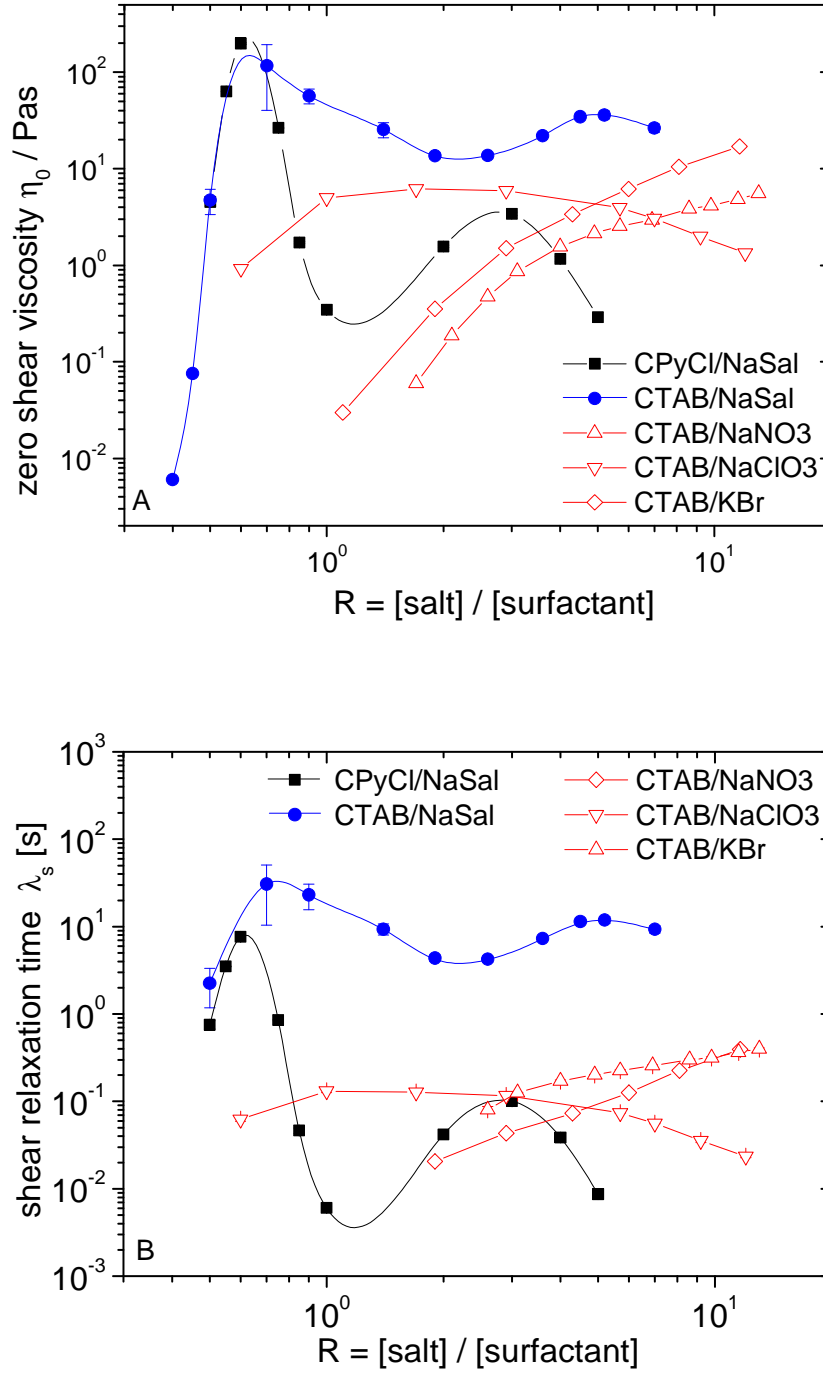
Figure 5.1: Zero shear viscosity η_0 (top) and terminal shear relaxation time λ_s (bottom) as a function of the salt/surfactant ratio R for 100 mM CPyCl/NaSal (measurement temperature $T = 20°C$), 25 mM CTAB/NaSal ($T = 20°C$), 75 mM CTAB/NaNO$_3$ ($T = 25°C$), 150 mM CTAB/NaClO$_3$ ($T = 30°C$), and 150 mM CTAB/KBr ($T = 30°C$) solutions. Lines are to guide the eye.

5.4 Results and discussions

5.4.1 Choice of step-strain parameters in CaBER experiments for WLM solutions

The step-strain parameters initial gap height h_i, final gap height h_f and strike time t_s set in a CaBER experiment may have a strong effect on the subsequent capillary thinning process, since they determine the initial filament diameter as well as the axial stress within the filament.

In preliminary experiments four different sets of h_i and h_f have been used ($h_i = 0.5$ mm and $h_f = 6$ mm , $h_i = 1.5$ mm and $h_f = 11$ mm, $h_i = 1.5$ mm and $h_f = 8$ mm as well as $h_i = 1.5$ mm and $h_f = 6$ mm) in order to elucidate their effect on filament thinning. Initial gap heights $h_i > 1.5$ mm are not feasible, due to the low surface tension of the investigated fluids. The liquid under test flows out of the gap and a correct filling is not possible. If the ratio h_f/h_i is chosen too high, filaments break before the upper plate has reached its end position, e.g. for $h_f = 6$ mm and $h_i = 0.5$ mm uniform filaments could only be formed for the 100 mM CPyCl/NaSal solutions with $R = 0.5$ and $R = 5$. Tilted CaBER experiments on CPyCl/NaSal/NaCl and CTAB/NaSal [Sachsenheimer et al. 2014a] have revealed that high axial normal stresses σ_{zz} occur during the initial period of thinning and we suppose that filament rupture occurs during the step strain period when σ_{zz} exceeds a critical value the filament can bear. This idea is supported by FiSER experiments on CTAB/NaSal solutions where a critical axial normal stress at filament rupture independent of elongation rate was found [Bhardwaj et al. 2007a].

Choosing $h_i = 1.5$ mm and $h_f = 6$ mm enabled us to characterize the capillary thinning of WLM solutions in a broad range of surfactant concentrations and salt/surfactant ratios R covering both viscosity maxima and hence spanning several orders of magnitude with respect to shear viscosity. The influence of the strike time t_s on the filament lifetime t_{fil} was investigated for CPyCl/NaSal and CTAB/NaSal solutions covering both viscosity maxima and ts was varied between $t_s = 20$ ms and $t_s = 160$ ms. Longer strike times are not recommended because of a potential superposition of filament stretching and capillary thinning [Sachsenheimer et al. 2014a]. However, no variations of the filament lifetime was found within experimental error in contrast to the observations of Miller et al. [Miller et al. 2009] who reported a significant influence of t_s and h_f on the filament lifetime but in good agreement with the results of Kim et al. [Kim et al. 2010] who could not recover an influence of initial step strain parameters on the elongational relaxation time.

## 5.4.2 Characteristic filament shape and diameter decay

In the following filament formation and subsequent capillary thinning will be discussed based on results obtained for CPyCl/NaSal and CTAB/NaSal solutions. Three characteristic types of filament shape and diameter evolution are observed for these WLM solutions. Typical pictures of fluid filaments at different stages of thinning are shown in figure 5.2.
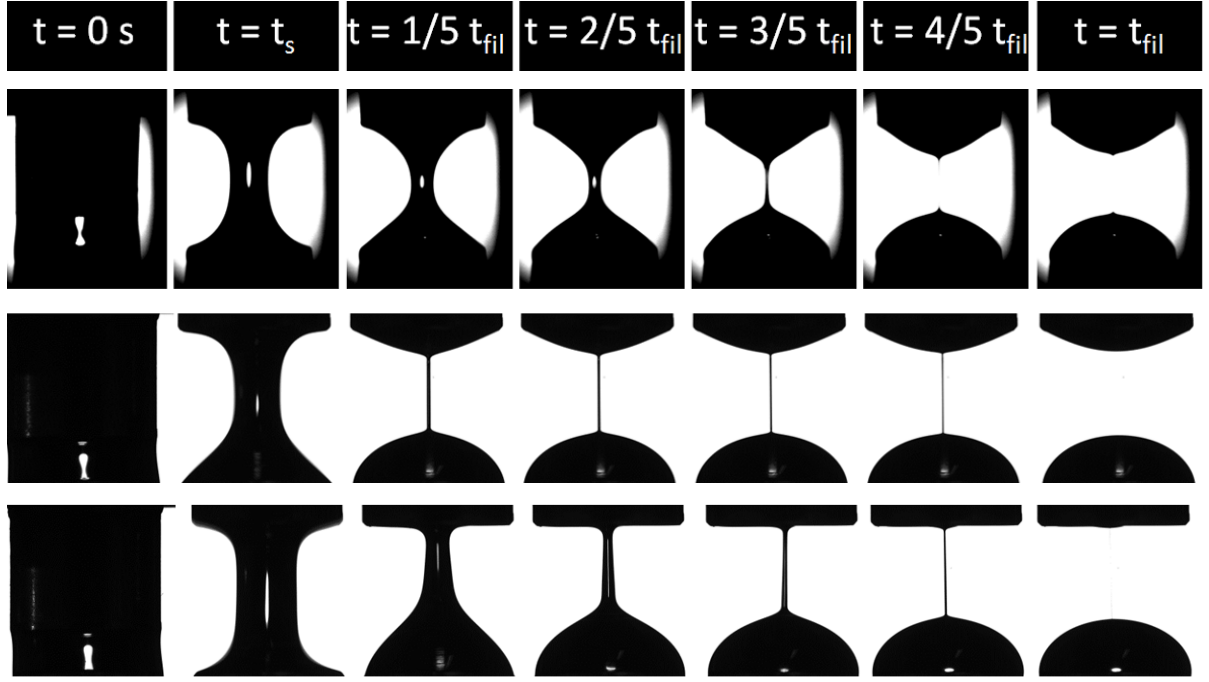
Figure 5.2: Typical images of fluid filaments taken during CaBER experiments ($h_i = 1.5$ mm, $h_f = 6$ mm , $t_s = 40$ ms) at different stages of capillary thinning relative to the filament lifetime t_{fil} for 100mM CPyCl/NaSal with $R = 0.5$ (top), 25mM CTAB/NaSal with $R = 0.5$ (middle) and 25 mM CTAB/NaSal with $R = 4.5$ (bottom).

Filaments made from the CPyCl/NaSal solutions show a cylindrical region near the midpoint of the thread only in the final stage of thinning ($t > 3/5 t_{fil}$) whereas a curved filament shape is observed at the beginning of the thinning process. This shape evolution is typical for viscoelastic fluids where the thinning process is initially controlled by viscous and capillary forces until finally elasto-capillary thinning dominates [Clasen 2010; Sachsenheimer et al. 2014a]. The Newtonian response also shows up in the linear decrease of the filament diameter during the early thinning period, whereas exponential filament diameter decay is observed in the final stage controlled by elasto-capillary thinning as shown in figure 5.3. Similar results were found for CPyCl/NaSal/NaCl solutions analyzing the axial force in the liquid thread [Sachsenheimer et al. 2014a]. Finally, the fluid filament breaks and in certain cases this is preceded by a bead-on-a-string structure, but this phenomenon is not discussed in this

paper. Filament lifetime for these CPyCl/NaSal solutions varies between $t_{fil} \approx 0.2$ s and $t_{fil} \approx 60$ s depending on the salt/surfactant ratio R.
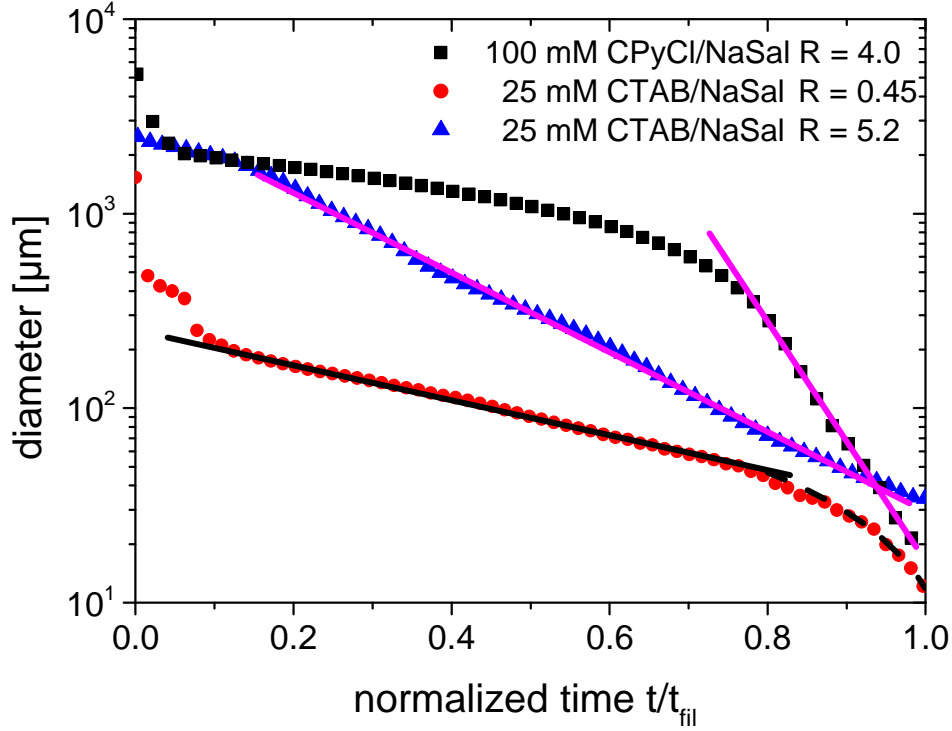
Figure 5.3: Filament diameter as a function of normalized time t/t_{fil} determined at $T = 20°C$ for 100 mM CPyCl/NaSal with $R = 4.0$ ($\eta_0 = 1.2$ Pas and $t_{fil} = 0.8$ s) as well as 25 mM CTAB/NaSal with $R = 0.4$ ($\eta_0 = 0.076$ Pas and $t_{fil} = 107$ s) and $R = 5.2$ ($\eta_0 = 36.2$ Pas and $t_{fil} = 70$ s). Number of shown data points is reduced for sake of clarity. The solid lines represent the exponentially thinning region where the elongational relaxation time is determined. The curve line represents the late Newtonian thinning regime observed for CTAB/NaSal at $R = 0.45$and is a fit of equation 1 to the experimental data in the time range $0.8 < t/t_{fil} < 1$.

The investigated CTAB/NaSal solutions show a different characteristic filament shape and diameter vs. time curve at low ($R < R_{max}$) and high ($R > R_{max}$) salt/surfactant ratio. At low R (figure 5.2 middle), the filaments of CTAB/NaSal solutions exhibit a perfect cylindrical shape during the whole thinning process as expected for viscoelastic solutions. The diameter D_1 determined right after the upper plate has reached the end position ($t = t_s$) is significantly smaller than for CPyCl/NaSal solutions or CTAB/NaSal solutions with $R > R_{max}$ due to the low-viscosity of this solution. The corresponding diameter vs. time curve (figure 5.3) shows an extended regime of exponential thinning diameter followed by a linear decay prior to breakup. In this R range filament lifetimes vary between $t_{fil} \approx 50$ s

and $t_{fil} \approx 800$ s.

CTAB/NaSal solutions with high R values exhibit an asymmetric filament in the early stage of thinning controlled by gravitational sagging (Bond number Bo $= \rho g D^2/\Gamma > 1$). As the thinning proceeds further a cylindrical filament shape with exponentially decreasing diameter until filament breakage is observed. Filament lifetimes vary between $t_{fil} \approx 40$ s and $t_{fil} \approx 800$ s.

All three thinning periods (early Newtonian, visco-elastic and late Newtonian) observed here for WLM solutions can be covered using a FENE-P model [Entov and Hinch 1997]. In addition, the occurrence of an early Newtonian thinning regime has been associated with the dimensionless elasto-capillary number Ec $= 2\lambda_s\Gamma/\eta_0 D$ which is the dimensionless ratio of the elastic stress and capillary pressure within the filament [Anna and McKinley 2001; Clasen et al. 2006b; Clasen 2010; Sachsenheimer et al. 2014a]. Furthermore, the late Newtonian regime has been attributed to the finite extensibility parameter of polymer molecules or WLM structures [Entov and Hinch 1997; Rothstein 2003; Chellamuthu and Rothstein 2008]. However, an exponentially decreasing diameter region allowing for an unambiguous determination of the elongational relaxation time λ_e is found for all WLM solutions investigated in this study.

5.4.3 Filament thinning behavior of CPyCl/NaSal and CTAB/NaSal solutions

In figure 5.4 filament lifetime t_{fil} is plotted as a function of the salt/surfactant ratio R for the 100 mM CPyCl/NaSal and the 25 mM CTAB/NaSal solutions. These surfactant concentrations are compared here because they yield similar η_0 and λ_s values for $R < R_{max}$. Here we plot t_{fil} which can be determined from $D(t)$ in a straight forward manner. However, the elongational relaxation time λ_e obtained from the exponential diameter decay regime exhibits a similar dependency on R and reveals the same differences between the CPyCl and CTAB systems.

Significant differences between the CTAB/NaSal and CPyCl/NaSal system show up in the CaBER experiments, even at low R values where the shear rheological properties η_0 and λ_s are nearly identical (see figure 5.1). In the whole salt concentration range t_{fil} or λ_e is (up to three orders of magnitude) higher for the CTAB/NaSal system than for the CPyCl/NaSal system. The maximum filament lifetime is $t_{fil}^{max} \approx 1000$ s and $t_{fil}^{max} \approx 60$ s for CTAB/NaSal and CPyCl/NaSal, respectively. It should be kept in mind that the CTAB concentration at which such stable filaments occurs is only a fourth of the CPyCl concentration. The long filament lifetimes observed for CTAB/NaSal solutions at low R values are most likely
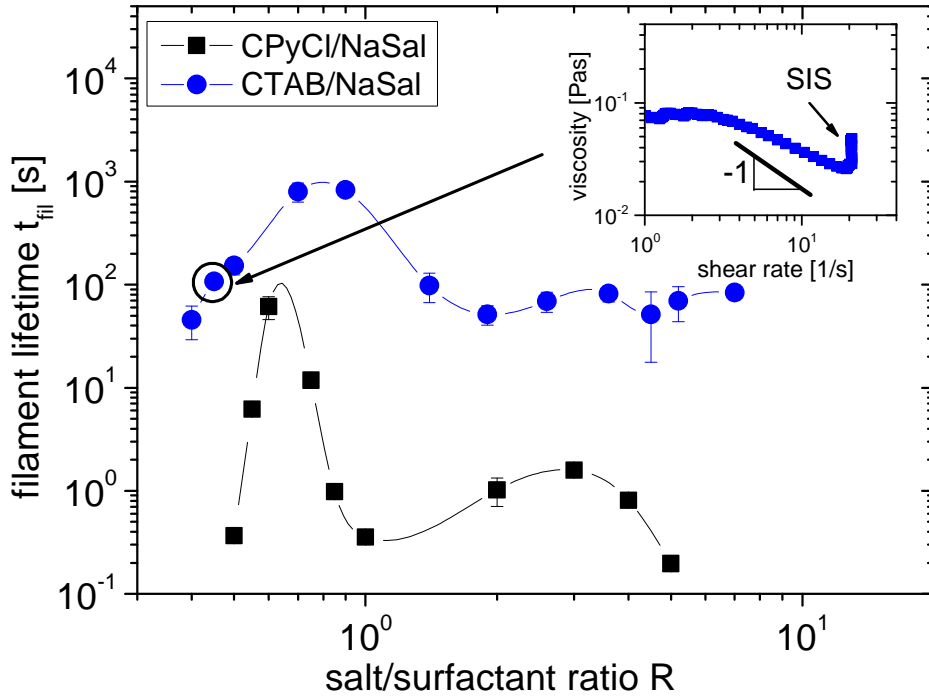
Figure 5.4: Filament lifetime t_{fil} as a function of salt/surfactant ratio R for 100mM CPyCl/NaSal and 25 mM CTAB/NaSal at $T = 20°$C. Lines are to guide the eye.

due to an elongation-induced structure (EIS) formation because the system CTAB/NaSal is known to undergo structural changes during flow [Liu and Pine 1996; Ouchi et al. 2006b; Vasudevan et al. 2008; Lutz-Bueno et al. 2013] in the concentration range in which our CaBER experiments indicate EIS. This structure formation effect is mostly investigated in shear flows [Liu and Pine 1996; Ouchi et al. 2006b; Vasudevan et al. 2008; Lutz-Bueno et al. 2013] where the shear-induced structure (SIS) shows up in a sudden increase of the steady shear viscosity η at a critical shear rate γ_c (see insert in figure 5.4), critical shear stress or a critical total shear deformation. Generally, the occurrence of shear thickening in WLM solutions can also result from elastic instabilities [Britton and Callaghan 1999; Fardin et al. 2011, 2012b,a; Fardin and Lerouge 2012; Beaumont et al. 2013; Perge et al. 2014]. But in these cases shear banding is observed (elucidated by a slope of -1 in the steady viscosity function) prior to shear thickening. Furthermore, elastic instabilities have been observed for CPyCl/NaSal/NaCl ($c_s = 238$ mM) and CTAB/NaNO3 ($c_s = 30$ mM) [Britton and Callaghan 1999; Fardin et al. 2011, 2012b,a; Fardin and Lerouge 2012] but neither SIS has been reported in the literature, nor did we find any indication of EIS. Interestingly, capillary thinning behavior of solutions showing shear banding (fast braking limit, $R > R_{max}$) is controlled by linear viscoelastic shear properties (see section 5.4.4). So

it seems flow instabilities do not occur in this flow kinematics. The phenomenon of long stable filaments will be discussed in more detail below.

5.4.4 Fast breaking limit

Shear and elongational relaxation times are compared in figure 5.5 showing the relaxation time ratio λ_e/λ_s as a function of salt/surfactant ratio R for the 100 mM CPyCl/NaSal and the 25 mM CTAB/NaSal systems. For high R, i.e. in the fast breaking limit, linear viscoelastic
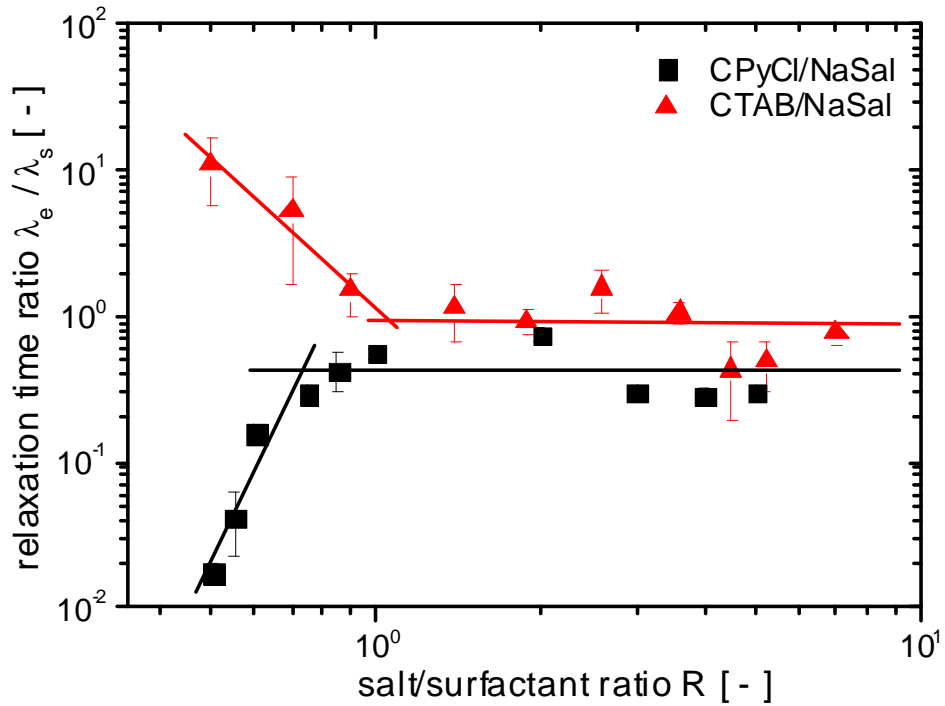
Figure 5.5: Relaxation time ratio λ_e/λ_s as a function of salt/surfactant ratio R for 100 mM CPyCl/NaSal and 25 mM CTAB/NaSal at $T = 20°$C.

shear relaxation is described by a single-mode Maxwell model in a wide frequency range (see e.g. insert in figure 5.6). The relaxation time ratio λ_e/λ_s is fairly independent of R. The difference between $\lambda_e/\lambda_s = 0.4 \pm 0.2$ for CPyCl/NaSal solutions and $\lambda_e/\lambda_s = 0.9 \pm 0.4$ for CTAB/NaSal solutions may be explained by differences in micellar flexibility. More importantly, finding a constant relaxation time ratio of $\lambda_e/\lambda_s \approx 1$ indicates that the capillary thinning behavior is characterized by linear material properties which can be obtained from simple oscillatory shear experiments (see also [Sachsenheimer et al. 2014a]).

This hypothesis is further supported by the universal scaling of the reduced filament lifetime t_{fil}/G_0 with the equilibrium micellar breakage time λ_{br} shown in figure 5.6 summarizing data for six different WLM systems at different surfactant concentrations, salt/surfactant ratios,
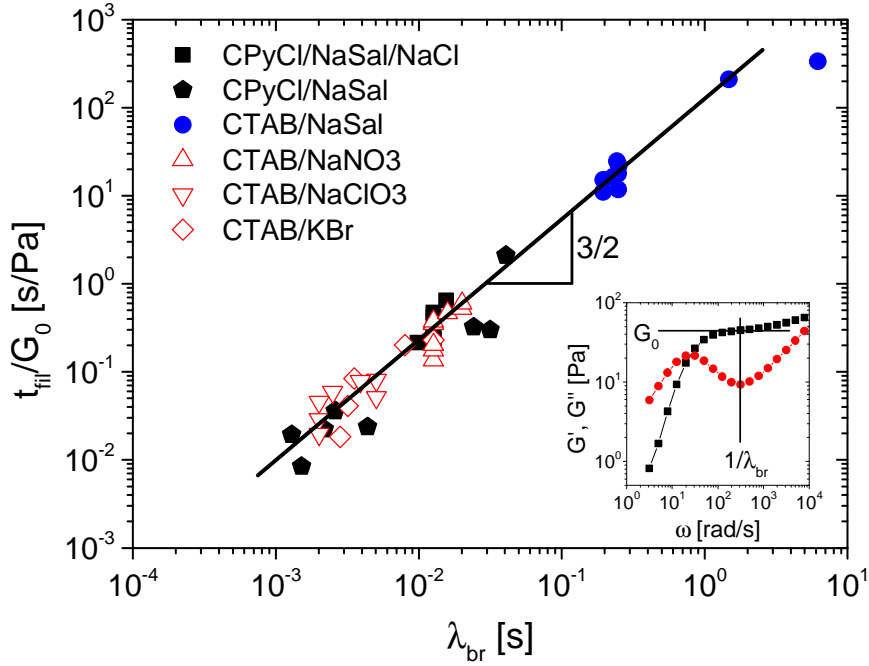
Figure 5.6: Ratio of filament lifetime and plateau modulus as a function of the breakage time of the micelles for different WLM solutions as mentioned in the diagram. Different data points represented by the same symbol refer to different R values or in case of CPyCl/NaSal/NaCl solutions to different surfactant concentrations. The solid line represents a power law fit to the experimental data with an exponent of 3/2. The insert shows the storage and loss moduli for a 25mM CPyCl/NaSal solution ($R = 0.8$) as a function of the angular frequency illustrating the determination of G_0 and λ_{br}. Measurement temperatures are given in table 5.1.

and temperatures. The linear viscoelastic fluid properties G_0 and λ_{br} are determined from small amplitude oscillatory shear experiments (at the same measurement temperature) as illustrated in the insert of figure 5.6 where the storage and loss moduli G' and G'' are plotted against the angular frequency ω. The breakage time is defined as the reciprocal angular frequency at which the loss modulus shows a minimum value, $\lambda_{br} = 1/\omega\,(G''_{min})$, [Fischer and Rehage 1997; Yesilata et al. 2006] and the plateau modulus G_0 is determined from G' at the same angular frequency, $G_0 = G'\,(\omega\,(G''_{min}))$. The ratio of filament lifetime and plateau modulus clearly depends on the breakage time and all data points collapse to one master curve according to $t_{fil}/G_0 \propto \lambda_{br}^{3/2}$ irrespective of the type of surfactant, the behavior of the salt (strongly binding or not), and the measurement temperature. This scaling law also holds for solutions with $\lambda_e/\lambda_s < 1$ as long as a minimum in G'' is still present. A similar scaling is found when t_{fil} is replaced by λ_e. The correlation can also be given in terms of dimensionless numbers dividing the times by $\sqrt{\rho V_i/\Gamma}$, where ρ is the density and V is the

initial sample volume as well as dividing the modulus by the initial Laplace pressure $2\Gamma/D_0$. These findings indicate that no flow-induced structural change occurs in this salt/surfactant regime and the breaking rate of the micelles does not change during elongational flow in a CaBER experiment.

5.4.5 Low salt regime

Striking differences are observed between CPyCl/NaSal and CTAB/NaSal solutions in the low salt limit. For the CPyCl/NaSal system, λ_e/λ_s starts at values much lower than one ($\lambda_e/\lambda_s \approx 0.02$) and increases with increasing salt concentration until the plateau is reached at high R. Relaxation time ratios $\lambda_e/\lambda_s << 1$ found for low R values might be taken as evidence for a flow-induced decrease of the mean length of micelles, but such low λ_e/λ_s values are also observed for solutions of covalently bound polymers in the entangled state and λ_e/λ_s values as low as 0.01 are reported in the literature [Liang and Mackley 1994; Oliveira et al. 2006; Clasen 2010; Arnolds et al. 2010; Sachsenheimer et al. 2014a]. Therefore, it is not very surprising that WLM solutions where the reptation is the dominant stress relaxation mechanism, show $\lambda_e/\lambda_s << 1$. Similar results are also obtained for CTAB/NaNO$_3$, CTAB/NaClO$_3$, and CTAB/KBr solutions at low R values investigated in this study. Nevertheless, structural analysis under elongational flow, e.g. neutron scatting, would be useful for clarifying the origin of these findings unambiguously, but this is beyond the scope of this paper and will be addressed in a subsequent study.

In contrast, the relaxation time ratio of the CTAB/NaSal solutions at low salt concentrations starts at approximately $\lambda_e/\lambda_s = 10$ and decreases with increasing salt/surfactant ratio R reaching a plateau for $R \approx 1 > R_{max}$. Such high relaxation time ratios have never been reported in the literature (to the best of our knowledge) and we hypothesize an elongation-induced structural change stabilizing the filaments as already mentioned above. In this case, λ_e corresponds to the characteristic thinning time scale of the flow-induced structure and λ_s corresponds to the characteristic relaxation time scale of the equilibrium structure of the WLM solutions at rest. This topic will be discussed in more detail below.

5.4.6 Distinguishing between linear and branched micelles

Figure 5.7 shows the filament lifetime t_{fil} as a function of zero shear viscosity η_0 for different WLM solutions investigated in this study. CPyCl/NaSal solutions (figure 5.7a) with similar zero shear viscosity exhibit a significantly lower filament lifetime in the case of linear micelles ($R < R_{max}$) than in the case of branched ones ($R > R_{max}$). Furthermore, the filament lifetime depends more strongly on zero shear viscosity in the linear regime ($t_{fil} \propto \eta_0^{1.3}$)

than in the branched regime ($t_{fil} \propto \eta_0^{0.9}$). For CPyCl/NaSal solutions the change of the micellar morphology from a linear to branched structure at R_{max} is confirmed by rheological measurements [Oelschlaeger et al. 2009] and cryo-TEM studies [Abezgauz and Danino 2007]. Similar results are obtained for the CTAB/NaClO$_3$ system, when solutions with $R < R_{max}$ and $R > R_{max}$ are compared (figure 5.7c). For CTAB/NaNO$_3$ solutions, the scaling exponent $t_{fil} \propto \eta_0^\alpha$ decreases from $\alpha = 1.3$ to $\alpha = 0.9$ at a critical salt/surfactant value $R = 5.7$ indicating a linear to branched micelles transition. This hypothesis is further supported by cry-TEM images [Helgeson et al. 2010] and by Oelschlaeger et al. [Oelschlaeger et al. 2010] who observed a characteristic increase of the plateau modulus G_0 at $R \approx 5.0$ for a 350 mM CTAB/NaNO$_3$ solution.
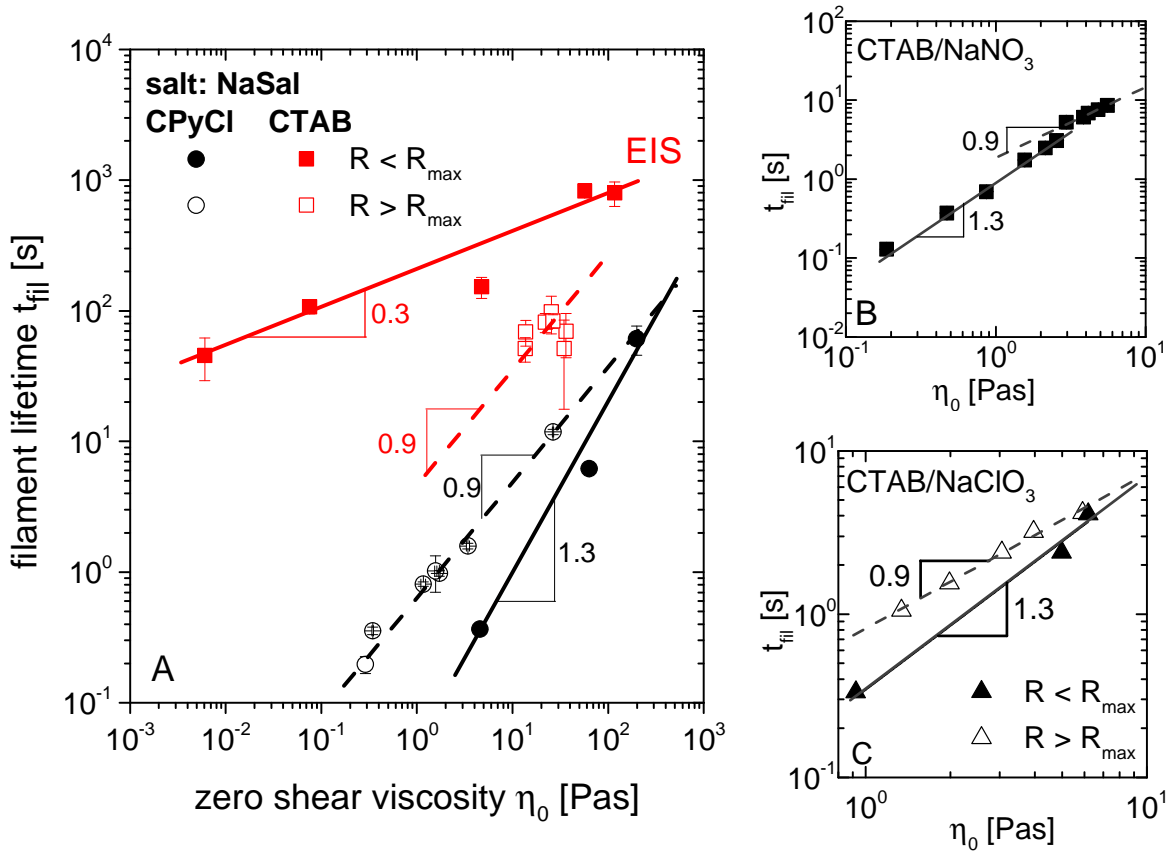
Figure 5.7: Filament lifetime t_{fil} as a function of zero shear viscosity η_0 for 100 mM CPyCl/NaSal, 25 mM CTAB/NaSal (both left, measurement temperature $T = 20°C$), 75 mM CTAB/NaNO$_3$ (top right, $T = 25°C$), and 150 mM CTAB/NaClO$_3$ (bottom right, $T = 30°C$) at $R < R_{max}$ (filled symbols) and $R > R_{max}$ (open symbols).

For the branched CTAB/NaSal solutions with $c_s = 25$ mM and $R > R_{max}$ the filament lifetime t_{fil} hardly changes with the zero shear viscosity η_0, both quantities depend only weakly

on R. This hinders an accurate determination of a scaling exponent but the variation of lifetime with η_0 seems to be consistent with the scaling law $t_{fil} \propto \eta_0^{0.9}$ found for the other systems. However, filament lifetime is much larger for solutions with $R < R_{max}$ than for solutions with $R > R_{max}$ and varies only weakly with zero shear viscosity ($t_{fil} \propto \eta_0^{0.3}$). This is in contrast to the findings for the other systems and is taken as further evidence for EIS occurring in CTAB/NaSal solutions with $R < R_{max}$.

Elongation-induced structure formation also may have occurred in another system investigated by Chellamuthu and Rothstein [Chellamuthu and Rothstein 2008]. They focused on solutions of sodium oleate (NaOA) and octyl trimethyl ammonium bromide (C_8TAB) at a fixed mass ratio of 7:3 and different total surfactant concentrations c_s. For solutions at $c_s < c_{s,max} = 4$ wt.% long filament lifetimes and high maximum Trouton ratios are reported. For $c_s > c_{s,max}$ where micelles show a branched structure [Ziserman et al. 2004] a rapid decrease of the maximum Trouton ratio with increasing c_s is found. This observation was taken as evidence for extremely efficient stress relief mechanisms due to sliding of branching points and ghost-like crossing.

However, the shape of the diameter vs. time curve for NaOA/C_8TAB solutions at $c_s < c_{s,max}$ is very similar to that obtained for CTAB/NaSal solutions at $R < R_{max}$4 (EIS regime). Corresponding steady shear experiments show a sudden increase of viscosity or normal stress difference at a critical shear rate (e.g. $\dot{\gamma} = 94 \pm 7$ s^{-1} for $c_s = 2$ wt.%) supposed to indicate a structure build-up in shear. The drastic change in the elongational behavior occurring around $c_{s,max}$ reported by Chellamuthu and Rothstein seems to be more likely due to a flow-induced structure formation than due to a transition between linear and branched micelles as hypothesized in their paper. Furthermore, it should be noted that the measured filament lifetimes of NaOA/C_8TAB solutions at $c_s \geq c_{s,max}$ are lower than the theoretical values calculated from the zero shear viscosity assuming Newtonian flow behavior. This may indicate a flow-induced decrease of the mean length of the micelles.

Finally, distinguishing between linear and branched micelles based on CaBER measurements seems to be possible but is not unambiguous. In general, the micellar structure can change during flow (e.g. EIS formation as observed for CTAB/NaSal solutions for $R < R_{max}$ or breakage of micelles most likely to occur in NaOA/C_8TAB solutions for $c_s > c_{s,max}$).

5.4.7 Flow induced structure build-up

As discussed above, the phenomenon of elongation-induced structure (EIS) formation is suggested by the high λ_e/λ_s ratios observed for 25 mM CTAB/NaSal solutions at low salt/surfactant ratios R. In order to shed more light on EIS we have investigated CTAB/NaSal

and CPyCl/NaSal solutions with lower surfactant concentration again covering a broad R range. In figure 5.8 we compare the filament lifetime t_{fil} obtained in our CaBER experiment to the theoretical filament lifetime $t_{fil,N}$ calculated from the zero shear viscosity of the solutions assuming Newtonian flow behavior during capillary thinning. Introducing this value is necessary because shear relaxation time could not be determined for the low viscosity WLM solutions with low surfactant concentration, and therefore the relaxation time ratio λ_e/λ_s could not be calculated. The filament lifetime ratio $t_{fil}/t_{fil,N}$ is plotted as a function of R for CTAB/NaSal solutions with 5, 10 and 25 mM surfactant concentration as well as for CPyCl/NaSal with $R = 1$ and CTAB/NaSal with $R = 0.5$ as a function of surfactant concentration c_s.
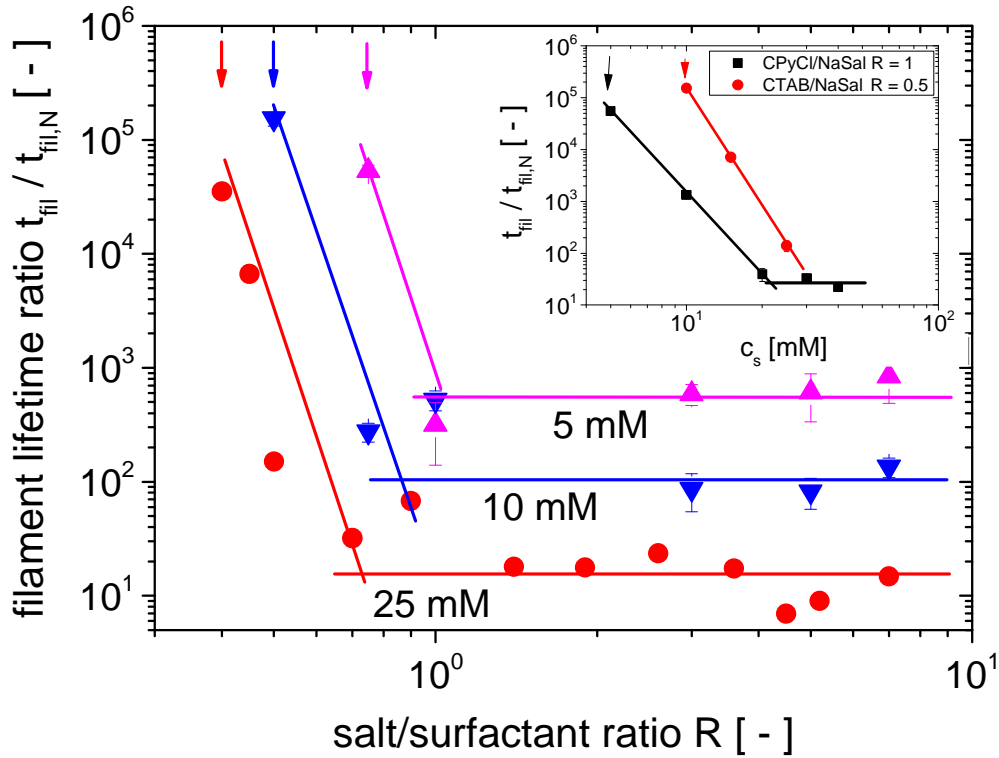
Figure 5.8: Filament lifetime ratio $t_{fil}/t_{fil,N}$ as a function of the salt surfactant ratio R for CTAB/NaSal solutions with surfactant concentrations of 5 mM, 10 mM, and 25mM at $T = 20°$C. The insert shows $t_{fil}/t_{fil,N}$ as a function of the surfactant concentration for CPyCl/NaSal solutions with $R = 1$ and CTAB/NaSal solutions with $R = 0.5$. The arrows indicate the critical R value at a given concentration or a critical surfactant concentration at a given R value, respectively, above which EIS are observed. Lines are to guide the eye.

For all surfactant systems, the filament lifetime ratio starts at high values of $t_{fil}/t_{fil,N} \approx 10^5$ but strongly decreases with increasing salt/surfactant ratio R and levels off at a constant

value for $R > R_{max}$. Similar results are obtained for CPyCl/NaSal solutions with $R = 1$ but different surfactant concentrations as illustrated in the insert of figure 5.8. For the 25 mM CTAB/NaSal solution this limiting $t_{fil}/t_{fil,N}$ ratio is around 10 and corresponds to $\lambda_e/\lambda_s \approx 1$ (see figure 5.5). As already discussed above filament thinning in this case is controlled by the viscoelasticity of the entangled WLM network present at rest. In all other cases, filament lifetime ratios $t_{fil}/t_{fil,N}$ between 10^2 and 10^5 are found indicating structure formation due to the elongational deformation during capillary thinning. This hypothesis is supported by the fact that all these solutions also show shear thickening and are prone to shear-induced structure (SIS) formation. It should be noted that performing multiple CaBER experiments on one and the same sample did not result in systematic variations in the filament lifetime confirming that the flow-induced structure formation is reversible. For a sake of clarity, we also want to note that the solutions investigated by Okawara and Takahashi [Okawara et al. 2008, 2009; Takahashi and Sakata 2011] do not show EIS in CaBER.
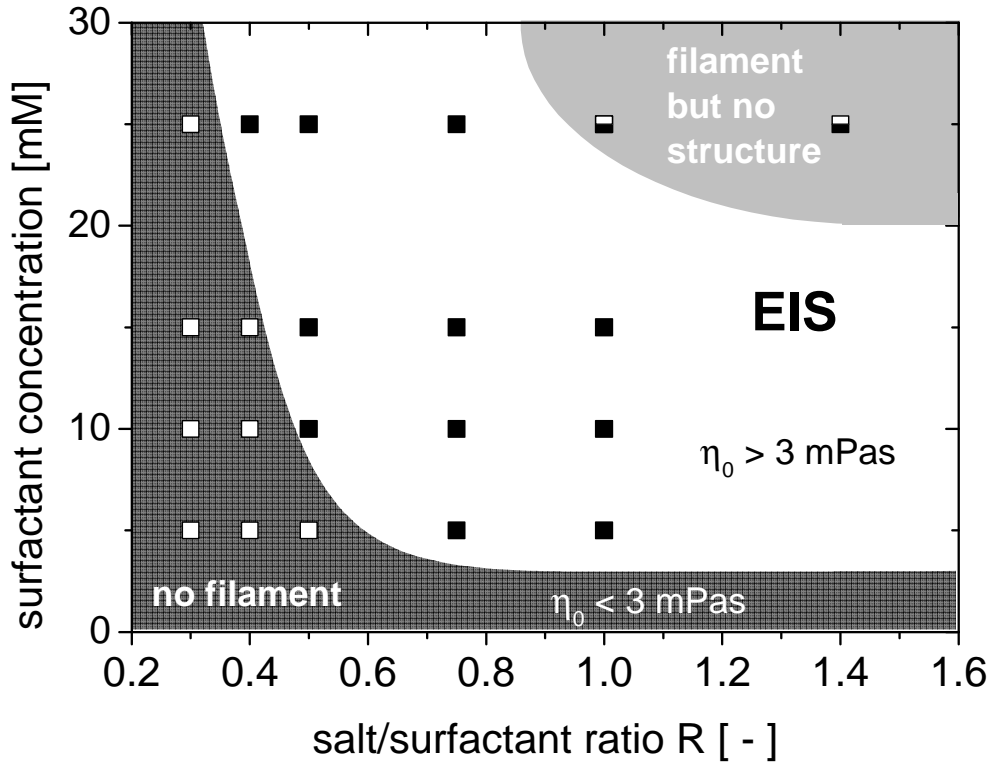
Figure 5.9: Illustration of filament creation in CaBER experiments depending on the salt/surfactant ratio R and the surfactant concentration for CTAB/NaSal solutions at $T = 20°$C. The dark gray area represents solutions where no filaments are created corresponding to zero shear viscosities $\eta_0 < 3$ mPas. The light gray area (half filled symbols) represents solutions where filaments are created but filament lifetime is controlled by the equilibrium viscoelasticity of the solutions and not by EIS formation. Filled symbols indicate solutions where EIS is found.

However, finding structure formation in shear experiments does not automatically imply a corresponding effect during capillary thinning. Figure 5.9 illustrates the occurrence of EIS during capillary thinning of CTAB/NaSal solutions exemplarily. For low salt/surfactant ratios R, no filaments could be created in CaBER experiments indicating that no structural change occurs during the stretching process. Furthermore, no structure formation is observed for high surfactant concentrations cs at high R values. In this case the filament lifetime is only controlled by the viscoelasticity of the WLM solutions as already discussed above. It should be noted that for all solutions in the 'no filament' and 'EIS' region in figure 5.9 a structure formation has been found in shear experiments. The critical salt/surfactant ratio crit R at which EIS is observed (indicated by slowly thinning filaments), decreases with increasing surfactant concentration and corresponds to a critical zero shear viscosity of about 3 mPas. If the viscosity of the WLM solution is too low, the initial liquid bridge

breaks during the initial step strain deformation. This minimum viscosity criterion also holds if the surfactant concentration is too low, irrespective of R. Nevertheless, these solutions show shear thickening. This discrepancy may be rationalized assuming that a minimum energy input is needed for structure formation. While this energy input cannot take place during the fast stepstrain deformation in a CaBER experiment it may be maintained in large deformation shear experiments. Finally, similar results have been obtained for CPyCl/NaSal solutions but a slightly lower critical zero shear viscosity of 2.2 mPas is found in this case.
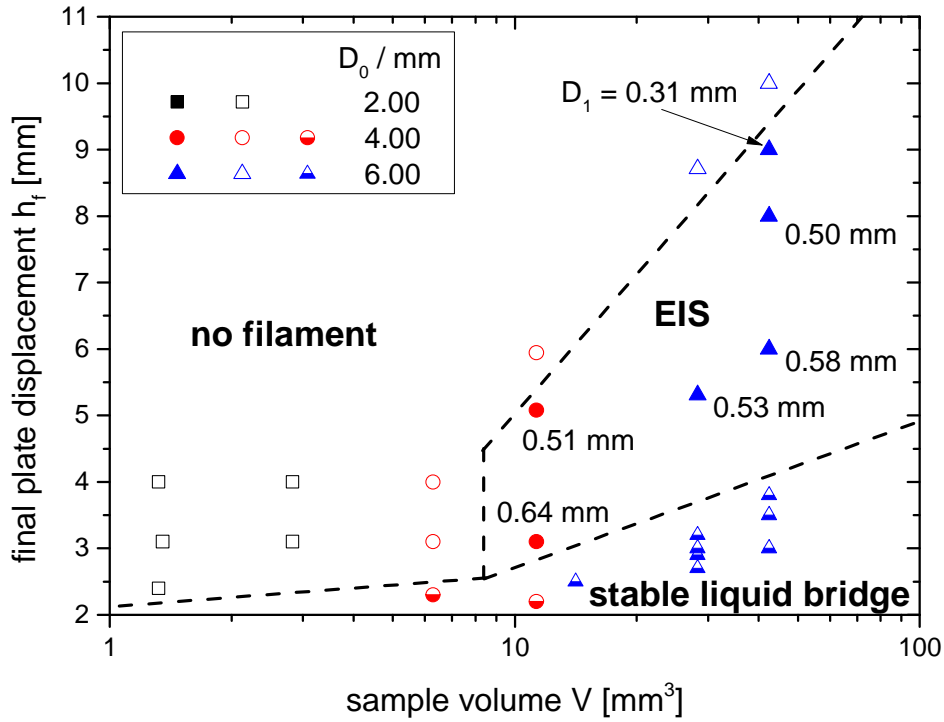
Figure 5.10: Influence of final plate displacement h_f and sample volume V on filament creation for a 10 mM CTAB/NaSal solution with $R = 0.5$ for three different plate diameters D_0 at $T = 20°C$. The sample volume V is set by the plate diameter D_0 and the plate displacement h_i and thus characterizes the initial configuration of the CaBER experiment.

The influence of the final plate displacement h_f and the sample volume V on structure formation in a CaBER experiment is illustrated exemplarily in figure 5.10 for a 10 mM CTAB/NaSal solution with $R = 0.5$. Generally, stable liquid bridges are observed for low final plate displacements. The minimum h_f needed for destabilization of the liquid bridge (followed by a thinning process) depends on surface tension and density of the solution but not on its viscosity or elasticity. Neglecting slight differences in solution density, critical h_f

values are independent of sample composition. However, if the final height h_f is sufficiently large two cases of filament breakup are observed. For low sample volume V (corresponding to low initial gap height h_i and small plate diameter D_0) the liquid bridge breaks during the initial step strain and no filament is created independent of the final plate separations h_f. This indicates that the thinning behavior is mainly controlled by the low zero shear viscosity and no structure build-up takes place. Increasing V but holding the final displacement h_f constant results in a dramatic increase of the filament lifetime indicating a structure build-up (EIS). Furthermore, for given initial sample volume (e.g. $V = 42$ mm^3 , corresponding to $D_0 = 6$ mm and $h_i = 1.5$ mm) the EIS phenomenon disappears if a critical $h_{f,c}$ value is exceeded. However, $h_{f,c}$ increases with increasing surfactant concentration, i.e. increasing solution viscosity, and the 'no filament' region in the $h_f - V$-plane disappears e.g. for a 25 mM CTAB/NaSal solution with $R = 0.5$.

The influence of the final displacement h_f , the sample volume V, and the zero shear viscosity η_0 of the surfactant solution might be summarized in the filament diameter D_1 measured right after the upper plate has reached the end position at $t = t_s$. This value increases with increasing sample viscosity (see for example data in [Clasen 2010]) and increasing V but decreases with increasing h_f. Our experimental results suggest that a minimum diameter $D_{1,crit}$ is needed for structure build-up of surfactant solutions in CaBER experiments. Values of $D_{1,crit} \approx 0.3$ mm are observed for a 10 mM CTAB/NaSal solution with $R = 0.5$ (figure 5.10) but $D_{1,crit}$ decreases slightly with increasing concentration ($D_{1,crit} \approx 0.26$ mm for 15 mM CTAB/NaSal, $R = 0.5$). This finding is supported by shear experiments using parallel plate geometry [Herle et al. 2005] where the increase of viscosity due to a structure build-up is less pronounced if the gap width is decreased.

Further insight into the EIS phenomenon is provided by FISER experiments. In these experiments the fluid drop is placed between two plates and the plates are separated at an exponentially increasing speed in order to maintain a constant elongation rate $\dot{\varepsilon}$. CTAB/NaSal solutions with surfactant concentrations between 5 mM and 20 mM and R values between 0.7 and 1 have been investigated at nominal elongation rates between 0.1 s^{-1} and 1 s^{-1}. Characteristic results for a $c_s = 10$ mM and $R = 0.75$ are shown in figure 5.11 displaying the filament diameter D as a function of total strain $\varepsilon_L(t) = \ln(L(t)/L_0)$ for different strain rates.

The $D(\varepsilon_L)$ curves can be split into three parts. In the first period D decreases from its initial value $D_0 \approx 5$ mm to $D_0 \approx 2.2$ mm corresponding to the stretching of the liquid filament which still forms a stable bridge. The second stage is characterized by a rapid filament thinning. Finally, regime III is reached at a critical nominal strain $\varepsilon_{L,c} = 1.1 \pm 0.1$. In this regime the slope of the $D(\varepsilon_L)$-curves dramatically decreases and this is attributed to

the elongation-induced structure build-up. In these FISER experiments structure formation always occurs at $\varepsilon_{L,c} \approx 1$ for all surfactant concentrations and R values investigated here irrespective of the applied nominal strain rate.
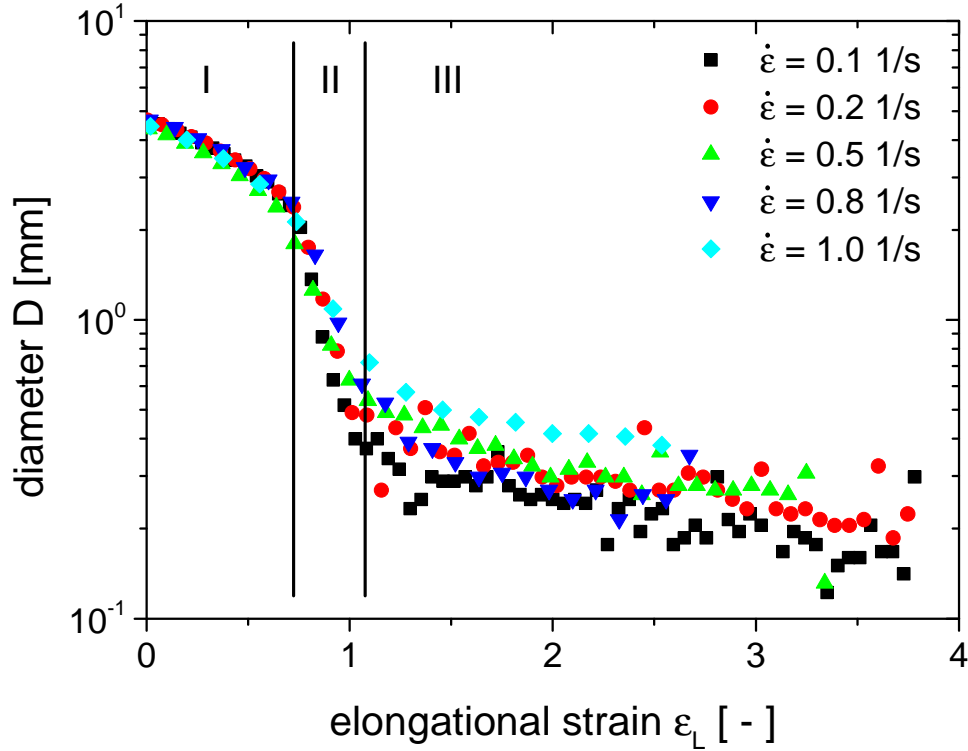
Figure 5.11: Diameter as a function of total elongational strain ε_L determined in FiSER experiments with an initial plate displacement $L_0 = 0.75$ mm for a CTAB/NaSal solution with $c_s = 10$ mM and $R = 0.75$ at $T = 25 \pm 3°C$.

Figure 5.12 shows two snapshots of a FiSER experiment performed at a constant elongation rate of $\dot{\varepsilon}_L = 0.4$ for a 10 mM CTAB/NaSal solution with $R = 1$. At the beginning (figure 5.12 left), a liquid reservoir is clearly visible at the lower plate. Further stretching yields only a slight decrease in the diameter but liquid is pulled out of the reservoir creating the new filament. This reveals the high stability of the filament and further supports the flow-induced structure build-up. Finally, the filament breaks at a finite diameter but not necessarily in the middle of the filament demonstrating the sensitivity of the structure to huge deformations presumably due to local fluctuations of structural strength.
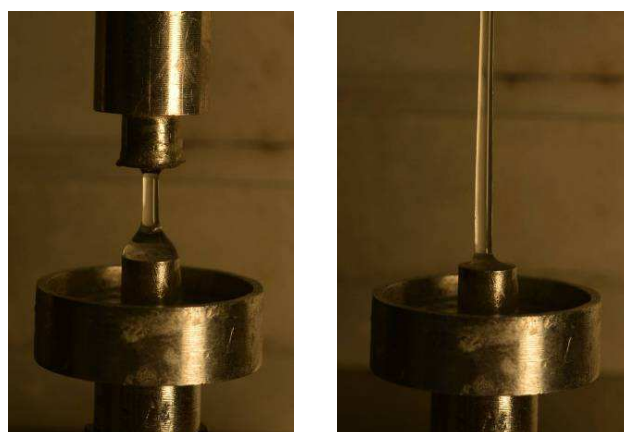
Figure 5.12: Snapshots of a stretched liquid filament consisting of a 10 mM CTAB/NaSal solution with $R = 1$ captured at the beginning and near the end of the third region in filament stretching performed using a FiSER apparatus at a constant elongational rate $\dot{\varepsilon}_L = 0.4$.

5.5 Conclusion

We have investigated the capillary thinning of six different wormlike micelles systems (CPyCl/ NaSal, CPyCl/NaSal/NaCl, CTAB/NaSal, CTAB/KBr, CTAB/NaNO$_3$, and CTAB/NaClO$_3$) covering a wide range of surfactant concentrations c_s and salt/surfactant ratios R.
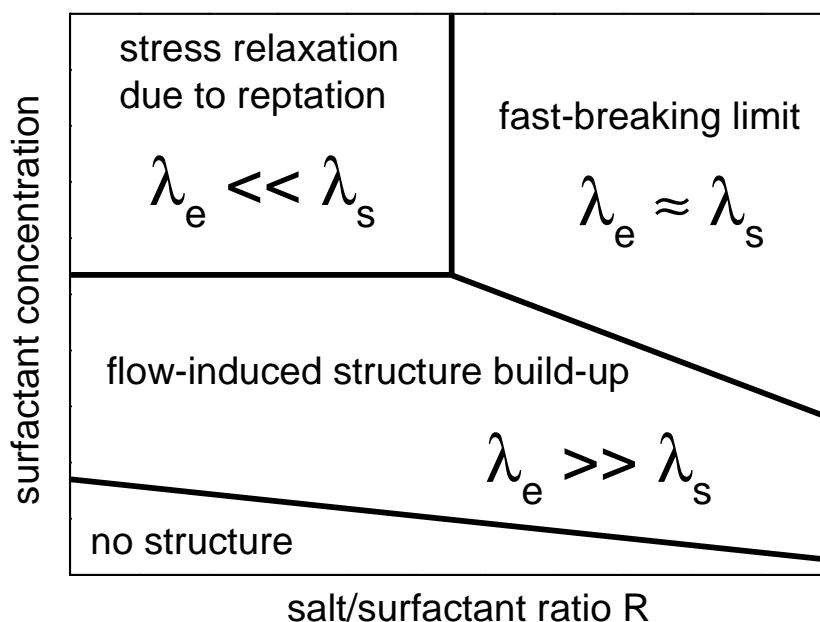
Figure 5.13: Schematic phase diagram for WLM solutions with different surfactant concentration and salt/surfactant ratios.

Figure 5.13 schematically summarizes the main results of our investigations on these WLM solutions.

Solutions in which stress relaxation is dominated by reptation (high c_s, low R) exhibit relaxation time ratios $\lambda_e/\lambda_s < 1$ similar to solutions of covalently bound polymer solutions. This is most likely due to stretching and orientation of the micelles in the strong non-linear flow during capillary thinning, but further structural investigations are needed to check for additional contributions from chain scission.

In the fast-breaking limit where micelles break and recombine quickly (high c_s, high R) $\lambda_e/\lambda_s \approx 1$ is found. Non-linear effects seem to be of minor relevance and the timescale of capillary thinning is solely controlled by linear material parameters available from small amplitude oscillatory shear. All investigated WLM solutions covering several orders of magnitude in shear modulus G_0 and micellar breakage time λ_{br} are found to obey a universal scaling law $t_{fil}/G_0 \propto \lambda_{br}^{3/2}$ even if $\lambda_e/\lambda_s < 1$. These findings indicate that the equilibrium mean length of the micelles does not change during capillary thinning.

Furthermore, CaBER experiments reveal a distinct difference between solutions of linear and branched micelles. The dependence of filament lifetime on zero shear viscosity is much stronger for linear micelles ($t_{fil} \propto \eta_0^{1.3}$) than for branched micelles ($t_{fil} \propto \eta_0^{0.9}$) and at a given zero shear viscosity branched micellar solutions exhibit a longer filament lifetime in CaBER experiments than solutions of linear micelles.

At lower surfactant concentrations filament lifetime is much larger than expected from the corresponding zero shear viscosity, $t_{fil} >> t_{fil,N}$, and relaxation time ratios $\lambda_e/\lambda_s > 1$ are observed. These findings are attributed to an elongation-induced structure (EIS) formation and all solutions categorized to show EIS also exhibit shear-induced structure (SIS) build-up. Nevertheless, a minimum zero shear viscosity η_0 and a minimum initial filament diameter D_1 are required to achieve such extended filament lifetimes in CaBER experiments indicating EIS. Additionally, FiSER experiments suggest that a minimum total strain $\varepsilon_{L,c}$ is needed for structure build-up in extensional flow. Further investigations will have to include birefringence, turbidity and scattering experiments to verify the EIS phenomenon directly and to get a deeper insight into the potentially formed super-micellar structure.

5.6 Acknowledgments

6 Summary

This thesis presents an experimental study on capillary thinning and eleongational rheology of polymer and wormlike micelles (WLM) solutions based on Capillary Breakup Extensional Rheometry (CaBER) including vertical and horizontal stretching of filaments. The CaBER technique allows for characterization of the uniaxial elongational behavior of low-viscosity fluids. Therefore, the self controlled thinning of an instable liquid bridge (previously created by an initial step strain) is analyzed. Characteristic elongational fluid properties are mostly determined from the diameter decay of the fluid filament.
The results of this thesis are related to three topics:

1. determination of the axial force and the true elongational viscosity,

2. elongational behavior of (mostly) entangled polystyrene (PS) and polyethylene oxide (PEO) solutions at different temperatures and solvent viscosities, and

3. elongational behavior of wormlike micelles solutions (CPyCl/NaSal, CPyCl/NaSal/NaCl, CTAB/NaSal, CTAB/KBr, CTAB/NaNO$_3$, CTAB/NaClO$_3$)[1] covering a broad range of surfactant concentrations and salt/surfactant ratios.

In order to determine the elongational behavior at elevated temperatures a self constructed temperature control unit has been developed allowing for a precise temperature adjustment between 5 °C and 90 °C with an accuracy of 0.2 °C.

A new way of performing CaBER experiments has been introduced in this thesis. This so called tilted CaBER method comprises a horizontal stretching of fluid filaments and a analysis of the gravity-driven bending of the liquid thread. Applying chain bending theory allows for a determination of the true axial force F in the liquid bridge in a range of $F = 0.1 - 1,000 \, \mu N$. For the first time, the true elongational viscosity has been determined from CaBER experiments without additional assumptions or specific constitutive equations only

---

[1]CPyCl: cetylpyridinium chlorid, NaSal: sodium salicylate, NaCl: sodium chloride, CTAB: hexadecyltrimethylammonium bromide, KBr: potassium bromide, NaNO$_3$: sodium nitrate, NaClO$_3$: sodium chlorate

analyzing video images of the thinning thread.

Commonly, data evaluation including the calculation of the elongational viscosity is based on the $\sigma_{zz} = 0$ assumption yielding an apparent axial force $F_{app} = \pi D \Gamma$ which is only given by the surface tension Γ. However, the true axial force F in the filament measured with the tilted CaBER method has revealed that this widely accepted assumption is not fulfilled in general during capillary thinning. Deviations of the $\sigma_{zz} = 0$ assumption have been discussed in terms of the force ratio $X = F/F_{app}$.

For Newtonian fructose solutions and silicon oil mixtures in a viscosity range of $0.9 - 60$ Pas, a compressive axial normal stresses $(\sigma_{zz}/|\sigma_{rr}| < 0)$ has been observed during linear diameter decay confirming Papageorgiou's [Papageorgiou 1995] solution for the force ratio $(X_\infty = 0.713)$ derived in case of negligible inertia.

The transient force ratio $X(t)$ for viscoelastic solutions decays exponentially in the first period of thinning and levels off at a value of $\tilde{X}$ depending on polymer concentration and initial elasto-capillary number Ec_0.

The initial stress decay after step strain filament formation is characterized by a relaxation time λ_X equal to the relaxation time λ_e determined from the terminal exponential thinning region indicating that the initial stress decay is controlled by the same molecular relaxation process as the strain hardening observed in the terminal regime of filament thinning.

Measurements on viscoelastic polyethylene oxide (PEO) solutions with high elasto-capillary numbers Ec_0 as well as concentrations $c > c^*$ (critical overlap concentration) but $c < 2c_e$ (c_e: entanglement concentration) has shown that no axial normal stresses $(\sigma_{zz}/|\sigma_{rr}| = 0)$ are present for these solutions during exponential diameter decay indicated by $\tilde{X} = X_\infty = 1$. In contrast, a positive axial normal stress $(\sigma_{zz}/|\sigma_{rr}| > 0,\ X_\infty > 1)$ has been detected for concentrations above the entanglement concentration $(c > c_e)$ during the whole thinning process. Furthermore, the final value of the force ratio X_∞ increases with increasing PEO concentration and no exponential diameter decay can be observed for these solutions.

However, for the PS and CPyCl/NaSal/NaCl solutions with $\mathrm{Ec}_0 \leq 1$ an intermediate Newtonian thinning regime (as already suggested by Clasen [Clasen 2010]) with compressive axial normal stress $(\sigma_{zz}/|\sigma_{rr}| < 0)$ has been confirmed based on the measured force ratio $\tilde{X} = 0.713$ prior to the viscoelastic thinning indicated by exponential diameter decay and $X_\infty = 1$.

Deviations from the $\sigma_{zz} = 0$ assumption $(X \neq 1)$ cause a difference between the apparent and true elongational viscosity η_e and $\eta_{e,app}$. Therefore apparent values, calculated from the diameter decay, have to be corrected by the factor $(2X - 1)$. Since η_e goes through a distinct minimum during filament thinning a characteristic minimum Trouton ratio Tr_{min} can be determined accurately. But it should be noted that the elongational rate during

capillary thinning is not constant as soon as deviations from the exponential diameter decay occur. This Trouton ratio decreases exponentially with increasing polymer concentration for all investigated solutions and levels off at $Tr_{min} \approx 10$ for all PEO solutions irrespective of solvent viscosity. For the PS and CPyCl/NaSal/NaCl solutions exhibiting intermediate Newtonian thinning and characterized by low elasto-capillary numbers $Tr_{min} = 3$ has been found. Furthermore, it could be shown that differences between elongational viscosities determined with CaBER and filament stretching extensional rheometer (FiSER) observed for WLM solutions (e.g. [Bhardwaj et al. 2007a]) cannot be related to the axial force ($X_\infty = 1$) and are more likely due to differences in strain history and failure mechanism.

The elongational relaxation time λ_e increases with increasing polymer concentration. But corresponding relaxation time ratios λ_e/λ_s, where λ_s is the terminal shear relaxation time determined in small amplitude oscillatory shear experiments, decrease exponentially with increasing polymer concentration and the data for all investigated solutions collapse onto a master curve irrespective of temperature, polymer molecular weight, or solvent viscosity when plotted versus the reduced concentration $c[\eta]$, with $[\eta]$ being the intrinsic viscosity. This has confirmed the strong effect of the non-linear deformation in CaBER experiments on entangled polymer solutions as suggested earlier [Arnolds et al. 2010].

In the third (probably most important) part of this dissertation the first systematic investigation of the uniaxial elongation behavior of wormlike micelles (WLM) solutions is presented. Six different systems (CPyCl/NaSal, CPyCl/NaSal/NaCl, CTAB/NaSal, CTAB/KBr, CTAB/NaNO$_3$, and CTAB/NaClO$_3$) have been investigated covering a broad range of surfactant concentrations c_s and salt/surfactant ratios R. The main results are schematically summarized in figure 6.1.

Solutions in which stress relaxation is dominated by reptation (high c_s, low R) exhibit relaxation time ratios $\lambda_e/\lambda_s < 1$ similar to solutions of covalently bound polymer solutions. This is most likely due to stretching and orientation of the micelles in the strong non-linear flow during capillary thinning, but further structural investigations are needed to check for additional contributions from chain scission.

In the fast-breaking limit (high c_s, low R) where micelles break and recombine quickly relaxation time ratios $\lambda_e/\lambda_s \approx 1$ have been found in contrast to the observations for covalently bound polymer solutions. Non-linear effects seem to be of minor relevance and the timescale of capillary thinning is solely controlled by linear material parameters available from small amplitude oscillatory shear. The investigated WLM solutions cover several orders of magnitude in shear modulus G_0 and micellar breakage time λ_{br}. Corresponding filament lifetimes t_{fil} have been found to obey a universal scaling law $t_{fil}/G_0 \propto \lambda_{br}^{3/2}$ even if $\lambda_e/\lambda_s < 1$ (min-
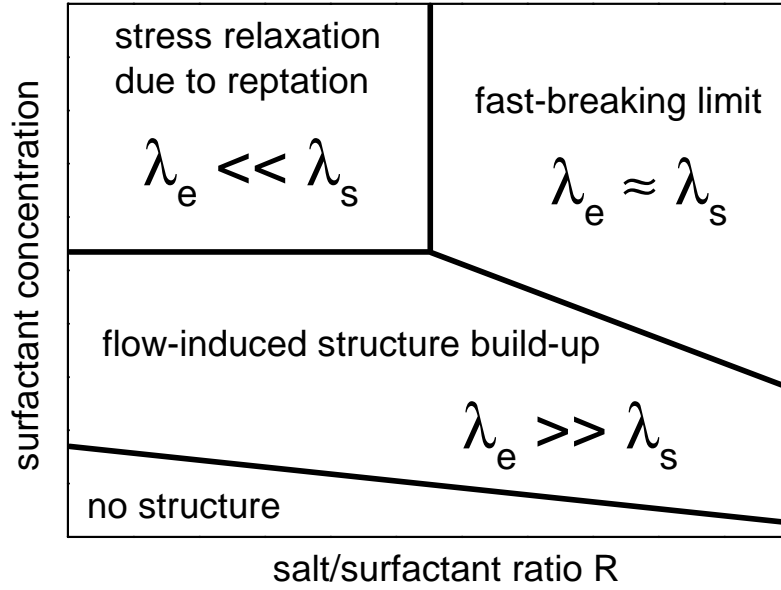
Figure 6.1: schematic phase diagram for WLM solutions with different surfactant concentration and salt/surfactant ratios.

imum in G" required). This indicates that the equilibrium mean length $\overline{L}$ of the micelles does not change during capillary thinning.

Furthermore, CaBER experiments have revealed a distinct difference between solutions of linear and branched micelles. The dependence of filament lifetime on zero shear viscosity is much stronger for linear micelles ($t_{fil} \propto \eta_0^{1.3}$) than for branched micelles ($t_{fil} \propto \eta_0^{0.9}$) and at a given zero shear viscosity η_0 branched micellar solutions exhibit a longer filament lifetime t_{fil} in CaBER experiments than solutions of linear micelles. This results may suggest that CaBER is a versatile means to distinguish between these structures.

At lower surfactant concentrations filament lifetimes t_{fil} are much larger than expected from the low zero shear viscosity, $t_{fil} \gg t_{fil,N}$, and relaxation time ratios $\lambda_e/\lambda_s > 1$ have been observed irrespective of the salt/surfactant ratio R. These findings have been attributed to a formation of elongation induced structures (EIS) and all solutions categorized to show EIS also exhibit shear induced structure (SIS) build-up. Nevertheless, a minimum zero shear viscosity η_0 and a minimum initial filament diameter D_1 are required to achieve such extended filament lifetimes in CaBER experiments indicating EIS. Additionally, filament stretching (FiSER) experiments suggest that a minimum total strain $\varepsilon_{L,c}$ is needed for structure build-up in extensional flow. Further investigations will have to include birefringence, turbidity and scattering experiments to verify the EIS phenomenon directly and to get a deeper insight into the potentially formed super-micellar structure.

7 Outlook

7.1 Tilted filament stretching measurements

Preliminarily measurements suggest that the tilted CaBER method can also be applied during the filament stretching process in order to calculate the true elongational viscosity. Figure 7.1 shows the diameter D as a function of time t for a liquid thread consisting of silicon
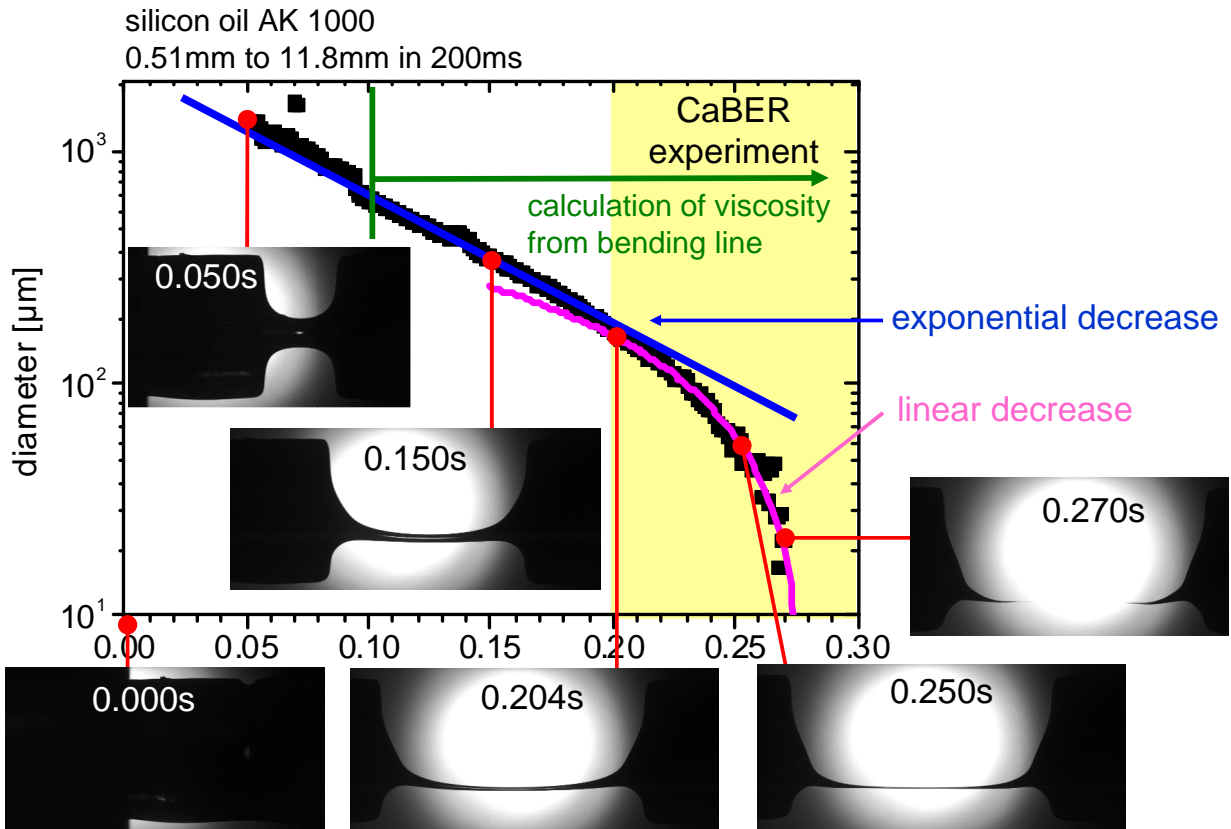
Figure 7.1: Diameter D as a function om time t for silicon oil AK 1000.

oil AK 1000. The strike time has been increased from its standard value of $t_s = 40$ ms to $t_s = 200$ ms. During the stretching process, $t < 200$ ms, the diameter decreases exponentially, whereas the characteristic linear diameter decay of a Newtonian liquid is observed after the plate has reached the end position. The deflection of the liquid thread is sufficiently large for

times $t > 100$ ms allowing for the determination of the true axial force in the filament. For these times, a Trouton ratio of Tr = 3.1±0.1 is observed indicating that the force calculation based on horizontally stretched filaments yields reasonable values not only during capillary thinning but also during filament stretching.

In fact, the transfer of the tilted CaBER method to continuous filament stretching could be an easy way to determine the true elongational viscosity of low viscous liquids while imposing a well defined elongational flow field without an initial step strain treatment. The application to other Newtonian liquids with different zero shear viscosity as well as to non-Newtonian liquids such as polymer or wormlike micelles solutions is not evaluated jet, but corresponding experiments could give a deeper insight into the elongational behavior of such solutions.

7.2 Direct force measurement

The tilted CaBER method cannot be used for determination of axial forces for solutions with pronounced non-cylindrical filaments, e.g. yield stress fluids. In such cases, the force has to be determined directly using a force transducer covering the range from 1 - 1,000 ţN.
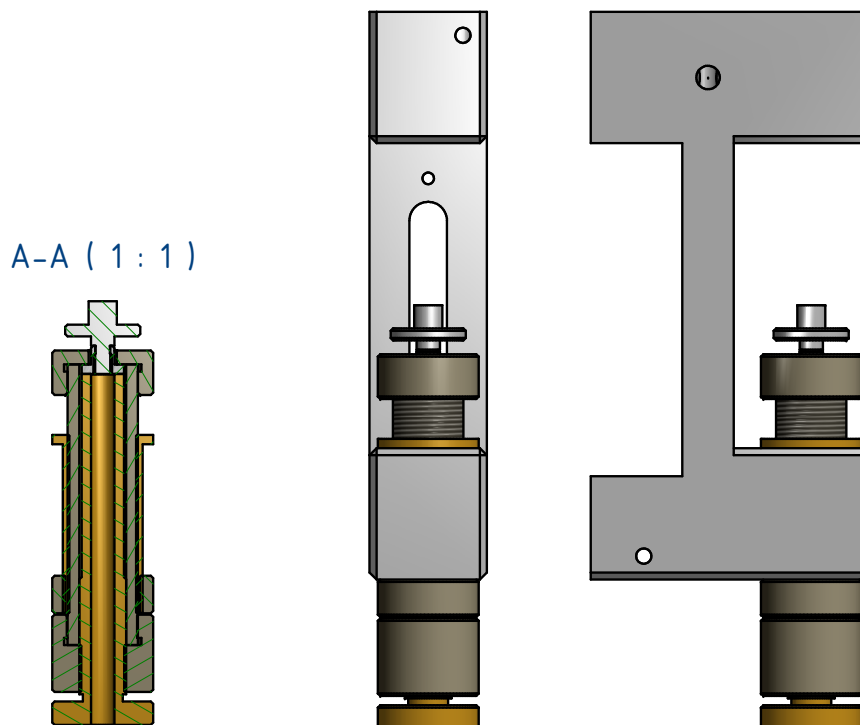
Figure 7.2: Self constructed force transducer. The lower plated will be mounted on a disk spring and the displacement of the spring will be measured with a highly sensitive laser interferometer.

Transducers showing a good handling during the filling process as well as during the measurement including the initial step strain treatment are not sensitive enough to determine the axial force over the whole thinning process until the filament breaks [Klein et al. 2009]. High sensitive force transducers e.g. FT-S270 and FT-S540 (FemtoTools GmbH) might be able to determine the axial force between 2 μN and 2000 μN and 0.3 μN and 180 μN respectively but cannot stand high mechanical forces present during sample filling or initial step strain. Therefore, using commercial force transducers seems to be unsuitable for an application with CaBER.

Figure 7.2 shows a draft of a home made force transducer. Here, the lower plate will be mounted on a disc spring. The weight of the liquid droplet ensures that the spring is always compressed during the experiment. The displacement of the spring can be detected easily with a highly sensitive laser interferometer allowing for a contactless measurement. Commercially available interferometer systems can achieve a resolution up to 40 pm. The true axial force can then be calculated from the deflection of the spring due to the linear relation between force and displacement. The main benefit of this method is that such springs are very cheap and can be replaced quickly, if necessary. However, the calculation of the true axial force during capillary thinning using a force transducer depends crucially on the determination of the we ight of the fluid droplet placed at the lower plate because the measured force signal is the difference of the weight force and the axial force (obviously assumed to be tensile) in the filament.

7.3 Optical investigations

The formation of an elongation induced structure (EIS) of low concentrated CPyCl/NaSal and CTAB/NaSal solutions dramatically increases the filament stability in CaBER experiments. Further investigations on EIS should be based on direct structural investigations e.g. using small angle light and neutron scattering (SALS, SANS) as well as turbidity and birefringence measurements in order to understand the huge variations in filament life time upon variation of surfactant concentration at salt/surfactant ratio R.

A strongly increasing turbidity would directly evidence structure build-up. First analysis of high resolution video images captured with a microscope objective do not show turbid regions in fluid filaments of WLM solutions during capillary thinning. However, using a laser setup including a high sensitivity light detector should give better results [Talbott and Goddard 1979; Rothstein 2003; Sattler et al. 2007]. Further optical investigates like birefringence measurements would provide information about flow alignment of WLM and give some information of the validity of the stress optical rule (SOR) for WLM solutions.

Since light scattering experiments during filament thinning in CaBER are not feasible due to light refraction on the curvature of the liquid thread a hyperbolic flow channel, e.g. similar to the one used by the Rothstein group [Chellamuthu et al. 2009], seems to be suitable for such investigations. The hyperbolic contraction would produce a nearly uniform extensional flow along the center-line. Using different flow rates would allow for the realization of different elongational rates between $\dot{\varepsilon} = 1 \ldots 100\mathrm{s}^{-1}$. Furthermore, a contraction form 50 mm to a final down-stream width of 0.3 mm would correspond to a Hencky strain of approximately $\varepsilon \approx 5$. Therefore, structural changes could be studied as a function of elongation rate (different flow rates) and accumulated Hencky strain (different positions along the center-line). Potential differences in structure formation during planar and uniaxial extension could be evaluated based on turbidity and birefringence measurements, which can also performed on slender liquid filaments up to a minimum diameter of about 100 μm [Talbott and Goddard 1979; Rothstein 2003; Sattler et al. 2007].

Furthermore, the elongational viscosity of solutions where the SOR holds true could also be determined in a hyperbolic flow channel using a special optical elongational rheometer [Schuberth and Munstedt 2008b,a]. This technique combines the laser-Doppler velocimetry (LDV) and the two color flow-induced birefringence (FIB) method to measure the true elongational viscosity. The flow profile obtained using LDV allows for a calculation of the elongation rate. FIB provides the corresponding tensile stress required to calculate the elongational viscosity η_e, but only if the SOR is valid and can be accurately determined for the fluid under consideration.

It has to be kept in mind that for SANS measurement the minimum cross-section of the neutron beam is around 2 mm x 2 mm in order to get good scattering results within reasonable time. Accordingly, SANS experiments could be performed only up to $\varepsilon = 3$.

First preliminary SANS measurements have been performed at the SANS 1 beamline of the Paul Scherrer Institute (PSI, Villingen, CH) for a 10 mM CTAB solution with R = 0.5 in equilibrium conditions. Experimental results are shown in figure 7.3. The wormlike chain model of Pedersen and Schurtenberger [Pedersen and Schurtenberger 1996] (method 3. without excluded volume effects) has been used for determining the mean length $\overline{L}$ of the micelles (best fit of experimental data to the model is shown in figure 7.3 represented by the solid line). Measurements values of about $\overline{L} = 52.5$ nm are in good agreement with literature data [Garg et al. 2006].

Assuming that elongational flow just induces an increase in average micellar length $\overline{L}$, a 1000fold increase in filament lifetime would correspond to a 10fold increase in $\overline{L}$ (according to the Cates model [Cates and Candau 1990]) and thus could be observed in SANS experiments which are suitable for quantitative structural characterization on a length scale

of 1 nm to 100 nm. In addition, small angle light scattering (SALS) $(0.3 < q < 4\mu\mathrm{m}^{-1})$ measurements should be used to probe larger structures of about 250 nm to 3300 nm.
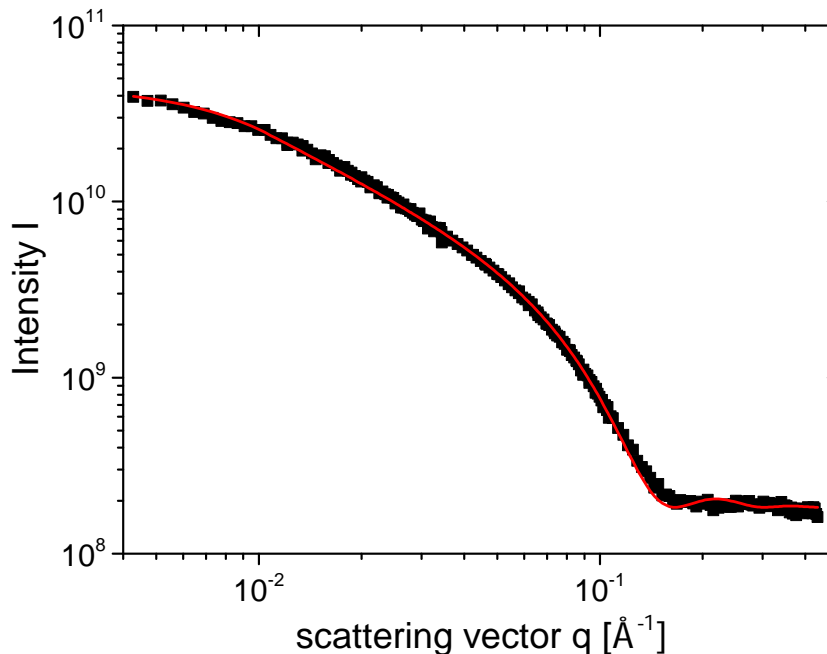
Figure 7.3: Intensity I as a function of the scattering vector q for a 10 mM CTAB/NaSal solution with R = 0.5. The line represents the best fit of the wormlike chain model of Pedersen and Schurtenberger [Pedersen and Schurtenberger 1996] (method 3. without excluded volume effects) to experimental data.

7.4 Further issues

The effect of direction of gravity, solvent viscosity, and temperature on the relaxation time ratio λ_s/λ_e has been evaluated in this study but the effect of surface tension Γ on λ_s/λ_e remains uninvestigated. From a theoretical point of view, the elongation rate $\dot{\varepsilon}$ is related to the elongation relaxation time λ_e (equation 1.8). Since the surface tension Γ is the driving force for capillary thinning, its influence on the elongational relaxation time should be checked experimentally. Therefore, aqueous polymer solutions should be stretched in an oil bath thus allowing for a substantial variation of the interfacial tension and hence $\dot{\varepsilon}$ by an order of magnitude.

An another interesting aspect is the thinning behavior of shear thinning fluids without having elastic effects. Viscoelastic fluids as investigated in this thesis show shear thinning and elastic effects (e.g. shear and elongational relaxation times) at the same time. However, it is

not totally clear which effects are related to the elasticity of the solutions and which effects are caused by a change in viscosity due to an increased deformation rate. Dispersions of non-spherical particles, e.g. glass fibers, in a Newtonian liquid should show a shear thinning due to the orientation of the particles in the flow field but no pronounced elastic effects should be present. Such measurements would give a deeper insight into the thinning behavior of shear thinning liquids. However, special attention has to be taken to prevent sedimentation of the particles. Therefore, the viscosity of the primary Newtonian phase should be chosen sufficiently high to suppress sedimentation during the experiment.

Bibliography

Abezgauz, L., R. O. and Danino, D. (2007). Department of biotechnology and food engineering, technion, haifa, israel. european colloid and interface society, geneva.

Agarwal, S. and Gupta, R. (2002). An innovative extensional viscometer for low-viscosity and low-elasticity liquids. *Rheologica Acta*, 41:456–460.

Alexandrou, A., Entov, V., Bazilevsky, A., Rozhkov, A., and Sharaf, A. (2009). On the tensile testing of viscoplastic fluids. *Acta rheological, special issue following the workshop: viscoplastic fluids: from theory to application.*

Anna, S. and McKinley, G. (2001). Elasto-capillary thinning and breakup of model elastic liquids. *Journal of Rheology*, 45(1):115–138.

Anna, S., Rogers, C., and GH, M. (1999). On controlling the kinematics of a filament stretching rheometer using a real-time active control mechanism. *Journal of Non-Newton Fluid Mechanics*, 87:307–335.

Anna, S. L., McKinley, G. H., Nguyen, D. A., Sridhar, T., Muller, S. J., Huang, J., and James, D. F. (2001). An interlaboratory comparison of measurements from filament-stretching rheometers using common test fluids. *Journal of Rheology*, 45(1):83–114.

Appell, J., Porte, G., Khatory, A., Kern, F., and Candau, S. J. (1992). Static and dynamic properties of a network of wormlike surfactant micelles (cetylpyridinium chlorate in sodium-chlorate brine). *Journal De Physique Ii*, 2(5):1045–1052.

Arnolds, O. (2011). *Dehnrheologie verdünnter, halbkonzentrierter und konzentrierter Polymerlösungen untersucht mit Capillary Breakup Extensional Rheometry (CaBER)*. PhD thesis, Karlsruher Institut für Technologie (KIT).

Arnolds, O., Buggisch, H., Sachsenheimer, D., and Willenbacher, N. (2010). Capillary breakup extensional rheometry (caber) on semi-dilute and concentrated polyethyleneoxide (peo) solutions. *Rheologica Acta*, 49:1207–1217.

Bibliography

Arora, K., Sureshkumar, R., Scheiner, M. P., and Piper, J. L. (2002). Surfactant-induced effects on turbulent swirling flows. *Rheologica Acta*, 41(1-2):25–34.

Arratia, P., Cramer, L., Gollub, J., and Durian, D. (2009). The effects of polymer molecular weight on filament thinning and drop breakup in microchannels. *New Journal of Physics*, 11:115006.

Azzouzi, H., Decruppe, J. P., Lerouge, S., and Greffier, O. (2005). Temporal oscillations of the shear stress and scattered light in a shear-banding-shear-thickening micellar solution. *European Physical Journal E*, 17(4):507–514.

Bach, A., Rasmussen, H., and Hassager, O. (2003). Extensional viscosity for polymer melts measured in the filament stretching rheometer. *Journal of Rheology*, 47:429–441.

Bazilevskii, V., Entov, M., Lerner, M., and Rozhkov, N. (1997). *Failure of polymer solution filaments*, volume 39. Springer, Heidelberg, Germany.

Bazilevsky, A., Entov, V., and Rozhkov, A. (2001). Breakup of an oldroyd liquid bridge as a method for testing the rheological properties of polymer solutions. *Polym Sci Ser A*, 43:716–726.

Bazilevsky, A. V., Entov, V. M., and Rozhkov, A. N. (1990). Liquid filament microrheometer and some of its applications. *Proceedings of the Third European Rheology Conference*, pages 41–43.

Beaumont, J., Louvet, N., Divoux, T., Fardin, M. A., Bodiguel, H., Lerouge, S., Manneville, S., and Colin, A. (2013). Turbulent flows in highly elastic wormlike micelles. *Soft Matter*, 9(3):735–749.

Becerra, M. and Carvalho, M. S. (2011). Stability of viscoelastic liquid curtain. *Chemical Engineering and Processing: Process Intensification*, 50:445–449.

Berret, J. F., Appell, J., and Porte, G. (1993). Linear rheology of entangled wormlike micelles. *Langmuir*, 9(11):2851–2854.

Berret, J. F., Gamez-Corrales, R., Oberdisse, J., Walker, L. M., and Lindner, P. (1998). Flow-structure relationship of shear-thickening surfactant solutions. *Europhysics Letters*, 41(6):677–682.

Berret, J. F., Lerouge, S., and Decruppe, J. P. (2002). Kinetics of the shear-thickening transition observed in dilute surfactant solutions and investigated by flow birefringence. *Langmuir*, 18(20):7279–7286.

Berret, J. F. and Serero, Y. (2001). Evidence of shear-induced fluid fracture in telechelic polymer networks. *Physical Review Letters*, 87(4).

Bhardwaj, A., Miller, E., and Rothstein, J. P. (2007a). Filament stretching and capillary breakup extensional rheometry measurements of viscoelastic wormlike micelle solutions. *Journal of Rheology*, 51(4):693–719.

Bhardwaj, A., Miller, E., and Rothstein, J. P. (2007b). Filament stretching and capillary breakup extensional rheometry measurements of viscoelastic wormlike micelle solutions. *Journal of Rheology*, 51(4):693–719.

Bhardwaj, A., Richter, D., Chellamuthu, M., and Rothstein, J. (2007c). The effect of pre-shear on the extensional rheology of wormlike micelle solutions. *Rheologica Acta*, 46:861–875.

Böhme, G. (2000). *Strömungsmechanik nichtnewtonscher Fluide*. B. G. Teubner, Stuttgart.

Binding, D. (1991). Further considerations of axisymmetric contraction flows. *Journal of Non-Newtonian Fluid Mechanics*, 41(1-2):27 – 42.

Bischoff White, E., Chellamuthu, M., and Rothstein, J. (2010). Extensional rheology of a shear-thickening cornstarch and water suspension. *Rheologica Acta*, 49:119–129.

Boger, D. V. (1987). Viscoelastic flows through contractions. *Annual Review of Fluid Mechanics*, 19(1):157–182.

Boltenhagen, P., Hu, Y. T., Matthys, E. F., and Pine, D. J. (1997). Observation of bulk phase separation and coexistence in a sheared micellar solution. *Physical Review Letters*, 79(12):2359–2362.

Braun, D. and Rosen, M. (2000). *Rheology modifiers handbook Ů practical use and application*. William Andrew Publishing, Norwich, US.

Brenner, M. P., Lister, J. R., and Stone, H. A. (1996). Pinching threads, singularities and the number 0.0304... *Physics of Fluids*, 8(11):2827–2836.

Britton, M. M. and Callaghan, P. T. (1997). Two-phase shear band structures at uniform stress. *Physical Review Letters*, 78(26):4930–4933.

Britton, M. M. and Callaghan, P. T. (1999). Shear banding instability in wormlike micellar solutions. *European Physical Journal B*, 7(2):237–249.

Bibliography

Callaghan, P. T., Cates, M. E., Rofe, C. J., and Smeulders, J. (1996). A study of the "spurt effect" in wormlike micelles using nuclear magnetic resonance microscopy. *Journal De Physique Ii*, 6(3):375–393.

Campo-Deaño, L. and Clasen, C. (2010). The slow retraction method (srm) for the determination of ultra-short relaxation times in capillary breakup extensional rheometry experiments. *Journal of Non-Newtonian Fluid Mechanics*, 165(23-24):1688–1699.

Candau, S. J., Khatory, A., Lequeux, F., and Kern, F. (1993). Rheological behavior of wormlike micelles - effect of salt content. *Journal De Physique Iv*, 3(C1):197–209.

Cappelaere, E., Cressely, R., Makhloufi, R., and Decruppe, J. P. (1994). Temperature and flow-induced viscosity transitions for ctab surfactant solutions. *Rheologica Acta*, 33(5):431–437.

Cates, M. E. (1987). Reptation of living polymers - dynamics of entangled polymers in the presence of reversible chain-scission reactions. *Macromolecules*, 20(9):2289–2296.

Cates, M. E. (1988). Dynamics of living polymers and flexible surfactant micelles - scaling laws for dilution. *Journal De Physique*, 49(9):1593–1600.

Cates, M. E. (1996). Flow behaviour of entangled surfactant micelles. *Journal of Physics: Condensed Matter*, 8:9167–9176.

Cates, M. E. and Candau, S. J. (1990). Statics and dynamics of worm-like surfactant micelles. *Journal of Physics-Condensed Matter*, 2(33):6869–6892.

Chan, R., Gupta, R., and Sridhar, T. (1988). Fiber spinning of very dilute solutions of polyacrylamide in water. *Journal of Non-Newtonian Fluid Mechanics*, 30(2-3):267–283.

Chao, K. K., Child, C. A., Grens, E. A., and Williams, M. C. (1984). Antimisting action of polymeric additives in jet fuels. *Aiche Journal*, 30(1):111–120.

Chellamuthu, M., Arndt, E. M., and Rothstein, J. P. (2009). Extensional rheology of shear-thickening nanoparticle suspensions. *Soft Matter*, 5(10):2117–2124.

Chellamuthu, M. and Rothstein, J. P. (2008). Distinguishing between linear and branched wormlike micelle solutions using extensional rheology measurements. *Journal of Rheology*, 52(3):865–884.

Chen, C. M. and Warr, G. G. (1997). Light scattering from wormlike micelles in an elongational field. *Langmuir*, 13(6):1374–1376.

116

Chen, L., Bromberg, L., Hatton, T. A., and Rutledge, G. C. (2008). Electrospun cellulose acetate fibers containing chlorhexidine as a bactericide. *Polymer*, 49(5):1266–1275.

Christanti, Y. and Walker, L. M. (2001a). Surface tension driven jet break up of strain-hardening polymer solutions. *Journal of Non-Newtonian Fluid Mechanics*, 100(1-3):9–26.

Christanti, Y. and Walker, L. M. (2001b). Surface tension driven jet break up of strain-hardening polymer solutions. *Journal of Non-Newtonian Fluid Mechanics*, 100(1-3):9–26.

Christanti, Y. and Walker, L. M. (2002a). Effect of fluid relaxation time of dilute polymer solutions on jet breakup due to a forced disturbance. *Journal of Rheology*, 46(3):733–748.

Christanti, Y. and Walker, L. M. (2002b). Effect of fluid relaxation time of dilute polymer solutions on jet breakup due to a forced disturbance. *Journal of Rheology*, 46(3):733–748.

Clasen, C. (2010). Capillary breakup extensional rheometry of semi-dilute polymer solutions. *Korea-Australia Rheology Journal*, 22(4):331–338.

Clasen, C., Eggers, j., Fontelos, M. A., Li, J., and McKinley, G. H. (2006a). The beads-on-string structure of viscoelastic threads. *Journal of Fluid Mechanics*, 556:283–308.

Clasen, C., Plog, J. P., Kulicke, W.-M., Owens, M., Macosko, C., Scriven, L. E., Verani, M., and McKinley, G. H. (2006b). How dilute are dilute solutions in extensional flows? *Journal of Rheology*, 50(6):849–881.

Crassous, J. J., Regisser, R., Ballauff, M., and Willenbacher, N. (2005). Characterization of the viscoelastic behavior of complex fluids using the piezoelastic axial vibrator. *Journal of Rheology*, 49(4):851–863.

Cressely, R. and Hartmann, V. (1998). Rheological behaviour and shear thickening exhibited by aqueous ctab micellar solutions. *European Physical Journal B*, 6(1):57–62.

Croce, V., Cosgrove, T., Maitland, G., Hughes, T., and Karlsson, G. (2003). Rheology, cryogenic transmission electron spectroscopy, and small-angle neutron scattering of highly viscoelastic wormlike micellar solutions. *Langmuir*, 19(20):8536–8541.

Cromer, M., Cook, L. P., and McKinley, G. H. (2009). Extensional flow of wormlike micellar solutions. *Chemical Engineering Science*, 64(22):4588–4596.

Danino, D. (2012). Cryo-tem of soft molecular assemblies. *Current Opinion in Colloid & Interface Science*, 17(6):316–329.

Bibliography

Danino, D., Bernheim-Groswasser, A., and Talmon, Y. (2001). Digital cryogenic transmission electron microscopy: an advanced tool for direct imaging of complex fluids. *Colloids and Surfaces a-Physicochemical and Engineering Aspects*, 183:113–122.

Danino, D., Talmon, Y., and Zana, R. (2000). Cryo-tem of thread-like micelles: on-the-grid microstructural transformations induced during specimen preparation. *Colloids and Surfaces a-Physicochemical and Engineering Aspects*, 169(1-3):67–73.

David, R. A., Wei, M.-H., and Kornfield, J. A. (2009). Effects of pairwise, donor-acceptor functional groups on polymer solubility, solution viscosity and mist control. *Polymer*, 50(26):6323–6330.

Decruppe, J. P. and Ponton, A. (2003). Flow birefringence, stress optical rule and rheology of four micellar solutions with the same low shear viscosity. *European Physical Journal E*, 10(3):201–207.

Dehmoune, J., Decruppe, J.-P., Greffier, O., and Xu, H. (2007). Rheometric and rheo-optical investigation on the effect of the aliphatic chain length of the surfactant on the shear thickening of dilute worm-like micellar solutions. *Rheologica Acta*, 46(8):1121–1129.

Dehmoune, J., Decruppe, J. P., Greffier, O., Xu, H., and Lindner, P. (2009). Shear thickening in three surfactants of the alkyl family c(n)tab: Small angle neutron scattering and rheological study. *Langmuir*, 25(13):7271–7278.

Dexter, R. W. (1996). Measurement of extensional viscosity of polymer solutions and its effects on atomization from a spray nozzle. *Atomization and Sprays*, 6(2):167–191.

Dontula, P., Pasquali, M., Scriven, L. E., and Macosko, C. W. (1997). Can extensional viscosity be measured with opposed nozzle devices? *Rheologica Acta*, 36(4):429–448.

Drye, T. J. and Cates, M. E. (1992). Living networks - the role of cross-links in entangled surfactant solutions. *Journal of Chemical Physics*, 96(2):1367–1375.

Dunlap, P. and Leal, L. (1987). Dilute polystyrene solutions in extensional flows: Birefringence and flow modification. *Journal of Non-Newtonian Fluid Mechanics*, 23(0):5 – 48.

Eggers, J. (1993). Universal pinching of 3d axisymmetric free-surface flow. *Phys. Rev. Lett.*, 71:3458–3460.

118

Eggers, J. (1997). Nonlinear dynamics and breakup of free-surface flows. *Rev. Mod. Phys.*, 69:865–930.

Entov, V. and Hinch, E. (1997). Effect of a spectrum of relaxation times on the capillary thinning of a filament of elastic liquid. *Journal of Non-Newtonian Fluid Mechanics*, 72(1):31–53.

Erni, P., Varagnat, M., Clasen, C., Crest, J., and McKinley, G. H. (2011). Microrheometry of sub-nanolitre biopolymer samples: non-newtonian flow phenomena of carnivorous plant mucilage. *Soft Matter*, 7(22):10889–10898.

Fardin, M. A., Divoux, T., Guedeau-Boudeville, M. A., Buchet-Maulien, I., Browaeys, J., McKinley, G. H., Manneville, S., and Lerouge, S. (2012a). Shear-banding in surfactant wormlike micelles: elastic instabilities and wall slip. *Soft Matter*, 8(8):2535–2553.

Fardin, M. A. and Lerouge, S. (2012). Instabilities in wormlike micelle systems from shear-banding to elastic turbulence. *European Physical Journal E*, 35(9).

Fardin, M. A., Ober, T. J., Gay, C., Gregoire, G., McKinley, G. H., and Lerouge, S. (2011). Criterion for purely elastic taylor-couette instability in the flows of shear-banding fluids. *Epl*, 96(4).

Fardin, M. A., Ober, T. J., Grenard, V., Divoux, T., Manneville, S., McKinley, G. H., and Lerouge, S. (2012b). Interplay between elastic instabilities and shear-banding: three categories of taylor-couette flows and beyond. *Soft Matter*, 8(39):10072–10089.

Fernando, R., Xing, L., and Glass, J. (2000). Rheology parameters controlling spray atomization and roll misting behavior of waterborne coatings. *Progress in Organic Coatings*, 40(1-4):35–38.

Fernando, R. H., Lundberg, D. J., and Glass, J. E. (1989). *Importance of Elongational Flows in the Performance of Water-Borne Formulations*, chapter 13, pages 245–259. American Chemical Society.

Fischer, E. and Callaghan, P. T. (2001). Shear banding and the isotropic-to-nematic transition in wormlike micelles. *Physical Review E*, 64(1).

Fischer, P., Fuller, G. G., and Lin, Z. C. (1997). Branched viscoelastic surfactant solutions and their response to elongational flow. *Rheologica Acta*, 36(6):632–638.

Bibliography

Fischer, P. and Rehage, H. (1997). Non-linear flow properties of viscoelastic surfactant solutions. *Rheologica Acta*, 36(1):13–27.

Fischer, P., Wheeler, E. K., and Fuller, G. G. (2002). Shear-banding structure orientated in the vorticity direction observed for equimolar micellar solution. *Rheologica Acta*, 41(1-2):35–44.

Fuller, G. and Leal, L. (1980). Flow birefringence of dilute polymer solutions in two-dimensional flows. *Rheologica Acta*, 19(5):580–600.

Fuller, G. G., Cathey, C. A., Hubbard, B., and Zebrowski, B. E. (1987). Extensional viscosity measurements for low-viscosity fluids. *Journal of Rheology (1978-present)*, 31(3):235–249.

Galvan-Miyoshi, J., Delgado, J., and Castillo, R. (2008). Diffusing wave spectroscopy in maxwellian fluids. *European Physical Journal E*, 26(4):369–377.

Garg, G., Hassan, P. A., and Kulshreshtha, S. K. (2006). Dynamic light scattering studies of rod-like micelles in dilute and semi-dilute regime. *Colloids and Surfaces a-Physicochemical and Engineering Aspects*, 275(1-3):161–167.

Germann, N., Cook, L. P., and Beris, A. N. (2013). Nonequilibrium thermodynamic modeling of the structure and rheology of concentrated wormlike micellar solutions. *Journal of Non-Newtonian Fluid Mechanics*, 196:51–57.

Gier, S. and Wagner, C. (2012). Visualization of the flow profile inside a thinning filament during capillary breakup of a polymer solution via particle image velocimetry and particle tracking velocimetry. *Physics of Fluids*, 24(5).

Goldin, M., Pfeffer, R., and Shinnar, R. (1972). Break-up of a capillary jet of a non-newtonian fluid having a yield stress. *The Chemical Engineering Journal*, 4(1):8–20.

Granek, R. and Cates, M. E. (1992). Stress-relaxation in living polymers - results from a poisson renewal model. *Journal of Chemical Physics*, 96(6):4758–4767.

Groß, D., Hauger, W., and Wriggers, P. (2004). *Technische Mechanik Band 4: Hydromechanik, Elemente der höheren Mechanik und Numerische Methoden*. Springer, Heidelberg, Germany.

Hadri, F. and Guillou, S. (2010). Drag reduction by surfactant in closed turbulent flow. *International Journal of Engineering Science and Technology*, 2(12):6876–6879.

Han, L., Gupta, R., Doraiswamy, D., and Palmer, M. (2004). Effect of liquid rheology on jetting of polymer solutions. In *XIVth International Congress on Rheology*, Seoul, KR.

Hartmann, V. and Cressely, R. (1997a). Influence of sodium salicylate on the rheological behaviour of an aqueous ctab solution. *Colloids and Surfaces a-Physicochemical and Engineering Aspects*, 121(2-3):151–162.

Hartmann, V. and Cressely, R. (1997b). Shear thickening of an aqueous micellar solution of cetyltrimethylammonium bromide and sodium tosylate. *Journal De Physique Ii*, 7(8):1087–1098.

Hartmann, V. and Cressely, R. (1997c). Simple salts effects on the characteristics of the shear thickening exhibited by an aqueous micellar solution of ctab/nasa1. *Europhysics Letters*, 40(6):691–696.

Hartmann, V. and Cressely, R. (1998). Occurrence of shear thickening in aqueous micellar solutions of ctab with some added organic counterions. *Colloid and Polymer Science*, 276(2):169–175.

Haward, S. J. and McKinley, G. H. (2012). Stagnation point flow of wormlike micellar solutions in a microfluidic cross-slot device: Effects of surfactant concentration and ionic environment. *Physical Review E*, 85(3).

Haward, S. J., Ober, T. J., Oliveira, M. S. N., Alves, M. A., and McKinley, G. H. (2012a). Extensional rheology and elastic instabilities of a wormlike micellar solution in a microfluidic cross-slot device. *Soft Matter*, 8(2):536–555.

Haward, S. J., Sharma, V., Butts, C. P., McKinley, G. H., and Rahatekar, S. S. (2012b). Shear and extensional rheology of cellulose/ionic liquid solutions. *Biomacromolecules*, 13(5):1688–1699.

Helgeson, M. E., Hodgdon, T. K., Kaler, E. W., and Wagner, N. J. (2010). A systematic study of equilibrium structure, thermodynamics, and rheology of aqueous ctab/nano3 wormlike micelles. *Journal of Colloid and Interface Science*, 349(1):1–12.

Herle, V., Fischer, P., and Windhab, E. J. (2005). Stress driven shear bands and the effect of confinement on their structures - a rheological, flow visualization, and rheo-sals study. *Langmuir*, 21(20):9051–9057.

Herle, V., Kohlbrecher, J., Pfister, B., Fischer, P., and Windhab, E. J. (2007). Alternating vorticity bands in a solution of wormlike micelles. *Physical Review Letters*, 99(15).

Bibliography

Hofmann, S., Rauscher, A., and Hoffmann, H. (1991). Shear induced micellar structures. *Berichte Der Bunsen-Gesellschaft-Physical Chemistry Chemical Physics*, 95(2):153–164.

Hu, Y., Rajaram, C. V., Wang, S. Q., and Jamieson, A. M. (1994). Shear thickening behavior of a rheopectic micellar solution - salt effects. *Langmuir*, 10(1):80–85.

Hu, Y. T., Boltenhagen, P., Matthys, E., and Pine, D. J. (1998). Shear thickening in low-concentration solutions of wormlike micelles. ii. slip, fracture, and stability of the shear-induced phase. *Journal of Rheology*, 42(5):1209–1226.

Hu, Y. T. and Matthys, E. F. (1995). Characterization of micellar structure dynamics for a drag-reducing surfactant solution under shear - normal stress studies and flow geometry-effects. *Rheologica Acta*, 34(5):450–460.

Humbert, C. and Decruppe, J. P. (1998). Stress optical coefficient of viscoelastic solutions of cetyltrimethylammonium bromide and potassium bromide. *Colloid and Polymer Science*, 276(2):160–168.

Israelachvili, J. N., Mitchell, D. J., and Ninham, B. W. (1976). Theory of self-assembly of hydrocarbon amphiphiles into micelles and bilayers. *J. Chem. Soc., Faraday Trans. 2*, 72:1525–1568.

James, D., Yogachandran, N., and Roper, J. (2003). Fluid elasticity in extension, measured by a new technique, correlates with misting. In *8th TAPPI advanced coating fundamentals symposium*, pages 166–171, Chicago, US.

Kadoma, I. A. and van Egmond, J. W. (1998). Flow-induced nematic string phase in semidilute wormlike micelle solutions. *Physical Review Letters*, 80(25):5679–5682.

Kadoma, I. A., Ylitalo, C., and van Egmond, J. W. (1997). Structural transitions in wormlike micelles. *Rheologica Acta*, 36(1):1–12.

Kato, M., Takahashi, T., and Shirakashi, M. (2002). Steady planar elongational viscosity of ctab/nasal aqueous solutions measured in a 4-roll mill flow cell. *Journal of the Society of Rheology Japan*, 30(5):283–287.

Kato, M., Takahashi, T., and Shirakashi, M. (2004). Flow-induced structure change and flow instability of ctab/nasal aqueous solution in 4-roll mill flow cell. Seoul, Korea. International Congress on Rheology.

Kato, M., Takahashi, T., and Shirakashi, M. (2006). Influence of planar elongation strain on flow-induced structure and flow instability of ctab/nasal aqueous solution. *Transactions Japan Society Mech. Eng. Series B*, 72:1935–1942.

Kennedy, J. C., Meadows, J., and Williams, P. A. (1995). Shear and extensional viscosity characteristics of a series of hydrophobically associating polyelectrolytes. *Journal of the Chemical Society-Faraday Transactions*, 91(5):911–916.

Kern, F., Lequeux, F., Zana, R., and Candau, S. J. (1994). Dynamical properties of salt-free viscoelastic micellar solutions. *Langmuir*, 10(6):1714–1723.

Khatory, A., Kern, F., Lequeux, F., Appell, J., Porte, G., Morie, N., Ott, A., and Urbach, W. (1993). Entangled versus multiconnected network of wormlike micelles. *Langmuir*, 9(4):933–939.

Kheirandish, S., Gubaydullin, I., and Willenbacher, N. (2009). Shear and elongational flow behavior of acrylic thickener solutions. part ii: effect of gel content. *Rheologica Acta*, 48:397–407.

Kheirandish, S., Guybaidullin, I., Wohlleben, W., and Willenbacher, N. (2008). Shear and elongational flow behavior of acrylic thickener solutions. *Rheologica Acta*, 47:999–1013.

Kim, N. J., Pipe, C. J., Ahn, K. H., Lee, S. J., and McKinley, G. H. (2010). Capillary breakup extensional rheometry of a wormlike micellar solution. *Korea-Australia Rheology Journal*, 22(1):31–41.

Klein, C. O., Naue, I. F. C., Nijman, J., and Wilhelm, M. (2009). Addition of the force measurement capability to a commercially available extensional rheometer (caber). *Soft Materials*, 7(4):242–257.

Kolte, M., Rasmussen, H., and Hassager, O. (1997). Transient filament stretching rheometer ii: numerical simulation. *Rheologica Acta*, 36:285–302.

Kolte, M. I. and Szabo, P. (1999). Capillary thinning of polymeric filaments. *Journal of Rheology*, 43(3):609–625.

Larson, R. G. (1999). *The Structure and Rheology of Complex Fluids*. Oxford University Press, Oxford.

Lenczyk, J. P. and Kiser, K. M. (1971). Stability of vertical jets of non-newtonian fluids. *AIChE Journal*, 17(4):826–831.

Bibliography

Lequeux, F. (1992). Reptation of connected wormlike micelles. *Europhysics Letters*, 19(8):675–681.

Lerouge, S., Fardin, M. A., Argentina, M., Gregoire, G., and Cardoso, O. (2008). Interface dynamics in shear-banding flow of giant micelles. *Soft Matter*, 4(9):1808–1819.

Li, H. and Hao, J. (2008). Phase behavior and rheological properties of a salt-free catanionic surfactant ttaoh/la/h2o system. *Journal of Physical Chemistry B*, 112(34):10497–10508.

Liang, R. and Mackley, M. (1994). Rheological characterization of the time and strain dependence for polyisobutylene solutions. *Journal of Non-Newtonian Fluid Mechanics*, 52(3):387–405.

Liu, C. H. and Pine, D. J. (1996). Shear-induced gelation and fracture in micellar solutions. *Physical Review Letters*, 77(10):2121–2124.

Lu, B., Li, X., Scriven, L. E., Davis, H. T., Talmon, Y., and Zakin, J. L. (1998). Effect of chemical structure on viscoelasticity and extensional viscosity of drag-reducing cationic surfactant solutions. *Langmuir*, 14(1):8–16.

Lutz-Bueno, V., Kohlbrecher, J., and Fischer, P. (2013). Shear thickening, temporal shear oscillations, and degradation of dilute equimolar ctab/nasal wormlike solutions. *Rheologica Acta*, 52(4):297–312.

Ma, W., Chinesta, F., Tuladhar, T., and Mackley, M. (2008). Filament stretching of carbon nano tube suspension. *Rheologica Acta*, 47:447–457.

Macosko, C. (1994). *Rheology: principles, measurements, and applications*. Advances in interfacial engineering series. VCH.

Mahajan, M. P., Tsige, M., Taylor, P. L., and Rosenblatt, C. (1999). Stability of liquid crystalline bridges. *Physics of Fluids*, 11(2):491–493.

Mair, R. W. and Callaghan, P. T. (1997). Shear flow of wormlike micelles in pipe and cylindrical couette geometries as studied by nuclear magnetic resonance microscopy. *Journal of Rheology*, 41(4):901–924.

Martinie, L., Buggisch, H., and Willenbacher, N. (2013). Apparent elongational yield stress of soft matter. *Journal of Rheology*, 57(2):627–646.

Matta, J. and Tytus, R. (1990). Liquid stretching using a falling cylinder. *Journal of Non-Newtonian Fluid Mechanics*, 35(2-3):215 – 229.

124

McKay, G., Ferguson, J., and Hudson, N. (1978). Elongational flow and the wet spinning process. *Journal of Non-Newtonian Fluid Mechanics*, 4(1-2):89–98.

McKinley, G., Brauner, O., and Yao, M. (2001). Kinematics of filament stretching in dilute and concentrated polymer solutions. *Korea-Australia Rheology Journal*, 13:29–35.

McKinley, G. and Sridhar, T. (2002). Filament stretching rheometry of complex fluids. *Annual Review of Fluid Mechanics*, 34:375–415.

McKinley, G. H. (2005). Visco-elasto-capillary thinning and break-up of complex fluids. *Annual Rheology Reviews*, 5(4):1–48.

McKinley, G. H. and Tripathi, A. (2000). How to extract the newtonian viscosity from capillary breakup measurements in a filament rheometer. *Journal of Rheology*, 44(3):653–670.

Meadows, J., Williams, P. A., and Kennedy, J. C. (1995). Comparison of the extensional and shear viscosity characteristics of aqueous hydroxyethylcellulose solutions. *Macromolecules*, 28(8):2683–2692.

Miller, E., Clasen, C., and Rothstein, J. P. (2009). The effect of step-stretch parameters on capillary breakup extensional rheology (caber) measurements. *Rheologica Acta*, 48(6):625–639.

Münch, C., Hoffmann, H., Ibel, K., Kalus, J., Neubauer, G., Schmelzer, U., and Selbach, J. (1993). Transient small-angle neutron-scattering experiments on micellar solutions with a shear-induced structural transition. *Journal of Physical Chemistry*, 97(17):4514–4522.

Münstedt, H. (1975). Viscoelasticity of polystyrene melts in tensile creep experiments. *Rheologica Acta*, 14:1077–1088.

Münstedt, H. (1979). New universal extensional rheometer for polymer melts. *Journal of Rheology*, 23:421–436.

Münstedt, H., Kurzbeck, S., and Egersdörfer, L. (1998). Influence of molecular structure on rheological properties of polyethylenes part ii. elongational behavior. *Rheologica Acta*, 37:21–29.

Moan, M. and Magueur, A. (1988). Transient extensional viscosity of dilute flexible polymer solutions. *Journal of Non-Newtonian Fluid Mechanics*, 30(2-3):343 – 354.

Bibliography

Mohanty, S., Davis, H. T., and McCormick, A. V. (2001). Complementary use of simulations and free energy models for ctab/nasal systems. *Langmuir*, 17(22):7160–7171.

Morrison, F. A. (2001). *Understanding Rheology*. Oxford University Press, New York.

Muller, A. J., Torres, M. F., and Saez, A. E. (2004). Effect of the flow field on the rheological behavior of aqueous cetyltrimethylammonium p-toluenesulfonate solutions. *Langmuir*, 20(10):3838–3841.

Muller, R. and Froelich, D. (1985). New extensional rheometer for elongational viscosity and flow birefringence measurements: some results on polystyrene melts. *Polymer*, 26(10):1477 – 1482.

Nelson, W. C., Kavehpour, H. P., and Kim, C. J. (2011). A miniature capillary breakup extensional rheometer by electrostatically assisted generation of liquid filaments. *Lab on a Chip*, 11(14):2424–2431.

Nemoto, N., Kuwahara, M., Yao, M. L., and Osaki, K. (1995). Dynamic light-scattering of ctab/nasal thread-like micelles in a semidilute regime .3. dynamical coupling between concentration fluctuation and stress. *Langmuir*, 11(1):30–36.

Ng, S. L., Mun, R. P., Boger, D. V., and James, D. F. (1996). Extensional viscosity measurements of dilute solutions of various polymers. *Journal of Non-Newtonian Fluid Mechanics*, 65(2-3):291–298.

Niedzwiedz, K., Buggisch, H., and Willenbacher, N. (2010). Extensional rheology of concentrated emulsions as probed by capillary breakup elongational rheometry (caber). *Rheologica Acta*, 49(11):1103–1116.

Niedzwiedz, Katarzyna andArnolds, O., Willenbacher, N., and Brummer, R. (2009). How to characterize yield stress fluids with capillary breakup extensional rheometry (caber)? *Appl Rheol*, 19.

Nowak, M. (2001). Elastic properties of a dilute surfactant solution in the shear induced state. *Rheologica Acta*, 40(4):366–372.

Oda, R., Panizza, P., Schmutz, M., and Lequeux, F. (1997). Direct evidence of the shear-induced structure of wormlike micelles: Gemini surfactant 12-2-12. *Langmuir*, 13(24):6407–6412.

Oelschlaeger, C., Schopferer, A., Scheffold, F., and Willenbacher, N. (2009). Linear-to-branched micelles transition: A rheometry and diffusing wave spectroscopy (dws) study. *Langmuir*, 25(2):716–723.

Oelschlaeger, C., Suwita, P., and Willenbacher, N. (2010). Effect of counterion binding efficiency on structure and dynamics of wormlike micelles. *Langmuir*, 26(10):7045–7053.

Okawara, M., Hasegawa, T., Iino, Y., and Narumi, T. (2008). Experimental study on pressure loss of ctab/nasal aqueous solution through slots and a capillary. *Nihon Reoroji Gakkaishi*, 36:137–143.

Okawara, M., Hasegawa, T., Iino, Y., and Narumi, T. (2009). Experimental study of pressure loss and rheo-optical behavior of ctab/nasal aqueous solution under elongational flow. *Nihon Reoroji Gakkaishi*, 37:39–46.

Oliveira, M. S., Yeh, R., and McKinley, G. H. (2006). Iterated stretching, extensional rheology and formation of beads-on-a-string structures in polymer solutions. *Journal of Non-Newtonian Fluid Mechanics*, 137(1-3):137–148.

Orr, N. and Sridhar, T. (1999). Probing the dynamics of polymer solutions in extensional flow using step strain rate experiments. *Journal of Non-Newton Fluid Mechanics*, 82:203–232.

Ouchi, M., Takahashi, T., and Shirakashi, M. (2006a). Flow-induced structure change and flow-instability of ctab/nasal aqueous solution in a two-dimensional abrupt contraction channel. *Nihon Reoroji Gakkaishi*, 34(4):229–234.

Ouchi, M., Takahashi, T., and Shirakashi, M. (2006b). Shear-induced structure change and flow-instability in start-up couette flow of aqueous, wormlike micelle solution. *Journal of Rheology*, 50(3):341–352.

Padding, J. T. (2009). Efficient simulation of noncrossing fibers and chains in a hydrodynamic solvent. *Journal of Chemical Physics*, 130(14).

Papageorgiou, D. T. (1995). On the breakup of viscous liquid threads. *Physics of Fluids*, 7(7):1529–1544.

Pathak, J. A. and Hudson, S. D. (2006). Rheo-optics of equilibrium polymer solutions: Wormlike micelles in elongational flow in a microfluidic cross-slot. *Macromolecules*, 39(25):8782–8792.

Bibliography

Pedersen, J. S. and Schurtenberger, P. (1996). Scattering functions of semiflexible polymers with and without excluded volume effects. *Macromolecules*, 29(23):7602–7612.

Perge, C., Fardin, M. A., and Manneville, S. (2014). Surfactant micelles: Model systems for flow instabilities of complex fluids. *European Physical Journal E*, 37(4).

Plog, J. P., Kulicke, W. M., and Clasen, C. (2005). Influence of the molar mass distribution on the elongational behaviour of polymer solutions in capillary breakup. *Applied Rheology*, 15(1):28–37.

Pope, D. P. and Keller, A. (1977). Alignment of maeromolecules in solution by elongational flow; a study of the effect of pure shear in a four roll mill. *Colloid & Polymer Sci*, 255(7):633–643.

Porte, G., Gomati, R., Elhaitamy, O., Appell, J., and Marignan, J. (1986). Morphological transformations of the primary surfactant structures in brine-rich mixtures of ternary-systems (surfactant alcohol brine). *Journal of Physical Chemistry*, 90(22):5746–5751.

Prudhomme, R., Smith-Romanogli, V., and Dexter, R. (2005). Elongational viscosity effects in spraying processes. In *230th ACS national meeting*, Washington, US.

Prudhomme, R. K. and Warr, G. G. (1994). Elongational flow of solutions of rodlike micelles. *Langmuir*, 10(10):3419–3426.

Raghavan, S. R. and Kaler, E. W. (2001). Highly viscoelastic wormlike micellar solutions formed by cationic surfactants with long unsaturated tails. *Langmuir*, 17(2):300–306.

Rathfon, J. M., Cohn, R. W., Crosby, A. J., Rothstein, J. P., and Tew, G. N. (2011). Confinement effects on chain entanglement in free-standing polystyrene ultrathin films. *Macromolecules*, 44(13):5436–5442.

Regev, O., Vandebril, S., Zussman, E., and Clasen, C. (2010). The role of interfacial viscoelasticity in the stabilization of an electrospun jet. *Polymer*, 51(12):2611–2620.

Rehage, H. and Hoffmann, H. (1988). Rheological properties of viscoelastic surfactant systems. *The Journal of Physical Chemistry*, 92(16):4712–4719.

Rehage, H. and Hoffmann, H. (1991). Viscoelastic surfactant solutions - model systems for rheological research. *Molecular Physics*, 74(5):933–973.

Renardy, M. (1994). Some comments on the surface tension driven breakup (or the lack of it) of the viscoelastic jets. *Journal of Rheology*, 51:97–107.

Renardy, M. (1995). A numerical study of the asymptotic evolution and breakup of newtonian and viscoelastic jets. *Journal of Non-Newtonian Fluid Mechanics*, 59(2-3):267 – 282.

Rodd, L. E., Scott, T. P., Cooper-White, J. J., and McKinley, G. H. (2005). Capillary break-up rheometry of low-viscosity elastic fluids. *Applied Rheology*, 15(1):12–27.

Rothstein, J. P. (2003). Transient extensional rheology of wormlike micelle solutions. *Journal of Rheology*, 47(5):1227–1247.

Rothstein, J. P. and McKinley, G. H. (2002a). A comparison of the stress and birefringence growth of dilute, semi-dilute and concentrated polymer solutions in uniaxial extensional flows. *Journal of Non-Newtonian Fluid Mechanics*, 108(1-3):275–290.

Rothstein, J. P. and McKinley, G. H. (2002b). Inhomogeneous transient uniaxial extensional rheometry. *Journal of Rheology*, 46(6):1419–1443.

Rubinstein, M. and Colby, R. H. (2009). *Polymer physics*. Oxford Univ. Press, Oxford.

Sachsenheimer, D., Hochstein, B., Buggisch, H., and Willenbacher, N. (2012). Determination of axial forces during the capillary breakup of liquid filaments - the tilted caber method. *Rheologica Acta*, 51(10):909–923.

Sachsenheimer, D., Hochstein, B., and Willenbacher, N. (2014a). Experimental study on the capillary thinning of entangled polymer solutions. *Rheologica Acta*. accepted.

Sachsenheimer, D., Oelschlaeger, C., Müller, S., Bindgen, S., Küstner, J., and Willenbacher, N. (2014b). Elongational deformation of wormlike micellar solutions. journal of rheology. *Journal of Rheology*. submitted.

Salmon, J. B., Colin, A., Manneville, S., and Molino, F. (2003). Velocity profiles in shearbanding wormlike micelles. *Physical Review Letters*, 90(22).

Sankaran, A. K. and Rothstein, J. P. (2012). Effect of viscoelasticity on liquid transfer during gravure printing. *Journal of Non-Newtonian Fluid Mechanics*, 175:64–75.

Sattler, R., Gier, S., Eggers, J., and Wagner, C. (2012). The final stages of capillary break-up of polymer solutions. *Physics of Fluids*, 24(2).

Sattler, R., Kityk, A., and Wagner, C. (2007). Molecular configurations in the droplet detachment process of a complex liquid. *Physical Review E*, 75(5).

Bibliography

Schmitt, V., Lequeux, F., Pousse, A., and Roux, D. (1994). Flow behavior and shear-induced transition near an isotropic-nematic transition in equilibrium polymers. *Langmuir*, 10(3):955–961.

Schmitt, V., Schosseler, F., and Lequeux, F. (1995). Structure of salt-free wormlike micelles - signature by sans at rest and under shear. *Europhysics Letters*, 30(1):31–36.

Schümmer, P. and Tebel, K. (1983). A new elongational rheometer for polymer solutions. *Journal of Non-Newtonian Fluid Mechanics*, 12(3):331–347.

Schubert, B. A., Kaler, E. W., and Wagner, N. J. (2003). The microstructure and rheology of mixed cationic/anionic wormlike micelles. *Langmuir*, 19(10):4079–4089.

Schubert, B. A., Wagner, N. J., Kaler, E. W., and Raghavan, S. R. (2004). Shear-induced phase separation in solutions of wormlike micelles. *Langmuir*, 20(9):3564–3573.

Schuberth, S. and Munstedt, H. (2008a). Simultaneous measurements of velocity and stress distributions in polyisobutylenes using laser-doppler velocimetry and flow induced birefringence. *Rheologica Acta*, 47(1):111–119.

Schuberth, S. and Munstedt, H. (2008b). Transient elongational viscosities of aqueous polyacrylamide solutions measured with an optical rheometer. *Rheologica Acta*, 47(2):139–147.

Shikata, T., Hirata, H., and Kotaka, T. (1988). Micelle formation of detergent molecules in aqueous-media .2. role of free salicylate ions on viscoelastic properties of aqueous cetyltrimethylammonium bromide sodium-salicylate solutions. *Langmuir*, 4(2):354–359.

Solomon, M. J. and Muller, S. J. (1996). The transient extensional behavior of polystyrene-based boger fluids of varying solvent quality and molecular weight. *Journal of Rheology*, 40(5):837–856.

Spiegelberg, S. H., Ables, D. C., and McKinley, G. H. (1996). The role of end-effects on measurements of extensional viscosity in filament stretching rheometers. *Journal of Non-Newtonian Fluid Mechanics*, 64(2-3):229–267.

Sridhar, T., Tirtaatmadja, V., Nguyen, D., and Gupta, R. (1991). Measurement of extensional viscosity of polymer solutions. *Journal of Non-Newtonian Fluid Mechanics*, 40(3):271–280.

Stelter, M., Brenn, G., Yarin, A. L., Singh, R. P., and Durst, F. (2002). Investigation of the elongational behavior of polymer solutions by means of an elongational rheometer. *Journal of Rheology*, 46(2):507–527.

Takahashi, T. and Sakata, D. (2011). Flow-induced structure change of ctab/nasal aqueous solutions in step planar elongation flow. *Journal of Rheology*, 55(2):225–240.

Takahashi, T., Yako, N., and Shirakashi, M. (2001). Relationship between shear-induced structure and optical anisotropy on cpyci/nasai aqueous solution. *Nihon Reoroji Gakkaishi*, 29(1):27–32.

Talbott, W. and Goddard, J. (1979). Streaming birefringence in extensional flow of polymer solutions. *Rheologica Acta*, 18(4):505–517.

Tan, H., Tam, K., Tirtaatmadja, V., Jenkins, R., and Bassett, D. (2000). Extensional properties of model hydrophobically modified alkali-soluble associative (hase) polymer solutions. *Journal of Non-Newtonian Fluid Mechanics*, 92(2-3):167–185.

Tan, L., Pan, J., and Wan, A. (2012). Shear and extensional rheology of polyacrylonitrile solution: effect of ultrahigh molecular weight polyacrylonitrile. *Colloid Polym Sci*, 290:289–295.

Tembely, M., Vadillo, D., Mackley, M. R., and Soucemarianadin, A. (2012). The matching of a "one-dimensional" numerical simulation and experiment results for low viscosity newtonian and non-newtonian fluids during fast filament stretching and subsequent break-up. *Journal of Rheology*, 56(1):159–183.

Tirtaatmadja, V., McKinley, G. H., and Cooper-White, J. J. (2006). Drop formation and breakup of low viscosity elastic fluids: Effects of molecular weight and concentration. *Physics of Fluids*, 18(4):043101.

Tirtaatmadja, V. and Sridhar, T. (1993). A filament stretching device for measurement of extensional viscosity. *Journal of Rheology*, 37(6):1081–1102.

Tropea, C., editor (2007). *Springer handbook of experimental fluid mechanics*. Springer, Heidelberg.

Tuladhar, T. R. and Mackley, M. R. (2008). Filament stretching rheometry and break-up behaviour of low viscosity polymer solutions and inkjet fluids. *Journal of Non-Newtonian Fluid Mechanics*, 148(1-3):97–108.

Vadillo, D. C., Mathues, W., and Clasen, C. (2012). Microsecond relaxation processes in shear and extensional flows of weakly elastic polymer solutions. *Rheologica Acta*, 51(8):755–769.

Bibliography

Vadillo, D. C., Tuladhar, T. R., Mulji, A. C., Jung, S., Hoath, S. D., and Mackley, M. R. (2010). Evaluation of the inkjet fluid's performance using the "cambridge trimaster" filament stretch and break-up device. *Journal of Rheology*, 54(2):261–282.

Vasquez, P. A., McKinley, G. H., and Cook, L. P. (2007). A network scission model for wormlike micellar solutions - i. model formulation and viscometric flow predictions. *Journal of Non-Newtonian Fluid Mechanics*, 144(2-3):122–139.

Vasudevan, M., Buse, E., Lu, D., Krishna, H., Kalyanaraman, R., Shen, A. Q., Khomami, B., and Sureshkumar, R. (2010). Irreversible nanogel formation in surfactant solutions by microporous flow. *Nature Materials*, 9(5):436–441.

Vasudevan, M., Shen, A., Khomami, B., and Sureshkumar, R. (2008). Self-similar shear thickening behavior in ctab/nasal surfactant solutions. *Journal of Rheology*, 52(2):527–550.

Wagner, M., Collignon, B., and Verbeke, J. (1996a). Rheotens-mastercurves and elongational viscosity of polymer melts. *Rheologica Acta*, 35(2):117–126.

Wagner, M. H., Schulze, V., and Göttfert, A. (1996b). Rheotens-mastercurves and drawability of polymer melts. *Polymer Engineering & Science*, 36(7):925–935.

Walker, L. M., Moldenaers, P., and Berret, J. F. (1996). Macroscopic response of wormlike micelles to elongational flow. *Langmuir*, 12(26):6309–6314.

Webster, M., Matallah, H., Sujatha, K., and Banaai, M. (2008). Numerical modelling of step-strain for stretched filaments. *Journal of Non-Newtonian Fluid Mechanics*, 151(1-3):38–58.

Wheeler, E. K., Fischer, P., and Fuller, G. G. (1998). Time-periodic flow induced structures and instabilities in a viscoelastic surfactant solution. *Journal of Non-Newtonian Fluid Mechanics*, 75(2-3):193–208.

Wheeler, E. K., Izu, P., and Fuller, G. G. (1996). Structure and rheology of wormlike micelles. *Rheologica Acta*, 35(2):139–149.

Willenbacher, N., Matter, Y., Gubaydullin, I., and Schaedler, V. (2008). Effect of aggregation on shear and elongational flow properties of acrylic thickeners. *Korea-Australia Rheology Journal*, 20(3):109–116.

132

Wunderlich, I., Hoffmann, H., and Rehage, H. (1987). Flow birefringence and rheological measurements on shear induced micellar structures. *Rheologica Acta*, 26(6):532–542.

Xue, Z. J., Corvalan, C. A., Dravid, V., and Sojka, P. E. (2008). Breakup of shear-thinning liquid jets with surfactants. *Chemical Engineering Science*, 63(7):1842–1849.

Yamamoto, T. and Taniguchi, K. (2012). Emergence of turbid region in startup flow of ctab/nasal aqueous solutions between parallel plates. *Journal of Rheology*, 56(2):245–258.

Yang, J. (2002). Viscoelastic wormlike micelles and their applications. *Current Opinion in Colloid & Interface Science*, 7(5-6):276–281.

Yang, J. M. and Xu, Y. Z. (2008). Coalescence of two viscoelastic droplets connected by a string. *Physics of Fluids*, 20(4).

Yesilata, B., Clasen, C., and McKinley, G. H. (2006). Nonlinear shear and extensional flow dynamics of wormlike surfactant solutions. *Journal of Non-Newtonian Fluid Mechanics*, 133(2-3):73–90.

Ziserman, L., Raghavan, S. R., Baser, B., Kaler, E. W., and Danino, D. (2004). Micellar structure and rheological behavior in mixed surfactant systems. In *Annual Scientific Meeting of the Israel Society of Microscopy*, Jerusalem.

Zusammenfassung

Die vorliegende Arbeit behandelt eine experimentelle Untersuchung der kapillaren Verjüngung von Polymer- und Tensidlösungen sowie die daraus abgeleiteten dehnrheologischen Eigenschaften. Hierzu wird das so genanntes Capillary Breakup Extensional Rheometer (CaBER) eingesetzt, da dieses Verfahren die Bestimmung der dehnrheologischen Eigenschaften niederviskoser Flüssigkeiten ermöglicht. Entsprechende Versuche werden sowohl in vertikaler als auch horizontaler Ausrichtung durchgeführt. Bei der Durchführung eines CaBER-Experimentes wird zunächst eine Flüssigkeitstropfen zwischen zwei konzentrischen Platten gegeben. Im Anschluss wird dieser schlagartig verstreckt und so eine instabile Flüssigkeitsbrücke erzeugt. Im weiteren Verlauf des Experimentes verjüngt sich diese aufgrund der Oberflächenspannung des Fluides bis letztendlich der Fadenriss eintritt. Entsprechende dehnrheologische Parameter können, zumindest näherungsweise, aus der zeitlichen Abnahme des Fadendurchmessers bestimmt werden.

Generell lässt sich die vorliegende Arbeit in drei aufeinander aufbauende Hauptaspekte unterteilen:

1. Bestimmung der wahren axialen Fadenkraft währen der kapillaren Verjüngung, sowie die Berechnung der wahren Dehnviskosität,

2. das Dehnverhalten von (meist) verschlauft vorliegenden Polystyrol- (PS) und Polyethylenoxidlösungen (PEO) bei unterschiedlichen Temperaturen sowie Lösemittelviskositäten und

3. das Dehnverhalten von Tensidlösungen, die in einer wurmartigen Mizellstruktur (engl. wormlike micelles, WLM) vorliegen (CPyCl/NaSal, CPyCl/NaSal/NaCl, CTAB/NaSal, CTAB/KBr, CTAB/NaNO$_3$, and CTAB/NaClO$_3$)[1]

Zunächst wird in dieser Arbeit eine neuartige Möglichkeit zur Durchführung von CaBER-Versuchen beschrieben. Diese so genannte "tilted CaBER"-Methode basiert auf der horizontalen Verstreckung von Flüssigkeitsfäden, die sich aufgrund der Erdanziehung durchbiegen.

---

[1]CPyCl: Cetylpyridiniumchlorid, NaSal: Natriumsalicylat, NaCl: Natriumchlorid, CTAB: Cetyltrimethylammoniumbromid, KBr: Kaliumbromid, NaNO$_3$: Natriumnitrat, NaClO$_3$: Natriumchlorat

Zusammenfassung

Eine Analyse der Filament-Durchbiegung gemäSS der Theorie der Balkenbiegung ermöglicht es erstmalig die wahre Axialkraft F, in einem Bereich von $F = 0.1 - 1,000 \ \mu N$, während der kapillaren Verjüngung von Fluidfäden zu bestimmt. Weiterhin kann durch diese Versuchsführung erstmalig die wahre Dehnviskosität bestimmen werden, ohne dabei weitere Annahmen bezüglich spezieller Materialgesetze zu treffen.

Im Allgemeinen basiert die Datenanalyse sowie die Berechnung der Dehnviskosität jedoch auf der Annahme, dass keine axialen Normalspannungen σ_{zz} während der kapillaren Verjüngung im Fluid auftreten. Aus dieser so genannten $\sigma_{zz} = 0$ Annahme ergibt sich dann eine scheinbare (engl. apparent) Axialkraft $F_{app} = \pi D \Gamma$ im Fluidfilament, die nur von der Oberflächenspannung Γ (bei bekanntem Fadendurchmesser D) hervorgerufen wird. Die in dieser Arbeit durchgeführten Untersuchungen zeigen jedoch, dass diese weit verbreitete Annahme im Allgemeinen nicht erfüllt ist. Abweichungen werden zweckmäSSigerweise in dimensionsloser Form mittels dem Kräfteverhältnisses $X = F/F_{app}$ untersucht.

Newtonsche Fluiden (Zuckerlösungen und Mischungen aus Silikonölen) in einem Viskösitätsbereich von $0.9 - 60$ Pas zeigen hierbei neben einem linearen Durchmesser-Zeit-Verlauf ein Kräfteverhältnis von $X = 0.713$ und somit eine negative Axialspannung $\sigma_{zz}/|\sigma_{rr}| < 0$ (Druckspannung). Dieses Ergebnis bestätigt direkt die nummerischen Berechnungen von [Papageorgiou 1995], der diesen Wert für die kapillare Verjüngung von Newtonschen Fluiden für den Grenzfall vernachlässigbarer Trägheit vorhergesagt hat.

Das Kräfteverhältnis $X(t)$ viskoelastischer Lösungen ist zu Beginn durch eine exponentielle Abnahme bestimmt. Die daraus definierte Relaxationszeit λ_X zeigt sich identisch zu der Dehnrelaxationszeit λ_e, die aus dem exponentiell abnehmenden Durchmesser am Ende der kapillaren Verjüngung bestimmt wird. Somit kann gezeigt werden, dass sowohl der Beginn der kapillaren Verjüngung als auch der Bereich in dem der Fadendurchmesser exponentiell abnimmt von den selben molekularen Relaxationsprozessen bestimmt werden.

Im weiteren Verlauf der kapillaren Verjüngung zeigt sich ein (zumindest zeitweise) konstanter Wert $\tilde{X}$, welcher eine Abhängigkeit von der Polymerkonzentration und der so genannten Elastokapillarzahl Ec_0 aufweist.

Viskoelatische Polyethylenoxid-Lösungen, die durch eine hohe Elastokapillarzahlen charakterisiert sind, zeigen in einem Konzentrationsbereich zwischen der kritischen Konzentration c^* und der doppelten Entanglementkonzentration $2c_e$ einen exponentiellen Durchmesser-Zeit-Verlauf sowie eine Kräfteverhältnis $\tilde{X} = X_\infty = 1$. Somit treten bei diesen Fluiden während der kapillaren Verjüngung keine axialen Normalspannungen auf ($\sigma_{zz}/|\sigma_{rr}| = 0$). Bei höheren Polymerkonzentrationen ($c > 2c_e$) zeigt sich jedoch eine kontinuierliche Zunahme des Kräfteverhältnisses $X_\infty > 1$ und somit eine positive axiale Normalspannung ($\sigma_{zz}/|\sigma_{rr}| > 0$) während der gesamten kapillaren Verjüngung. Weiterhin lässt sich

in diesem Konzentrationsbereich keine Durchmesserabnahme mit exponentiellem Charakter beobachten. Somit scheint es, dass ein exponentieller Durchmesser-Zeit-Verlauf nur dann beobachtet werden kann, wenn die $\sigma_{zz} = 0$ Annahme erfüllt ist. Andere Stoffsysteme, wie PS- oder CPyCl/NaSal/NaCl-Lösungen, die überwiegend $Ec_0 < 1$ aufweisen, zeigen ein komplexeres Verhalten für den zeitlichen Verlauf der Axialkraft F. Nach der exponentiellen Abnahme des Kräfteverhältnisses zeigt sich ein zeitweise konstanter Bereich mit $X = 0.713$ bevor auch diese Lösungen ein Kräfteverhältnis von $X_\infty = 1$ (begleitet von einem exponentiellen Durchmesser-Zweit-Verlauf) aufweisen. Hierdurch kann ein mittlerer Newtonscher Bereich währen der kapillaren Verjüngung von Fluiden mit $Ec_0 < 1$, wie er bereits zuvor von Clasen [Clasen 2010] vermutet wurde, direkt nachgewiesen werden.

Die Abweichung von der $\sigma_{zz} = 0$ Annahme ($X \neq 1$) zeigt einen direkten Einfluss auf die Dehnviskosität und somit eine Abweichung zwischen dem wahren und scheinbaren Wert ($\eta_e \neq \eta_{e,app}$). Deswegen müssen scheinbare Dehnviskositäten, welche alleinig aus der zeitlichen Abnahme des Fadendurchmesser bestimmt sind, mittels des Faktors $2X - 1$ korrigiert werden um den wahren Wert für die Dehnviskosität zu erhalten. Der zeitliche Verlauf der so bestimmten wahren Dehnviskosität zeigt ein deutliches Minimum wodurch eine minimales Trouton-Verhältnis $Tr_{min} = \eta_{e,min}/\eta_0$ bestimmt werden kann. Tr_{min} nimmt mit zunehmender Polymerkonzentration ab und erreicht für hohe Konzentrationen einen konstanten Wert. Für PEO-Lösungen ergibt sich, unabhängig von der Viskosität des Lösemittels, $Tr_{min} \approx 10$ wobei PS- und CPyCl/NaSal/NaCl-Lösungen ein minimales Trouton-Verhältnis von $Tr_{min} = 3$ aufweisen.

Durch die in dieser Arbeit gewonnenen Kenntnisse zur Bestimmung der wahren Dehnviskosität aus CaBER-Versuchen wird ersichtlich, dass die in der Literatur für WLM-Lösungen beschriebenen Unterschiede zischen CaBER und kontinuierlichen Dehnversuchen (FiSER) [Bhardwaj et al. 2007a] nicht auf die vereinfachte Auswertung der CaBER-Messungen zurückzuführen sind. Vermutlich liegen diese Abweichungen auf Unterschiede in der Deformationsvergangenheit oder an unterschiedlichen Mechanismen beim Fadenriss begründet.

Neben der Dehnviskosität lässt sich auch die Dehnrelaxationszeit λ_e aus CaBER-Versuchen ermitteln. Diese zeigen, wie auch die Scherrelaxationszeit λ_s, eine Zunahme mit der Polymerkonzentration. Das entsprechende Relaxationszeitverhältnis λ_e/λ_s nimmt mit zunehmender Polymerkonzentration exponentiell ab. Durch Auftragung von λ_e/λ_s über die reduzierte Konzentration $c[\eta]$, wobei $[\eta]$ die intrinsische Viskosität darstellt, ergibt sich eine Masterkurve für die untersuchten Polymerlösungen obwohl diese unterschiedliche Molekulargewichte, Messtemparturen sowie Lösemittelviskositäten aufweisen. Die starke Abhängigkeit des Relaxationszeitverhältnisses λ_e/λ_s bestätigt einen deutlichen Einfluss der nichtlinearen Deformation in einem CaBER-Experiment, wie er bereits früher beobachtet wurde [Arnolds et al. 2010].

Der dritte und wahrscheinlich wissenschaftlich interessanteste Teil dieser Arbeit beinhaltet die erste systematische Untersuchung von Lösungen aus wurmartigen Tensidmizellen. Hierbei werden sechs unterschiedliche Systeme untersucht (CPyCl/NaSal, CPyCl/NaSal/NaCl, CTAB/NaSal, CTAB/KBr, CTAB/NaNO$_3$ und CTAB/NaClO$_3$) und dabei die Tensidkonzentration c_s, sowie das Salz/Tensid-Verhältnis R über einen weiten Bereich variiert. Die grundlegenden experimentellen Ergebnisse sind schematisch in Abbildung 7.4 dargestellt.
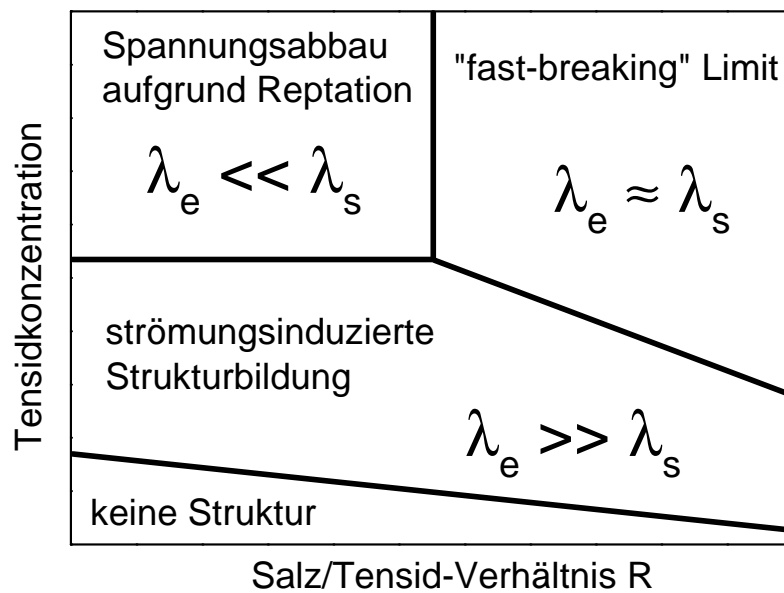
Figure 7.4: Schematisches Phasendiagramm für WLM Lösungen in Abhängigkeit von der Tensidkonzentration und dem Salz/Tensid-Verhältnisses R.

Tensidlösungen deren Spannungsrelaxation durch Reptation gekennzeichnet sind (hohe Tensidkonzentration und geringes Salz/Tensid Verhältnis R) zeigen Relaxationszeitverhältnisse von $\lambda_e/\lambda_s < 1$ wie sie bereits bei Lösungen aus kovalent gebundenen Polymeren beobachtet wurden. Dies ist höchst wahrscheinlich auf eine Dehnung bzw. eine Orientierung der Mizellen in der starken Dehnströmung zurückzuführen. Dennoch sind an dieser Stelle weitere Untersuchungen der Mizellstruktur notwendig um zusätzliche Effekte einer möglichen Abnahme der mittleren Mizelllänge $\tilde{L}$ beurteilen zu können.

Im Bereich hoher Tensidkonzentrationen sowie hohen Salz/Tensid-Verhältnissen R, dem so genannten "fast breaking limit", können einzelne Mizellen brechen und sich wieder rekombinieren und ermöglichen so weitere Mechanismen zur Spannungsrelaxation. Für diese Lösungen zeigen sich Relaxationszeitverhältnisse von $\lambda_e/\lambda_s \approx 1$. Nichtlineare Effekte scheinen durch den ständigen Mizellbruch und -aufbau unterdrückt zu werden, so dass die kapillare Verjüngung alleinig durch lineare Materialparameter wie dem Plateaumoduls G_0 sowie der

Bruchzeit λ_{br} bestimmt werden.

Für die Lebensdauer des Filamentes t_{fil} kann ein universelles Skalengesetz ($t_{fil}/G_0 \propto \lambda_{br}^{2/3}$) angegeben werden welches ebenfalls für WLM-Lösungen mit $\lambda_e/\lambda_s < 1$ gültig ist, solange λ_{br} aus Scherdaten eindeutig bestimmbar bleibt. Dies weiSSt darauf hin, dass die mittlere Länge der Mizellem $\tilde{L}$ sich währen des CaBER-Versuches nicht ändert.

Unerwartet hohe Fadenlebensdauern $t_{fil} >> t_{fil,Newton}$ und Relaxationszeitverhältnisse $\lambda_e/\lambda_s > 1$ werden für Lösungen mit geringen Tensidkonzentrationen unabhängig von R beobachtet. Dies deutet auf eine Bildung dehninduzierter Strukturen (engl. elongation induced structures, EIS) hin. Gestützt wird diese Vermutung von der Tatsache, dass alle Lösungen die EIS zeigen auch eine Strukturbildung in Scherung (engl. shear induced structures, SIS) aufweisen. Weiterhin zeigt sich, dass zur Bildung solcher langlebiger Filamente und somit zur Bildung von EIS eine minimale Viskosität η_0 der Lösung sowie ein minimaler Durchmessers D_1 des Fluidfadens benötigt werden. Ergänzende FiSER-Experimente deuten auf eine, für die Strukturbildung notwendige, kritische Gesamtdeformation hin. Weitere Untersuchungen sind jedoch notwendig (z.B. Messung von Trübung und Doppelbrechung sowie Streuesperimente) um die Bildung von EIS eindeutig zu beweisen und die Struktur der eventuell entstehenden Mizellen zu erhalten.